Development of an independent MU calculation methodology for treatments with small fields

Guilherme Filipe Pinto Campos

Mestrado em Física Médica

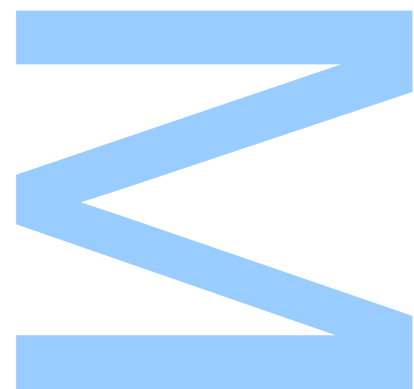Departamento de Física e Astronomia

2019

Orientador

Anabela Gregório Dias, PhD, Instituto Português de Oncologia do Porto Francisco Gentil, EPE

Coorientador

Ana Catarina Santos Souto, MSc, Instituto Português de Oncologia do Porto Francisco Gentil, EPE

IPOPORTO

U.PORTO

FC **FACULDADE DE CIÊNCIAS**
UNIVERSIDADE DO PORTO

Todas as correções determinadas

pelo júri, e só essas, foram efetuadas.

O Presidente do Júri,

Porto, _____/_____/_____

Agradecimentos

Este espaço é dedicado a todos aqueles que contribuíram para o desenvolvimento desta tese, de forma direta ou indireta.

Em primeiro lugar, uma nota de agradecimento às orientadoras, Prof. Anabela Dias e Prof. Catarina Souto pela orientação do trabalho, tempo despendido, disponibilidade, dedicação e assistência.

Ao Prof. Joaquim Agostinho e à Prof. Carla Rosa, que após a primeira entrevista para entrar no Mestrado, acreditaram nas minhas capacidades para concluir o grau académico.

Aos meus colegas de trabalho que me apoiaram para ingressar no Mestrado.

À minha entidade empregadora (Júlio Teixeira, S.A.) por me deixar exercer funções como Técnico de Radioterapia dosimetrista no Instituto CUF Porto e realizar este Mestrado em simultâneo sem qualquer contrapartida.

À minha família e amigos, pelo apoio incondicional ao longo destes anos.

Resumo

O desenvolvimento de técnicas de estereotaxia no passado permitiu o tratamento de pequenas lesões malignas e não malignas, numa única ou em várias frações de tratamento, com mais precisão e com uma maior dose de radiação ao tumor. Para assegurar a correta precisão dos tratamentos de estereotaxia, os departamentos de física dos serviços de radioterapia devem ter um programa exaustivo de controlo de qualidade. Múltiplas *guidelines* internacionais recomendam a verificação independente do *output* calculado com um método de cálculo alternativo.

O desenvolvimento de uma calculadora independente de unidades monitor (MU) com correções de heterogeneidades foi proposto como objetivo principal deste trabalho, para um Varian TrueBeam™ STx (6FFF e 10 FFF) e um Varian Novalis Tx™ (6X SRS) usando cones estereotáxicos. Múltiplas medidas em profundidade, perfis de dose e *output factors* foram medidos em ambos os aceleradores lineares usando um detetor apropriado para medições de campos pequenos. As medidas seguiram o formalismo de dosimetria para campos pequenos proposto pelo TRS-483, o qual foi publicado em Novembro de 2017.

Duas interfaces gráficas foram criadas em MATLAB®, uma interface para a importação e processamento de dados do feixe a partir de ficheiros PTW MEPHYSTO mc^2 ou a partir dos dados de referência da Varian e outra interface para importação de dados do doente e cálculo de MU, com e sem correção de heterogeneidades.

Os algoritmos desenvolvidos para cálculo de MU com e sem correção de heterogeneidades foram extensivamente testados usando um fantoma de tórax QUASAR™ e um fantoma Lucy® 3D QA. Todos os testes de validação em fantomas passaram com a exceção de um teste de validação sem correção de heterogeneidades.

Para os doentes, a diferença máxima de 5% entre a dose planeada e absorbida é largamente aceite para assegurar que o tratamento é seguro e efetivo. Múltiplos doentes com planos de tratamento em ambos os aceleradores lineares foram testados. Apenas um campo de tratamento em dois doentes diferentes excedeu a tolerância aceite com correção de heterogeneidades.

Palavras-chave: radiocirurgia, dosimetria de campos pequenos, cones estereotáxicos, correção de heterogeneidades, TRS-483.

Abstract

The development of stereotactic techniques in the past allowed the treatment of small malignant and non-malignant lesions, in single or multiple fractions, with more accuracy and a higher dose of radiation to the tumour. To ensure the correct accuracy of stereotactic treatments, radiotherapy physics departments should have an exhaustive quality assurance program. Several international guidelines recommend the independently verification of the computer calculation output with an alternative calculation method.

The development of an independent monitor unit (MU) calculator with heterogeneity correction was proposed as the main objective of this work, for a Varian TrueBeam™ STx (6 FFF and 10 FF) and a Varian Novalis Tx™ (6X SRS) using stereotactic cones. Multiple depth curves, dose profiles and output factors were measured in both linear accelerators using an appropriate detector for small field measurements. The measurements followed the dosimetry formalism for small fields proposed by the TRS-483, which was published in November 2017.

Two graphical interfaces were created in MATLAB®, one interface for beam data import and processing of PTW MEPHYSTO mc^2 files or Varian golden beam data files and another interface for patient data import and MU calculation, with and without heterogeneity correction.

The developed algorithms of MU calculation with and without heterogeneity correction were extensively tested using a QUASAR™ thorax phantom and a Lucy® 3D QA phantom. All the phantom validation tests passed with an exception of one field in the validation test without heterogeneity correction.

For patients, a maximum difference of 5% between the planned dose and the absorbed dose is widely accepted to ensure that the treatment is safe and effective. Multiple patients with treatment plans on both linear accelerators were tested. Only one treatment field of two different patients exceeded the tolerance accepted with heterogeneity correction.

Keywords: radiosurgery, dosimetry of small fields, stereotactic cones, heterogeneity correction, TRS-483.

Contents

List of Tables

List of Figures

Acronyms

3D-CRT   three-dimensional conformal radiotherapy

AAPM   American Association of Physicists in Medicine

ADCL   accredited dosimetry calibration laboratory

BRW   Brown-Roberts-Wells

CAX   central axis

CDC   Cone Dose Calculation

CRW   Cosman-Roberts-Wells

CT   computed tomography

CVD   chemical vapor deposition

DICOM   Digital Imaging and Communications in Medicine

DNA   deoxyribonucleic acid

DRR   digital reconstructed radiography

DVH   dose-volume histogram

EPL   equivalent path length

FFF   flattening filter free

FRIS   Frameless Radiosurgery Imaging Support

FSRT   fractionated stereotactic radiotherapy

FWHM   full-width at half maximum

GUI   graphical user interface

HFS   head first supine

HU   hounsfield units

IAEA   International Atomic Energy Agency

ICVI   Integrated Conical Collimator Verification & Interlock

IMRT   intensity modulated radiation therapy

LCPE   lateral charged particle equilibrium

LINAC   linear accelerator

MLC   multileaf collimator

MOSFET metal oxide semiconductor field effect transistor

MPV   mean pixel value

MRI   magnetic resonance imaging

MU   monitor unit

OAR   off-axis ratio

OBI   On-Board Imager®

OF   output factor

OSMS   Optical Surface Monitoring System

PDD   percentage depth dose

PET   positron emission tomography

PSDL   primary standards dosimetry laboratory

RCS   reference coordinates system

RED   relative electron density

RGB   red, green and blue

ROI   region of interest

SAD   source-axis distance

SBRT   stereotactic body radiation therapy

SCD   source-to-chamber distance

SPECT   single-photon emission computed tomography

SRS   stereotactic radiosurgery

SSD   source-to-skin distance

SSDL   secondary standards dosimetry laboratory

STD   source-to-target distance

TCPE   transient charged particle equilibrium

TIFF   tagged image file format

TLD   thermoluminescence dosimetry

TMR   tissue maximum ratio

TPR   tissue phantom ratio

TPS   treatment planning system

VMAT   volumetric arc therapy

WFF   without flattening filter

1 Introduction

Today cancer is the second cause of death around the globe [1]. Each year, 14 million of new cases of cancer are diagnosed [2]. Half of the patients diagnosed with cancer can benefit from radiotherapy, 50% with curative intent and another 50% with palliative relief [2]. World Health Organization estimates that 9.6 million people died in 2018 from cancer [1]. In Portugal the cancer incidence is rising 3% each year. The mortality rate is also increasing but slowly. Although we have more patients diagnosed with cancer, the success of cancer treatment is growing [3].

Radiotherapy is used to treat cancer with high-energy particle or waves such as X-rays, gamma rays, electron or proton beams [4]. It can also provide local control or symptom relief in cancers that are locally advanced or disseminated [3]. The development of stereotactic techniques allows the treatment of small lesions in the brain with more accuracy. Radiosurgery patients receive a high dose of radiation in the tumour area that needs to be treated, while nearby regions receives low doses because of the sharp dose fall-off provided by stereotactic cones or multileaf collimators (MLC).

The technique choice depends on the tumour size and the proximity within critical structures. Stereotactic radiosurgery (SRS) is administrated in a single fraction to small intracranial lesions while fractionated stereotactic radiotherapy (FSRT) is used for large lesions or those in close proximity to critical structures. FSRT balances the tumour control and the damage to normal tissue [5]. A diameter of 3 cm on its maximum extent is the size limit commonly accepted to make SRS [6], [7].

The objective of this work is the development of an independent MU calculator for stereotactic treatments with Varian and BrainLAB cone systems in a Varian TrueBeam™ STx and Varian Novalis Tx™ using photon flattening filter free (FFF) energies (6 FFF / 10 FFF) and 6X SRS, respectively. The independent MU calculator developed will take into account tissue heterogeneities, overcoming the main limitation of the Cone Dose Calculation (CDC) algorithm used in radiosurgery treatment dose calculations.

This work will follow the new dosimetry formalist for small fields proposed by the International Atomic Energy Agency (IAEA) TRS-483: Dosimetry of Small Static Fields Used in External Beam Radiotherapy.

2 Stereotactic Radiotherapy/Radiosurgery

2.1 Historical Background

SRS was first described in 1951 by Swedish neurosurgeon Lars Leksell. He used a stereotactic frame of his own design coupled with a 200 kV X-ray therapy machine to treat patients for trigeminal neuralgia. Leksell's strategy of precise stereotactic localization of a target and their irradiation with a focused beam of X-rays was the first example of a minimally invasive procedure called radiosurgery, which has proliferated extensively since then [8].

Leksell Gamma Knife was the first commercially available radiosurgical treatment device in 1968 [9]. This system consisted of 179 ^{60}Co sources aimed at an isocenter. Each source was collimated by a fixed collimator and with a helmet. Beams had a circular shape with nominal diameters of 4, 8, and 14 mm at the isocenter [10]. The result was a spherical dose distribution with sharp dose falloff [11]. This provided an alternative treatment to certain neurosurgical procedures that were treated with needles before the development of Gamma Knife with significant morbidity [9]. Stereotaxis refers to the use of a three-dimensional coordinate system to localize intracranial targets and has been more recently extensively developed in extracranial clinical situation. It delivers high doses of ionizing radiation with great conformality and a very high geometrical precision in single fractions (SRS) or multiple fractions (FSRT) [8]. Both techniques nowadays are used because of the advances in medical imaging, computer technology, software development and radiation-delivery technology [9].

SRS was developed to treat malignant and non-malignant structures in the cranial vault. However, the administration of high doses in a single fraction can produce considerable side effects in normal tissues surrounding the target volume. FSRT combines the precision of target localization and dose application of SRS with radiobiological advantage because it allows the deoxyribonucleic acid (DNA) of the normal tissue to repairs itself during the time between fractions [12].

In the eighties conventional radiation therapy devices were adapted for special procedures by the addition of specialized collimators and other devices that allowed stereotactic radiosurgery techniques. Many of these improvements were custom made for each clinical facility [8]. The proliferation of stereotactic treatments in linear accelerators began with the introduction of the non-invasive Gill-Thomas-Cosman frame that could subsequently be repositioned with a displacement < 1 mm [8].

Novalis was the first linear accelerator (LINAC) able to perform both SRS and FSRT treatments. The first unit was installed in the state of California in 1997. This LINAC employed circular collimators (from 5 to 60 mm in diameter) attached to an accessory tray and a mini-multileaf collimator (with central leaves of 3 mm, adjacent leaves of 4.5 mm

and outer leaves of 5.5 mm) with a maximum field size of 10x10 cm^2 at the isocenter [8]. Another LINAC dedicated to SRS and FSRT was the Neurotron 1000. This device is now commercialized by Accuray under the trade name of CyberKnife®. This machine features a compact LINAC mounted on an industrial robotic arm. It is a purely image-guided device that relays on stereoscopic planar imaging, multiple non-coplanar and non-isocentric beams onto fixed or moving targets in the head or body of the patient [13].

2.2 Overview of the Varian Novalis Tx™ and Varian TrueBeam™ STx systems

Varian Novalis Tx™

The Novalis LINAC provides an integrated system with technology developed by both Varian and BrainLAB, featuring a treatment planning system, an automated patient positioning with image-guidance and a treatment delivery LINAC (figure 1). In this way, possible problems related with the communication between the different systems and vendors are avoided because the treatment chain is integrated in all process [8].

The equipment is very similar to the Varian Trilogy® with its on-board imaging capabilities (on-board imager® (OBI) and MV panel), however the MLC is slightly different. This has a high definition MLC (HD-MLC) with a total of 60 leaf pairs (32 inner leaf pairs of 2.5 mm width at the isocenter and 14 outer leaf pairs on either side (28 total) with 5 mm width at the isocenter), providing a maximum field size of 40x22 cm^2 when using MLC. It has multiple photon and electron beam energies (6 and 15 MV for photons and 6, 9, 12, 15, 18 and 22 MeV for electrons), with a maximum dose rate of 600 MU/min for standard beams and 1000 MU/min (SRS mode) for 6 MV photon beams. This higher dose rate is achieved with a different flattening filter but it restricts the maximum field size to 15x15 cm^2 [14].

A set of conical collimators of 4, 6, 7.5, 10, 12.5 and 15 mm are accessible with the Novalis Tx™ model. Each cone aperture considers the beam divergence, reducing the penumbra, achieving a steeper dose gradient. Cones are securely fixed to the gantry thought a collimator mount with a bayonet locking mechanism. This system possesses software and hardware interlocks to ensure the correct choice of the collimator is inserted and the delivery of radiation outside the area shielded by the cone is avoided with the limitation of the secondary collimator settings [13].

The Novalis family system come with an integrated treatment planning system (TPS) (BrainSCAN and iPlan® RT). The iPlan® RT supports image fusion between different imaging modalities, automatic segmentation of the critical relevant structures for brain, spine, head and neck, and prostate treatments. It supports different treatment options including static conformal arcs, conformal beams, dynamic conformal arcs, cones and intensity modulated radiation therapy (IMRT). There are two algorithms for dose

calculation: Pencil Beam and Monte Carlo. The latter takes into account the LINAC head geometry, secondary electrons and tissue inhomogeneities, commonly found in extra cranial treatments. However, Novalis Tx™ can deliver treatments planned with other TPS such as Varian Eclipse™ and Philips Pinnacle, since they all provide integrated treatment planning technologies for radiosurgery [13].

The ExacTrac® system is composed of two sets of equipment: two kV X-ray imaging units and an IR-based optical positioning system. The sources of the X-ray units are installed on the floor (on either side of the LINAC) and the amorphous silicon flat panel is mounted diagonally on the ceiling [14]. The IR-based system is composed by a pair of infrared video cameras that triangulate an external set of fiducial markers (Body Marker Array) which is fixed to the thorax and/or abdomen of the patient [13]. The fusion of the orthogonal planar images with the digital reconstructed radiograph (DRR) created in the planning computed tomography (CT) scan provide the translations and rotations that are corrected with the Brainlab ExacTrac 6D Robotic Couch.

Figure 1: Varian Novalis Tx™ overview of its LINAC, couch and imaging systems. Image from Varian Medical Systems.

Varian TrueBeam™ STx

The TrueBeam™ STx (figure 2) is an advanced linear accelerator fully integrated for image-guided radiotherapy and radiosurgery. It features multiple photon and electron beam energies (2.5, 6, 10 and 15 MV for photons and 6, 9, 12 and 15 MeV for electrons), a high-definition multi-leaf collimator with the same specs as the Novalis Tx™ and a treatment couch with six degrees of freedom for the most accurate patient alignment possible [15]. It also includes the ExacTrac® system developed by BrainLAB. The linear accelerator is controlled by the new Maestro control architecture that synchronizes dosage, motion and imaging for a fast and efficient treatment [16].

It offers both flattened and FFF beams. FFF beams allow faster treatments because the removal of the flattening filter increases the dose rate. FFF beams are available at 6 MV FFF and 10 MV FFF with a maximum dose rate of 1400 MU/min and 2400 MU/min respectively.

Figure 2: Varian TrueBeam™ STx overview of its LINAC, couch and imaging systems. Image from Varian Medical Systems.

TrueBeam™ STx is bundled with the SRS Intracranial solution from Varian that enables SRS treatments to be delivered with precision and efficiency. The SRS Intracranial solution includes [17]:

- Optical Surface Monitoring System (OSMS) – a non-ionizing 3D imaging technology that reconstructs the 3D surface data referenced to the isocenter. It allows a highly accurate tracking of cranial positions even with non-coplanar beams. A display shows the motion in all six degrees of freedom and may be viewed throughout treatment;

- Integrated Conical Collimator Verification & Interlock (ICVI) – a system that provides a robust and verifiable method of mounting and verifying conical collimators. The ICVI system checks if the corrected cone size is attached, according to the treatment plan. An incorrect cone size triggers an interlock, increasing the patient safety. The 7 conical collimators have the following sizes: 4, 5, 7.5, 10, 12.5, 15 and 17.5 mm;

- Eclipse™ Cone Planning – A dedicated TPS that provides planning and dose calculation using conical collimators. It supports frame or frameless immobilization.

2.3 SRS/FSRT Treatment Planning

The SRS/FSRT treatment is planned using a brain CT scan. Often a magnetic resonance imaging (MRI) is fused with CT scan in order to provide better tumour delineation.

2.3.1 Computed Tomography Imaging

The stereotactic coordinates are used to define the volume which has to be irradiated, therefore, target volume and organs at risk are localized in the space defined by the stereotactic coordinates system. The localizer is a box with fiducial markers on each plane that defines the link between the stereotactic coordinates and the imaging coordinates so that any point in the 3D stereotactic coordinates can be determined [10].

The patient realises the CT scan on the Frameless Radiosurgery Imaging Support (FRIS) on the CT couch. After the mask preparation and cooling the CT scan is acquired following the institution protocol.

Other imaging modalities can be used complementarily with CT images for volumes definition, such as MRI and angiography and less frequently positron emission tomography (PET) and single-photon emission computed tomography (SPECT) [10].

2.3.2 Stereotactic devices

Stereotactic treatment implies the use of a device that can precisely direct the radiation to a specific site of the body [9]. For FSRT treatments the head is fixed non-invasively in a thermoplastic mask attached on the stereotactic frame [10]. Recently were developed frameless stereotactic techniques that use optical and radiographic methods. Independently of the device, the purpose is to provide an accurate coordinate system to direct radiation to the target [9].

There are different stereotactic frame systems like: Brown-Roberts-Wells (BRW), Cosman-Roberts-Wells (CRW), Leksell, Leibinger-Fischer and the BrainLAB system. Each system differs from each other in the material of the frame, design, connection with the localizer and the positioner and the accuracy [10].

2.3.3 Treatment Planning

After the delineation of the target volume and organs at risk that may get significant dose, the isocenter is defined. This point is located inside the target volume and must be positioned with precision in the isocenter of the treatment machine. In the case of multiple lesions more than one isocenter can be defined. The TPS outputs the position of

the isocenters in stereotactic coordinates that are used to correctly position the patient. The position step is done with a positioner (or localizer) attached to the stereotactic frame that allows the connection between the stereotactic coordinate system and the room coordinate system [10].

There are multiple collimation choices for stereotactic treatments. For circular or oval target volumes, stereotactic conic collimators can be used. Stereotactic conic collimators are tertiary collimators with diameter usually between 1 and 35 mm that can be attached to the LINAC. If the target volume is irregular, micro MLC can be used. The decreased leaf width has advantages in comparison with the traditional MLC. In this way, MLC leaves can be adjusted individually to the tumor shape. Micro MLC also permits the possibility of dynamic fields during irradiation and allows the implementation of IMRT and field shaping with dynamic arcs [10]. Stereotactic cones, however, have a higher mechanical stability and a sharper dose fall-off compared to MLC because of the smaller source-to-collimator distance and focused cone aperture in contrast to the round shape of the MLC leaf ends [18].

The radiation techniques in a conventional LINAC are, in general, isocentric and implemented with a rotational technique using conic collimators or dynamic fields. Static-field technique can also be used [10].

2.3.4 Positioning and radiation delivery

The positioning is done with the stereotactic positioner that allows the projection of the coordinates of the isocenter onto the orthogonal planes attached to the stereotactic frame. This way, the patient can be positioned so that the isocenter of the plan and the isocenter of the LINAC defined by the room-based lasers overlap. After positioning the patient, the positioner is removed and the treatment can start [10].

It is important to know that the mechanical stability and precision of the LINAC has to be much better than in the conventional radiation treatment [10] in order to provide sub-millimeter accuracy [9]. The axis of gantry rotation, the central axis of the beams and the rotation axis of the rotation table should convert to the isocenter within a fraction of a millimeter over all rotational angles that are used clinically [9].

TG-142 introduces new recommendations for quality assurance tests of medical linear accelerators that are capable of SRS and SBRT with higher tolerances for this type of treatments. The most notable mechanical tolerances that differ from conventional treatment techniques are the laser localization, the collimator size indicator and the treatment couch position indicators [19]. These differences are shown on table 1 and table 2.

Table 1: TG-142 daily mechanical tolerances for 3D-CRT and SRS/SBRT techniques.

Mechanical tolerance (daily tests)	3D-CRT	SRS/SBRT
Laser localization	2 mm	1 mm
Collimator size indicator	2 mm	1 mm

Table 2: TG-142 monthly mechanical tolerances for 3D-CRT and SRS/SBRT techniques.

Mechanical tolerance (monthly tests)	3D-CRT	SRS/SBRT
Treatment couch position indicators	2 mm / 1º	1 mm / 0.5º
Localizing lasers	$\pm$ 2 mm	$< \pm$ 1 mm

3 Small fields dosimetry

Radiation dosimetry measures the absorbed dose or dose rate resulting from the interactions of ionizing radiation with matter [20]. It is essential for the quantification of the various biological changes as a function of the amount of dose received [21].

The success of radiotherapy depends on the accurate determination of absorbed dose because of the dose-response curve for tumour control and normal tissue damage. A small difference in the dose received by the tumour may compromise the tumour eradication in case of under-dosage or complications in the normal tissue through overdosage [22]. The steps involved in the determination of absorbed dose integrate measurements with a detector (dosimeter) in a phantom (most of the times water) under the radiation field [22].

Large developments in radiotherapy techniques and treatment units have led to a proliferation of the use of small fields. The dosimetry of small fields is particularly complex and prone to errors [8]. It is important to apply multiple levels of redundancy in the determination of the absorbed dose by the use of different detectors with appropriate detector correction factors for the measurements, analysis of measured data on other similar equipment and corroboration of data with manufacturer reference data [8].

The reference dosimetry of high energy photons used in external radiotherapy is currently based on code of practices or dosimetry protocols such as the TRS-398 and TG-51. These codes of practices are based on measurements with ionization chambers that have calibration coefficients in terms of absorbed dose to water. The reference conditions for these calibration coefficients specify a reference field size of 10x10 cm^2. The IAEA and the American Association of Physicists in Medicine (AAPM) decided to develop internationally standardized recommendations for the dosimetry of small static photon fields up to 10 MV for machines that cannot establish the conventional 10x10 cm^2 reference field in external radiation therapy. The result of that work culminated in the publication of IAEA TRS-483, which is the first international code of practice dedicated to the dosimetry of small fields for specialized radiotherapy equipment able to produce small fields and for conventional LINACs with and without flattening filter [23] . This code of practice introduces a new type of reference field for beam calibration: the machine specific reference (*msr*) field for treatment units that cannot establish the conventional 10x10 cm^2 reference field.

3.1 Physics of small fields

A photon beam is considered small if one of the following conditions is fulfilled [24]:

- There is a loss of lateral charged particle equilibrium (LCPE) on the beam axis;

- There is a partial occlusion of the photon source by the collimating devices on the beam axis;

- The size of the detector is similar or large compared to the beam dimensions.

3.1.1 Lateral charged particle equilibrium

Transient charged particle equilibrium (TCPE) regions are defined as zones where, past the build-up region, absorbed dose and collision kerma are related to a slowly varying function. In photon beams, TCPE exists not only in the longitudinal direction but also in the lateral direction. Charged particles may leave the central axis to regions outside the central axis. This effect compensates the charged particles that do the opposite way and is called LCPE [24].

Loss of LCPE occurs when the beam half width or radius is smaller than the maximum range of secondary electrons that contribute measurably to the absorbed dose. The smallest field dimension for which LCPE condition exist is related by an important parameter, lateral particle distance (r_{LCPE}) [24].

The field size is often defined by the field diameter at the isocenter and can be determined by the full-width at half maximum (FWHM) of the dose profile in a phantom at the isocenter. For broad beams the field size is equal to the collimator aperture projected at the isocenter. However, for small fields, the FWHM exceeds the collimator aperture projected at the isocenter. If the radius of the field is smaller than r_{LCPE}, the penumbra of the field overlaps with the detector resulting in a sharp reduction in machine output when the field size decreases (figure 3). This effect is energy dependent because the range of secondary electrons is affected by the photon energy [24].
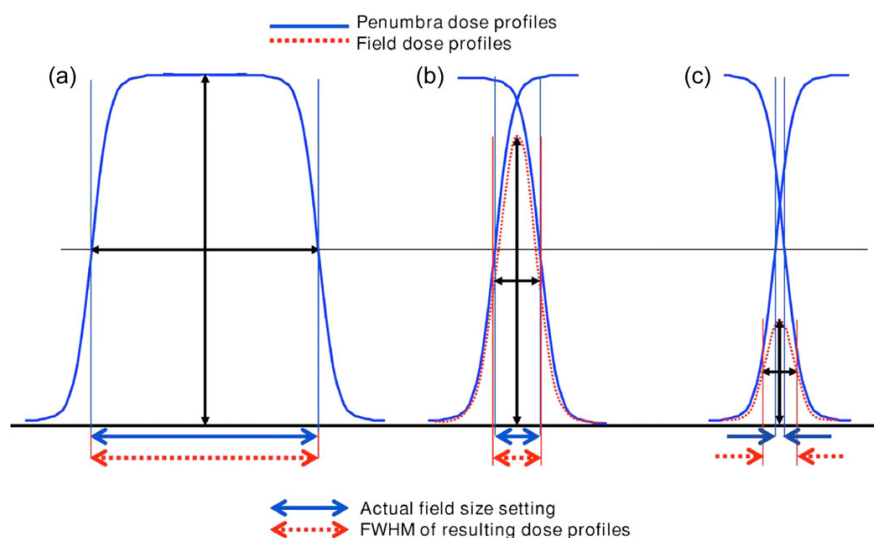
Figure 3: Effect of overlapping penumbrae on the FWHM illustrating the apparent field widening compared to the collimator settings. The blue line corresponds to the ideal field dose profile (ideal FWHM) and the distance marked as red to the real dose profiles. Image adapted from *The physics of small megavoltage photon beam dosimetry* (Pedro Andreo, 2017).

The r_{LCPE} defined by TRS-483 was calculated using Monte Carlo simulations and can be obtained as a function of the photon beam quality index, $TPR_{20,10}(10)$, or $\%dd(10,10)_x$ in centimeters [24]:

$$r_{LCPE} = 8.369 \times TPR_{20,10}(10) - 4.382 \qquad (3.1)$$

$$r_{LCPE} = 0.07797 \times \%dd(10,10)_x - 4.112 \qquad (3.2)$$

3.1.2 Partial source occlusion

The primary photon source has origin in the bremsstrahlung target which has a spot size with finite dimensions. In consequence, there will always be a field size (created by the collimation system) that is occluded by the collimators. This results in photon penumbra overlapping which reduces the output with further reduction of the field size. The width of the beam profile is also increased to a value that does not match the nominal collimator size projected at the isocenter, resulting in an apparent widening of the field. Partial occlusion of the primary photon source influences the particle spectrum, as explained below (3.1.4), and is a source of steep local absorbed dose gradients, both of which can have a large effect on the detector response [24].
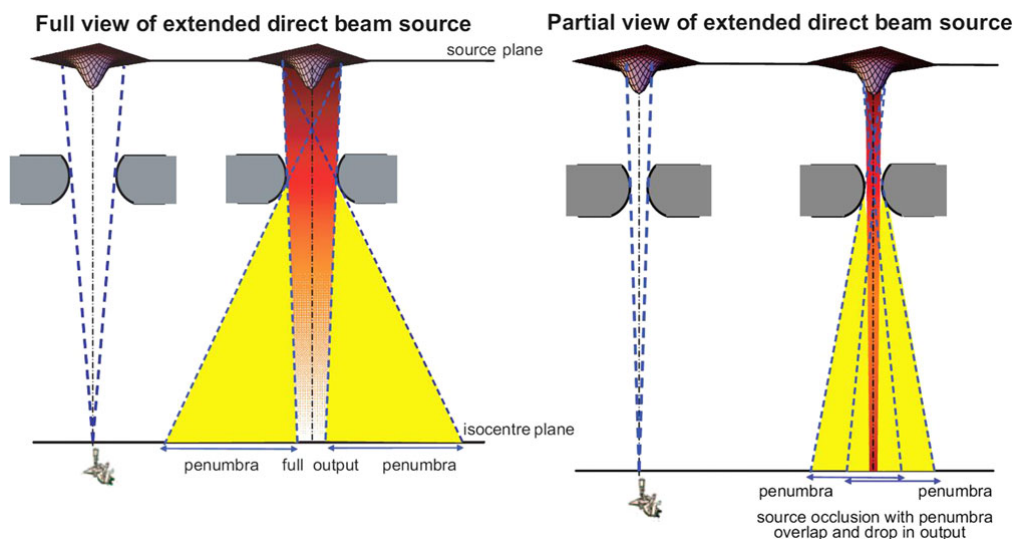
Figure 4: Illustration of the source occlusion effect. Image adapted from *The physics of small megavoltage photon beam dosimetry* (Pedro Andreo, 2017).

3.1.3 Volume effect

The signal generated by the detector is proportional to the average absorbed dose over its sensitive volume and is affected by the homogeneity of the dose over the detection volume. A field is called small if the ionization chamber used for dosimetry becomes too large to give reliable results. Small field conditions can be assumed to exist when the distance of the external edge of the detector volume and the field edge is smaller than

r_{LCPE} in the medium. To avoid this condition, the beam half width or radius has to be at least as large as r_{LCPE} plus half size of the external volume of the detector. [24].

3.1.4   Consequences of decreasing the field size

Two important aspects need to be considered in the dosimetry of small fields when decreasing the field size. The hardening of the energy spectrum and its influence on the water-to-air stopping-power ratios for ionization chamber reference dosimetry [25].

Changes in the energy spectrum of small photon beams arise from two different sources: changes in the treatment head when shaping small fields and changes in the phantom or patient when field size is reduced. The collimator that defines a small field shields photons that are scattered from different components inside the LINAC head including flattening filter (if present) and primary collimator. Thus, the number of low energy photons scattered by the primary collimator, flattening filter and other components in the LINAC head reaching the center of the small field is reduced. The amount of phantom or patient scatter also decreases for small fields when compared to broad fields. In small fields and for most depths, this has a larger effect than the reduced head scatter. Both effects lead to a hardening of the photon energy spectrum at any point of the beam axis with decreasing field size and an increase in the average photon energy (figure 5). This changes the ratio of mass energy absorption coefficients between water and the detector material and a potential change of the stopping power between water and the detector material [24].
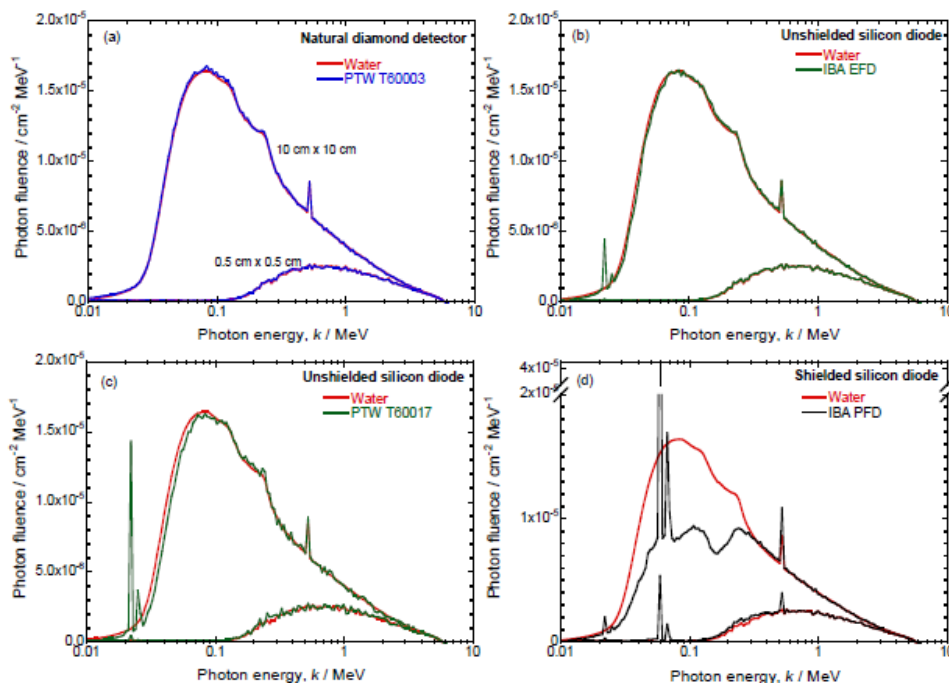
Figure 5: Monte Carlo calculated photon fluence spectra as a function of the photon energy for different detectors at 10 cm depth for 6 MV photon beams for 0.5x0.5 cm^2 and 10x10 cm^2 field sizes. Image adapted from *The physics of small megavoltage photon beam dosimetry* (Pedro Andreo, 2017).

Stopping power ratios are the core component of the processing of converting absorbed dose in the sensitive area of the dosimeter into absorbed dose to medium in the absence of the dosimeter [25]. Although the photon fluence spectrum changes considerably with the field size decrease, the charged particle spectrum produced in water is much less affected. The water to air stopping-power ratio is found to decrease by no more than 0.5% at a depth of 10 cm in a 10 MV photon beam using field sizes between 0.3x0.3 cm^2 and 10x10 cm^2. Even over a range of depths from the depth of maximum dose and 30 cm, the variation does not exceed 1%. [24]

4   Detectors for small field dosimetry

A dosimeter can be defined as an instrument or device that measures, directly or indirectly, the absorbed dose deposited in its sensitive volume. A dosimeter must have at least one physical property that is a function of the measured dosimetric quantity that can be used for radiation dosimetry with proper calibration [26].

The ideal detector requirements for small field dosimetry in radiotherapy would have several properties: high reproducibility and stability, linearity, dose rate and energy response independence and a high spatial resolution.

- In radiation therapy dosimetry the uncertainty of a measurement can be expressed in terms of accuracy and precision. The precision of a measurement specifies the reproducibility of the measurements and can be estimated obtaining repeated measurements. A high precision is associated with a small standard deviation of these measurement results. The accuracy of a measurement is the proximity between the true value and the expectation value of the measured quantity [26];

- Linearity: Ideally, the dosimeter reading should be linearly proportional to the dosimetric quantity. Beyond a certain dose range the dosimeter may behave non-linear. The linearity range and the non-linearity behavior depend on the type of dosimeter and its physical characteristics [26];

- Dose rate dependence: Ideally, the response of a dosimetry system at two different dose rates should remain constant [26];

- Energy dependence: Ideally, the energy response should be flat. In reality, dosimetry systems are calibrated at a specified radiation beam quality and are used over a wider energy range, which means that the variation of the response of a dosimetry system with radiation quality requires correction [26];

- Spatial resolution: Since the dose is a point quantity, the dosimeter should allow the determination of the dose from a small volume. The position of the point where the dose is determined should be well defined [26].

4.1   Detectors for small field measurements

There are several types of dosimeters systems that can be used for dose measurement. However, the choice of a detector for small field dosimetry is a hard task considering all the requirements above described.

No single detector stands out as having characteristics to the ideal one, so, it is advised to use at least two or three different types of detectors suitable for small fields dosimetry [24].

The most common used detector in relative dosimetry is the air-filled ionization chamber, however, there will be always a field size below which volume averaging becomes too large. Bellow that size only liquid ion chambers or solid-state detectors are appropriate for dosimetry of small fields [24].

4.1.1 Ionization chambers

In radiotherapy essentially only one type of chamber is employed: the cavity chamber. Another chamber with relevance to accurate dosimetry is the free-air ionization chamber, used in order to realise air kerma standards that are the basis for the majority of cavity chambers calibrations [22].

Ionization chambers exist in different shapes and sizes, depending on the specific requirements. They have a gas filled cavity surrounded by a conductive wall with a central collecting electrode. An insulator separates the outer wall and the collecting electrode to reduce the leakage current. An outer electrode can be provided to further reduce the chamber leakage. This electrode intercepts the leakage current and allows it to flow to ground, bypassing the collecting electrode [26].

There are basically two types of cavity chambers: cylindrical (thimble type) and parallel-plate (or plane-parallel).

Farmer is a popular cylindrical ionization chamber with $0.6 \, cm^3$ [22]. The chamber construction should be as homogeneous as possible, although the central electrode is aluminium with 1 mm diameter to ensure flat energy dependence. The wall material is of low atomic number (tissue or air equivalent) [26]. Classic ionization chambers have a volume of 0.3-0.6 cm^3. From 0.01 to 0.3 cm^3 are small and from 0.002 to 0.001 cm^3 are considered micro [24].

Parallel-plate ionization chambers have two plane walls, one as an entry window and polarizing electrode and the other as the back wall and collecting electrode. This type of ionization chamber is recommended for dosimetry of electron beams with energies below 10 MeV. They can also be used for surface dose and depth measurements in the build-up region of mega-voltage photon beams [26].

4.1.2 Diamond detectors

Diamond has been considered a suitable material for small volume high-resolution detectors due its radiation hardness, soft tissue equivalence (Z = 6), small size, high-sensitivity and low leakage current [27]. However, it has some disadvantages such as the need of pre-irradiation to stabilize the detector response and its dose rate dependence. Since diamond detectors are manufactured with natural diamonds, the detector response may vary from detector to detector because the sensitive volume

radius can vary between 1.0 and 2.2 mm and the thickness can vary from 0.2 to 0.4 mm. The long manufacturing time, the high cost and the lack of high-quality diamonds make it difficult for their wide use in radiotherapy dosimetry [28].

In the last years, natural diamond detectors have been replaced by artificial chemical vapour deposition (CVD) diamonds [24]. They are attractive due to their relative low-cost availability and reproducibility of natural diamond crystals and unlike natural diamond detectors, CVD diamond detectors reports low dose rate dependence.

4.1.3 Diodes detectors

A silicon diode detector is a p-n junction diode. There are n-Si and p-Si dosimeters, depending on the base material. For radiotherapy dosimetry, only p-Si is suitable since it is less affected by radiation damage and has smaller dark current [26]. During the irradiation electron-hole pairs are created. Conduction occurs by the movement of electrons in the conduction band and by motion of hole states in the valence band. The number of charge carriers is controlled by doping the material with impurities. Depending on the material used, the crystal (typically it is silicon) is given an excess or deficit of free electrons that can carry electrical current. Negative charged current is caused by an excess of electrons and a positively charged current is caused by an deficit in electrons, giving an n-type and p-type semiconductor, respectively [22].

Silicon diodes typical have small sensitive volumes ($< 0.2 \, mm^3$). By this reason, volume averaging effects are small. However, angular dependence is not uniform due to the internal construction and materials used. It is advised to use silicon diodes with the axis of symmetry parallel to the beam axis. Diodes over-respond to low energy photons causing differences in the mass energy absorption coefficients. However, in small fields, contribution of low energy photons is low because the scattered radiation is reduced. There are unshielded and shield diodes. Shield diodes have a high density material (usually tungsten) to absorb low energy scattered photons. The presence of this material increases the fluence of secondary electrons in silicon, increasing the mass energy absorption coefficient of tungsten of low energy photon beams, causing over-response of the diode. For this reason, the use of shielded diodes for OF measurement is discouraged. Increasing the depth of measurement also causes an over-response of shield diodes because the contribution of low energy scattered photons increases with depth. However, the decreased dose-rate at larger depths may lead to an under-response of the diode. For small fields, unshielded diodes are advised [24].

4.2   Other measurement devices

Other types of dosimeters systems can be used for dose measurement in small fields such as: film dosimetry (radiochromic films), thermoluminescence dosimetry (TLD), semiconductor dosimetry (silicon diodes and metal oxide semiconductor field effect transistors (MOSFETs), alanine detectors, plastic scintillator detectors and gels. [26].

These detectors can be used only to validate the beam data obtained, however, they cannot be used for the acquisition of the beam data for the optimization of the algorithms.

4.2.1   Radiochromic films

Radiographic films were known for its superior spatial resolution in 2D but they had to be used with caution because of their known limited absorbed dose range, energy and orientation dependence. They exhibited over-response at low absorbed dose to water levels outside the field, leading to an increased sensitivity in low energy photons. The radiographic film processing and readout procedures were essential for accurate dosimetry [24].

A new approach in film technology are the radiochromic films [22]. They have the advantages of old silver halid films (thinness, ruggedness, permanent record, high spatial resolution) but without numerous disadvantages [29]. Radiochromic films are self-develop and require no chemical processing to get a 2D image of the absorbed dose distribution. They do not require a darkroom for their processing and are insensitive to ambient light but they were reported to be sensitive to ultraviolet radiation [24]. For megavoltage beams they are nearly tissue equivalent because the photon mass energy absorption coefficients and electron mass collision stopping powers are very similar to those of water. They show energy dependence, however, depending on the composition, they have some degrees of energy dependence in the kilovoltage X-Ray region [22].

Post irradiation, radiochromic films development is governed by the polymerization of the diacetylene dye monomers [29]. They can be handled easily and can be read with a regular transmission flat-bed scanner [22]. The readout procedures require accurate absorbed dose to water calibration, careful investigation of spatial non-uniformity of the film and scanner response and dependence on film orientation. Radiochromic films can be used for measurement of absolute absorbed dose in the same way as others dosimeters as long as there is an established conversion of the film response and dose deposited in the film. Typically, that is made with a calibration curve established during calibration process [29]. The film signal continues to develop for several hours after irradiation, therefore, the film scanning must be performed in the same post-irradiation interval as for the calibration film [24].

Radiochromic films have some other disadvantages such as film darkening over time and temperature sensitivity effects, however, its advantages already mentioned here give radiochromic films a considerable advantage over radiographic films. They can be used for measurements of small beam profiles, penumbrae and output factors where changes in spectral components of a beam can occur and affect the output factor measurements.

4.2.2 TLDs

Thermoluminescence consists in the light emission from an insulator or from a semiconductor following the the previous absorption from the source of X-rays or other ionizing radiation. The amount of light emitted is proportional to the absorbed dose by the irradiated material. Since the light intensity emitted by a solid is proportional to the absorbed dose under favourable conditions, the absorbed dose can be evaluated with appropriate calibration [30]. TLDs are well known for absorbed dose audit programmes and *in vivo* dosimetry [24].

4.2.3 MOSFETs

MOSFETs are small silicone field-effect transistors. They can be used to measured dose based on the change in the threshold voltage. Due to its small size, they have an excellent spatial resolution and exhibit little attenuation of the beam, which is useful for *in vivo* dosimetry. However, they are energy dependent and show directional dependence and poor signal to noise ratio. Other disadvantages are its short lifespan and high cost [31].

4.2.4 Alanine

Alanine is a crystalline amino acid in which free radicals are formed at irradiation. The induced radicals by the radiation can be detected by electron spin resonance spectroscopy. The signal is proportional to the amount of radicals in the sample. This substance may be used as a dosimeter because the radical concentration is a function of the absorbed dose [32]. Alanine has the advantage of its density being close to the water so the only perturbation os the volume averaging effect [24] and multiple read-outs of the sample can be performed because the spin resonance spectroscopy does not destroy the signal [32]. However, alanine has low sensitivity (doses of 10 Gy are required to a reproducibility of less than 0.5%) and in general, the necessary instrumentation is not available in hospitals [24].

4.2.5 Plastic scintillator dosimetry system

A scintillator detector system consists of a plastic scintillator embedded in a small polystyrene probe and optically coupled to an optical fibre light guide. A second optic fibre, not connected to the scintillator, is used for subtraction of background and stem effect. Both fibres are connected to two different but identical photomultiplier tubes [33]. Plastic scintillators are almost water equivalent in terms of electron density and they match the water mass stopping power and mass energy absorption coefficient within 2% for the range of energies used clinically. Plastic scintillators are nearly energy and dose rate independent and they have a high spatial resolution due to its small size (about $1\,mm^3$) [26].

4.2.6 Gel dosimetry systems

Gel dosimetry systems are true 3D dosimeters for relative dose measurements. The dosimeter is, at the same time, the phantom that can measure the dose distribution in 3D. Gels are nearly tissue equivalent and can be divided in two categories: Frickle gels and polymer gels. In Frickle gels, Fe^{2+} ions in ferrous sulphate solutions are dispersed throughout gelatin. After irradiation, those ions are converted into Fe^{3+}. The changes in paramagnetic properties can be measured using nuclear magnetic resonance relaxation rates or optical techniques, creating a 3D image of the dose distribution. In polymer gel, nonomers are dispersed in a gelatin or agarose matrix. After irradiation, a polymerization reaction occurs, resulting in a 3D polymer gel matrix that deppends of the absorbed dose. The dose distribution can be obtained with nuclear magnetic resonance, CT scan, optical tomography, vibrational spectroscopy or ultrasound [26].

5 Cone Dose Calculation Algorithm

The CDC algorithm is used in Eclipse™ Cone planning system to calculate the dose when stereotactic cone applicators are used in stereotactic radiosurgery treatments. This algorithm uses Tissue Maximum Ratios (TMR), Off-Axis Ratios (OAR) and Output factors (OF) to determine the absolute dose at any point within the irradiated volume. The following chapters are based on the Eclipse Photon and Electron Algorithms Reference Guide [34].

5.1 Dose Calculation Model

The dose, D, at any point, P, in the beam is determined as:

$$D(r,d,SSD,S) = MU \times DR_{ref} \times OF_{TMR_{max}}(S) \times TMR(d,S) \times \left(\frac{SAD}{SSD+d}\right) \times OAR(r,S)$$

$$(5.1)$$

Where:

- r = off-axis distance to the point of interest;

- d = depth to location of interest along central axis;

- SSD = source-to-skin distance;

- $D(r,d,SSD,S)$ = dose at location of interest;

- MU = monitor units;

- DR_{ref} = reference dose rate = $\left(\frac{D_{ref}}{MU_{ref}}\right)$, where, D_{ref} is the absolute dose (Gy) in water for the reference field size at the reference point at the calibration depth, where MU_{ref} is the MU given to produce the reference dose for calibration;

- $OF(S)$ = output factor = $\left(\frac{D_S}{D_{ref}}\right)$, where D_S is the dose at a specific point on the central axis (at the isocenter) with depth d, when conical collimator, S, is used, and where D_{ref} is the dose measured in the same spatial location and d, as D_S, using reference field size;

- $OF_{TMR_{max}}(S)$ = output factor at $TMR_{max}(S)$, $OF(S) \times \frac{PDD(S,SSD,d_{max})}{PDD(S,SSD,d)} \times \left(\frac{SSD+d_{max}}{SAD}\right)^2$ where d is the depth used to measure $OF(S)$;

- $TMR(d,S)$ = tissue-maximum ratio, $\left(\frac{D_d}{D_{d_{max}}}\right)$, where $D_{d_{max}}$ is the dose at a specific point on the central axis (at the isocenter), with maximum dose depth d_{max} of tissue equivalent material overlaying the point, and where D_d is the dose at the same spatial point with an arbitrary depth, d, of overlaying tissue equivalent material;

- SAD = source-axis distance;
- $OAR(r, S)$ = off-axis ratio, $\left(\frac{D_r}{D_a}\right)$, where, D_a is the dose on the central axis at depth, d, and D_r is the dose at an arbitrary off-axis distance, r, with the same central-axis depth, d.

5.2 Limitations of the Dose Calculation Model

This algorithm has several limitations:

- The algorithm approximates arc beams as multiple static beams by averaging the TMR for each arc. The increment angle is configurable in TPS;
- Tissue inhomogeneity is not considered. All the CT values inside the body of the patient are treated as water and the CT values outside the body are treated as air. This limitation is generally acceptable in the head since most beam paths are through approximately water equivalent densities;
- Obliquity of the beams. The beam axis is assumed to always be normal to the patient contour and no consideration is made for beam obliquity. Due to the small field sizes in radiosurgery, this error is negligible;
- The absence of backscatter near the cavities or where the beam exits is not considered. This results in the displayed dose near the surface being higher than the actual dose;
- The off-axis ratio is assumed to be independent of depth, and only dependent on the distance from radiation source. This assumption is valid since the collimators are small and span only the central area of the LINAC broad beam.

5.3 Required Beam Data Measurements

CDC needs specific measurements for performing dose distributions calculations. The following measurements are required for configuring the algorithm:

- Absolute dosimetry for a reference field;
- Output Factors for all cones relative to absolute dosimetry reference field;
- Tissue Maximum Ratio for at least three cones;
- Off-Axis Ratio for at least three cones.

5.3.1 Absolute dosimetry

Absolute dosimetry follows a code of practice or dosimetry protocol to determine the absorbed dose in Gray at a reference depth in a water phantom. It is expressed in terms

of number of MU per Gray for a given standard field size, source-to.skin distance (SSD) and beam quality [22].

A dosimetry protocol provides the formalism and the data to relate a calibration of a chamber at a standards laboratory to the measured absorbed dose to water under reference conditions. Currently, there are two types of dosimetry protocol available: the protocols based on air kerma in air calibration coefficients; and the protocols based on absorbed dose to water calibration coefficients [26]. TRS-483 provides a code of practice that rely on the absorbed dose to water, N_{D,W,Q_0}, in a standards reference beam of quality Q_0 [24].

The equipment required for reference dosimetry depends on the LINAC reference field size. Machines that can't produce larger fields such as the 10x10 cm^2 from a conventional LINAC might have some restrictions on the equipment that can be used. The limitations include smaller ionization chambers and phantoms with geometries and materials different from those used for conventional reference dosimetry. The accuracy required, however, is still the same [24].

A ionometric dosimeter system includes [24]:

- One or more suitable ionization chambers;

- One or more phantoms with waterproof sleeves if needed;

- An electrometer calibrated in terms of charge or current per scale division;

- One or more stability check devices, specifically designed for the chosen ionization chamber;

- Calibrated thermometer and barometer.

5.3.1.1 Ionization chambers

Photon beams are most commonly calibrated with ionization chambers that are used as relative dosimeters and have calibration coefficients determined either in air or in water and are traceable to a national primary standards dosimetry laboratory (PSDL). The traceability of a calibration coefficient to a national PSDL implies one of the following [26]:

- The chamber was calibrated directly at the PSDL;

- The chamber was calibrated at a secondary standards dosimetry laboratory (SSDL) or at an accredited dosimetry calibration laboratory (ADCL) that traces its calibration to a PSDL;

- The chamber calibration coefficient was obtained through a cross-calibration with another ionization chamber, which as a calibration coefficient measured directly at a PSDL, PSDL or an ADCL.

Only cylindrical ionization chambers that fulfil the specifications of a reference class ionization chamber (table 3) are advised for absolute dosimetry in high energy photon beams.

Table 3: Specifications for reference class ionization chambers for reference dosimetry, from Table 3 of TRS-483.

Parameter	Specification
Chamber settling	Monitoring chamber response with accumulated dose: equilibrium is reached in less than 5 minutes; the initial and equilibrium readings agree within 0.5%.
Leakage	Smaller than 0.1% of the chamber reading.
Polarity effect	Smaller than 0.4% of the chamber reading. The polarity energy dependence is less than 0.3% between ^{60}Co and 10 MV photons.
Recombination correction	1. The correction is linear with dose per pulse. 2. Initial recombination (the dose rate or dose per pulse independent part of the total charge recombination) is below 0.2% at polarizing voltages around 300 V. 3. For pulsed beams, a plot of 1/M_Q (charge reading) vs 1/V (polarizing voltage) is linear at least for practical values of V. 4. For continuous beams, a plot of 1/M_Q vs 1/V^2 is linear, describing the effect of general recombination. The presence of initial recombination disturbs the linearity but this is normally a small effect, which may be neglected. 5. The difference in the initial recombination correction obtained with opposite polarities is less than 0.1%.
Chamber stability	Change in calibration coefficient over a typical recalibration period of 2 years below 0.3%. Same figure fr long term ($>$ 5 years) stability.
Chamber material	Wall material not exhibiting temperature and humidity effects.

5.3.1.2 Correction for influence quantities

Correction for influence quantities is required if an air-filled ionization chamber is used in different conditions from the reference conditions. Influence quantities include the air

density, humidity, polarization and ion recombination correction.

Air density correction

A correction is required because the mass of air in the cavity depends on temperature and pressure. The factor k_{TP} is given by: [24]

$$k_{TP} = \frac{(T + 273.15) \times P_0}{(T_0 + 273.15) \times P}$$ (5.2)

Where T_0 and P_0 are the temperature and pressure for which the calibration coefficient of the ionization chamber is valid (usually 20ºC and 1013.25 hPa). T and P are the temperature and pressure of the air inside the cavity of the ionization chamber at the time of measurement [24].

If the relative humidity is between the range of 20% to 80%, no correction factor is needed for the humidity [24].

Polarity correction

Under the same irradiation conditions, using opposite polarizing potentials, the reading should be the same. Polarity effect occurs when the reading is different. This effect is notable in the build-up region of photon beams of low energies. When a measurable polarity effect occurs, the true reading is taken to be the mean of the absolute values of readings at both polarities. The polarity correction factor, k_{pol}, is given by [26]:

$$k_{pol} = \frac{|M_+| + |M_-|}{2M}$$ (5.3)

Where M_+ and M_- are the chamber readings obtained with positive and negative polarities under identical irradiation conditions and M is the reading using the polarity used routinely [26].

Ion recombination correction

The response of an ionization chamber depends on the radiation dose, dose-rate, chamber polarity and also on the voltage applied between the measuring and collecting electrodes of the chamber [26]. Two effects take place inside the ionization chamber [24]:

- The recombination of ions formed by separate ionizing particle tracks (termed general recombination) that depends on the dose rate, chamber geometry and applied voltage;
- The recombination of ions formed by a single ionizing particle track (termed initial recombination) that depends on the chamber geometry and applied voltage but is

independent of the dose rate.

The correction factor k_s that correct the recombination of ions because of the incomplete collection of charge in the chamber cavity depends if the beam is continuous (like ^{60}Co gamma rays) or pulsed. For a common LINAC, it is given by [24]:

$$k_s = a_0 + a_1 \times \left(\frac{M_1}{M_2} \right) + a_2 \times \left(\frac{M_1}{M_2} \right)^2 \tag{5.4}$$

Where M_1 and M_2 are the measured values at the polarizing voltages V_1 and V_2. The potential V_1 is the normal operating voltage and V_2 is the reduced voltage. Ideally, the ratio V_1/V_2 should be higher than 3. The constants a_0, a_1 and a_2 are the quadratic fit coefficients that depends on the V_1/V_2 ratio for pulsed beams. Those constants are given on table 4 for different V_1/V_2 ratios.

Table 4: Quadratic fit coefficients, for the calculation of k_s by the 'two voltage' technique used in pulsed radiation, as a function of the voltage ratio, V_1/V_2.

V_1/V_2	a_0	a_1	a_2
2.0	2.337	-3.636	2.299
2.5	1.474	-1.587	1.114
3.0	1.198	-0.875	0.677
3.5	1.080	-0.542	0.463
4.0	1.022	-0.363	0.341
5.0	0.975	-0.188	0.214

5.3.2 Output Factors

The radiation output increases with the collimator opening or field size and is expressed in Gy/MU for a conventional LINAC. Typically, it is measured at a fixed point and then the output at z_{max} is determined by using PDD or TMR curves. A higher depth such as 5 or 10 cm is recommended because the influence of the electron contamination is negligible [22].

The measured output factor is assumed to be a product of two independent effects: the phantom scatter factor (S_p) and the collimator scatter factor (S_c) [22]:

$$OF = S_p \times S_c \tag{5.5}$$

Phantom scatter factor depends on the scatter geometry within the phantom or patient and can be modified by varying the beam shaping, SSD and the phantom or patient

shape. Collimator scatter factor depends on the collimator settings and the presence of additional filters [22].

The measured output is normalized to the radiation output of the calibration field size, topically 10x10 cm^2 in a conventional LINAC. Usually, they are presented graphically as a function of equivalent square field sizes. This assumes that the output of a rectangular field is equal to the output of the equivalent square field. If the difference between them is more than 2%, it may be necessary to have separate tables for the output factors for each rectangular field [26]. Since we are dealing with stereotactic cones, this is not a problem and only a measurement for each cone is needed.

5.3.3 Tissue Maximum Ratio

TMR is defined as the ratio of the dose rate, $D(d, S)$, on the beam central axis in the phantom at an arbitrary depth d, to the dose at the depth of maximum dose, $D(d_{max}, S)$ [26]:

$$TMR(d, S) = \frac{D(d, S)}{D(d_{max}, S)} \tag{5.6}$$

Where S is the field size.

For instance, if the measurement is normalized at a different depth (d_{ref}), Tissue Maximum Ratio becomes Tissue Phantom Ratio (TPR) [22].

TMR can be measured in water or solid phantoms by keeping the detector at a constant distance from the source and varying the overlying depth of material [22]. Nowadays, TMR are measured with a water tank that can precisely control the water drain, changing the SSD continuously while the detector is measuring the dose rate at a fixed distance from the radiation source.

5.3.4 Off-Axis Ratio

OAR is defined as the ratio of dose at a point away from the central axis, $D(x, S)$, to the dose at the point on the central axis, $D(0, S)$, at the same depth [22]:

$$OAR(x, S) = \frac{D(x, S)}{D(0, S)} \tag{5.7}$$

Where x is the distance away from the central axis and S is the field size.

The depths and field sizes required to be measured are demanded by the TPS that is being commissioned. Combining central axis dose distribution (TMR) with off-axis data

provides 2D and 3D information of the dose distribution [26].

OAR plays an important role in the determination of the field width. The distance between the 50% OAR values defines the field size. The geometrical field edge (defined by the collimators) and the light field edge must coincide with these 50% points of OAR measurements [22]. However, for small fields, due to the partial occlusion from the source and loss of LCPE, there is a reduction of the beam output and the resulting FWHM is not consistent with the geometrical definition of the field because the FWHM is determined by a lower position on the penumbrae curve. Thus, the field size at 50% relative dose becomes broader than the geometrical field size defined by the collimator [24]. This effective is shown on figure 3 of chapter 3.1.1.

5.4 Generating TMR configuration data from measured data

CDC configuration program fits the data to this equation:

$$TMR(d) = A \times e^{-u \times d} + B \times d^b \times e^{-\left(\frac{d}{d_1}\right)^{10}} \tag{5.8}$$

Where:

- $d_1 = 2 \times (d_{max} + 10mm)$ = power law correction to the exponential function to improve the continuity of the fitted function in the vicinity of $d_{max} + 10mm$;
- d = depth;
- d_{max} = depth of maximum dose;
- A, u, B, b = curve fitting parameters used in CDC configuration.

The parameters A and u are obtained by fitting the exponential function to the TMR data starting from the depth $d_{max} + 10mm$. Subtracting the resulting exponential curve from the data results in a difference curve that is used for obtaining B and b by fitting the power law function to that difference in the interval $d_{max} + 10mm$.

Since it is not necessary to perform TMR measurements for all collimators, the data for each missing collimator can be calculated by power law interpolation and extrapolation from other measurements.

5.5   Generating OAR configuration data from measured data

CDC configuration program applies a curve fit algorithm to the measured data using the following double exponential model:

$$OAR(r) = \begin{cases} 0.5 + 0.5 \times \left(\frac{f(r)-f(r_0)}{f(0)-f(r_0)} \right) & \text{if } (r \leq r_0) \\ 0.5 \times \left(\frac{g(r)-1}{g(r_0)-1} \right) & \text{if } (r > r_0) \end{cases} \tag{5.9}$$

Where:

- r = distance from the central axis to the point where the dose is being calculated;
- r_0 = collimator radius corrected for source-to-target distance;
- $f(r) = \left(1 - e^{a_1 \times (r-r_0)} \right) \times \left(1 - e^{a_2 \times (r-2 \times r_0)} \right)$
- $f(r) = \left(1 - e^{b_1 \times (r_0-r)} \right) \times \left(1 - e^{a_2 \times (-b_2 \times r)} \right)$

Where:

a_1, a_2, b_1, b_2 = curve fitting parameters used in CDC configuration.

Long tails of measured OAR curves are discarded. The equation above fits the data for points which $r < r_{\text{cut off}}$ where $r_{\text{cut off}} = 0.75 \times r_0 + 0.5(cm)$. This approximates the spot where OAR has dropped below 1.5%.

In the case of cone collimator fields, the shape of a rescaled OAR curve exhibits practically no dependence on the source-to-target distance (STD). Hence, for a given cone size, the OAR curves for all STDs can be obtained from one OAR curve by the rescaling equation:

$$OAR(r, STD_2) = OAR \left(\frac{STD_1}{STD_2} \times r, STD_1 \right) \tag{5.10}$$

Before fitting the measured OAR curves, all curves are rescaled to one reference STD, STD_{ref}. The resulting fitting parameters are interpolated by power lawn for all cone sizes. This gives OAR curves for each cone at STD_{ref}. The OAR for any other STD can be obtained by using the equation (5.10) again.

6   Implementation

This work involved three major steps. The first one was data acquisition of TMR, OAR and OF with a synthetic diamond detector for both LINACs, TrueBeam™ STx and Novalis Tx™.

The next major step was the MATLAB® development of a graphical user interface (GUI) for beam data import and process of the measured / golden beam data and CT calibration curve. This application is referred as "Beam Configuration". Another GUI was created to import the phantom or patient DICOM data to verify the MU of each field, with and without heterogeneity correction, based on the data exported from the TPS and the beam data previously processed for both LINACs. This application is called "Stereotactic MU Calculator" and is the main application of this project.

The last step was the verification of the GUIs. First the MATLAB® algorithm was tested against CDC calculations in different scenarios and latter it was tested in different phantoms using ionization chamber.

6.1   Materials

6.1.1   Linear accelerators

Two LINACs, TrueBeam™ STx and Novalis Tx™, with stereotactic cones were studied in this work. All LINACs features were described earlier in chapter 2.2.

The energies used were the ones used clinically for treating patients. For TrueBeam™ STx only energies without flattening filter were used (6 FFF and 10 FFF). For Novalis Tx™, a single energy was used, 6 MV with flattening filter (WFF) in SRS mode.

6.1.2   CT scan

The CT scan used for scanning phantoms and patients was the GE LightSpeed RT 16 from GE Healthcare. The CT calibration curve used was the one that is used for Eclipse™ TPS of IPO Porto at the time of this work.

6.1.3   Detectors and equipment

Absolute dosimetry

A PTW Farmer 30013 (figure 6a) was used for absolute dose measurements of both LINACs, for WFF and FFF energies. This ionization chamber is intended for absolute

dosimetry with a sensitive volume of $0.600\,cm^3$. The chamber has a thimble wall made of 0.09 mm mm thick graphite layer protected by a 0.335 mm acrylic exterior wall. This combination makes the chamber air-equivalent [35].

A PTW UNIDOS E (figure 6b) electrometer was used to read the electric charge accumulated by the ionization chamber. The water tank used was a PTW MP3 with lifting capabilities.

(a) PTW Farmer 30013

(b) PTW UNIDOS E

Figure 6: Ionization chamber and electrometer used for absolute dosimetry. Images from PTW Freiburg GmbH.

Relative beam data acquisition

For TMR, OAR and OF measurements a PTW microDiamond 60019 (figure 8a) was used. This is a synthetic diamond detector nearly water equivalent for all beam energies, it has a very small sensitive volume ($0.004\,mm^3$ with $4\,mm^2$ of active measurement area and 0.001 mm thickness, suitable for all field sizes up to 40x40 cm^2 [36]. This detector is well known for having a high linearity, low angular and negligible dose rate dependence [28]. It needs correction factors below field sizes below 10 mm, since the correction factor is higher than 1% in that range. At very small field sizes the combination of volume averaging and detector material perturbation effects compensate each other leading to low overall output correction factors [37]. The OF correction factors used were the ones described in the TRS-483.

When compared to other detectors used in small field dosimetry, PTW microDiamond 60019 shows a very small deviation of absorbed dose to water starting from 5x5 mm^2 square field sizes [36] as shown in the below figure:
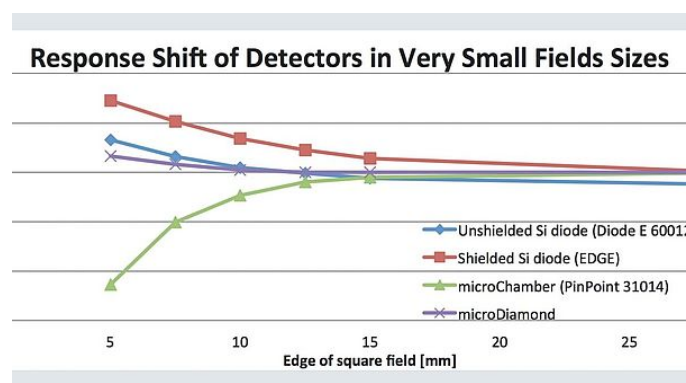
Figure 7: PTW microDiamond response shift compared to others detectors in the market. Image adapted from PTW Freiburg GmbH.

The electrometer used for TMR and OAR was a PTW Tandem (figure 8b) and for OF a PTW UNIDOS E was used (the same for absolute dose measurement).

(a) PTW microDiamond

(b) PTW Tandem

Figure 8: Detector used for relative measurements and electrometer used for TMR / OAR. Images from PTW Freiburg GmbH.

The same water phantom system, shown in figure 9, was used for absolute dosimetry and relative measurements.
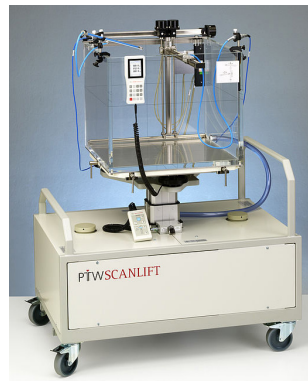
Figure 9: PTW MP3 water tank system used for absolute and relative dosimetry. Image from PTW Freiburg GmbH.

FWHM film measurements

GAFChromic™ EBT3 films (figure 10a) were used to confirm the FWHM diameter of each cone. The film is composed by an active layer with $28\,\mu m$ thick and a matte-polyester substrate of $125\,\mu m$ thick on both sides. The active layer contains a marker dye - which is the active component - and stabilizers among other components that give the radiochromic film its near energy independent characteristic [38]. These radiochromic films have a dynamic dose range from 0.1 Gy to 20 Gy however the optimum interval is from 0.2 Gy to 10 Gy. It also features a symmetrical construction and a anti-Newton ring coating while the previous model (EBT2) did not support [39].

A flatbed scanner Epson Expression 10000XL was used to scan all the films and convert them to digital image, as observed in figure 10b.

(a) GAFChromic™ EBT3 films.

(b) Epson Expression 10000XL scanner.

Figure 10: Radiochromic films and scanner used for cone FWHM confirmation. Images from GAFChromic and Epson product page respectively.

In phantom absolute dose verification

A PTW PinPoint 3D 31016 (figure 11) was used for absolute dose verification in phantoms. It is a small cylindrical ion chamber with $0.016\,\text{cm}^3$ (1.45 mm radius and 2.9 mm length). It has a small polarity effect, small directional response, short ion collection time and a low pre-irradiation dose is required. It is suitable for IMRT, stereotactic beams and can be used also for large fields up to 40x40 cm^2 [40]. OF correction factors from TRS-483 were applied. Due to the field size and the detector size, TRS-483 only includes correction factors below $\pm$ 5%. Values outside this interval are excluded and extrapolation is to be avoided. For this reason, dose verification was performed only for cones with a nominal size equal or above 10 mm.

Figure 11: PTW PinPoint 3D 31016. Image from PTW Freiburg GmbH.

Two phantoms were used to test the algorithms developed. Lucy® 3D QA phantom (figure 12a) from Standard Imaging in a first step was used to verify the dose in the ion chamber positioned at the isocenter. Due to it's almost homogeneity, it was used to verify the algorithms created without heterogeneity correction. Later, in order to verify the heterogeneity correction algorithm, a QUASAR™ thorax phantom (figure 12b) from Modus QA was used. This phantom has cylindrical inserts to simulate lungs, bones and others densities.

(a) Standard Imaging Lucy® 3D QA phantom.

(b) Modus QA QUASAR™ thorax phantom.

Figure 12: Phantoms used for in phantom absolute dose verification. Images from Standard Imaging and Modus QA product page respectively.

6.1.4 Software

Varian Golden Beam Data

Some beam data provided by Varian was used in this work. This is a pre-configured beam data that customers can use in TPS commissioning. It is distributed in w2CAD format or in an Excel spreadsheet. It can be compared to the user measurements and imported and calibrated into the Eclipse™ system.

A w2CAD file (.asc) must contain the measurements in a specific table format and must be saved into a ASCII file.

PTW MEPHYSTO mc^2

Measurements in the water phantom were made using the PTW MEPHYSTO mc^2 suite software and were exported in its proprietary file format.

A mc^2 file (.mcc) it's saved in plain text which means that can be opened and edited without any proprietary software. Each file can contain single or multiple measurements from different measurement types (PDD, TMR or OAR mostly). There is a header for each measurement that contains dozens of data associated with the measurement itself, such as date, measurement type, ionization chamber used, machine, beam characteristics (such as field size, energy) and setup conditions.

Data is saved in a discretized way for each detector position inside the water phantom. The detector position (in x, y or z axis depending on the measurement) and the accumulated charge during a user pre-defined time interval are saved to the MEPHYSTO mc^2 file.

CDC planning system and DICOM format

All the plans for phantoms or patients were created in CDC treatment planning system and were exported in the Eclipse™ workspace in DICOM format (.dcm).

DICOM is a communication protocol and file format. Every DICOM file can store medical

information, image(s) and patient information. The format ensures that DICOM files can be exchanged between two entities or machines that support the DICOM standards [41].

DICOM-RT is an extension of the DICOM protocol that was created to set the standard for data integration and communication between different equipment manufacturers and radiation therapy equipment [42]. There are seven DICOM-RT objects: RT Image, RT Structure Set, RT Plan, RT Dose, RT Beams Treatment Record, RT Brachy Treatment Record, RT Treatment Summary Record, RT Ion Plan and RT Ion Beams [42]. In fact, only three objects are in the scope of this work: RT Structure Set, RT Plan and RT Dose:

- RT Structure Set: defines a set of areas of significance such as target volumes, organ at risk, external contour or other regions of interest. It also defines the regions of interest (ROI) type and its physical properties such as the relative electron density;

- RT Plan: contains every geometric and dosimetric data of the treatment, including the position of the patient, the treatment technique, fractionation scheme, reference points and individual beam characteristics (isocenter, gantry, collimator and couch angles, field size, beam modifiers and accessories used, tolerance table, number of MU, control points, among others);

- RT Dose: contains planar (2D) or volumetric (3D) dose generated by the TPS. It also includes the dose-volume histogram (DVH) and dose statistics.

To satisfy the purpose of this work, only these DICOM-RT objects are required plus the CT scan that is exported also in DICOM format.

MATLAB® developed algorithms

All the algorithms developed during this work were created in MATLAB® R2019a from MathWorks. MATLAB® is a high-level programming language for technical computing. It allows matrix manipulations, function plotting, algorithm implementation, creation of user interfaces and interfacing with other programming languages.

Graphic interfaces were designed and programmed in App Designer and then compiled to a stand-alone executable application that runs on Windows, Linux or macOS.

Variables that are transversal to multiple scripts or GUIs were saved as a MAT-file. MAT-files are binary MATLAB® files that store workspace variables that can be opened, edited and saved again, if desired.

6.2 Methods

6.2.1 Absolute dosimetry

TRS-483 states that reference dosimetry of LINACs where a conventional 10x10 cm^2 can be established should follow TRS-398 protocol.

The reference conditions to determine the absorbed dose to water are the following [43]:

- **SCD:** 100.0 cm

- **Depth:** 5 cm if TPR$_{20,10}$ < 0.7 or 10 cm if TPR$_{20,10}$ ≥ 0.7

- **Field size:** 10x10 cm^2

- **Energy:** 6 FFF and 10 FFF for TrueBeam™ STx and 6X SRS for Novalis Tx™

A SSD of 95 cm with a depth of 5 cm was chosen because it was recommended by the Eclipse Photon and Electron Algorithms Reference Guide [34].

The dose rate of the absolute dosimetry measurements was the same used clinically for radiosurgery treatments: 1400 MU/min for 6 FFF, 1200 MU/min for 10 FFF and 1000 MU/min for 6X SRS.

The absorbed dose to water at the reference depth z_{ref} in water, in a photon beam of quality and in the absence of the chamber, is:

$$D_{w,Q} = M_Q \times N_{D,w,Q_0} \times k_{Q,Q_0} \tag{6.1}$$

Where M_Q is the dosimeter reading corrected for the influence quantities, N_{D,w,Q_0} is the calibration factor in terms of absorbed dose to water for the dosimetry at the reference quality Q_0 and k_{Q,Q_0} is a chamber specific factor which corrects for the difference between the reference beam quality Q_0 and the actual quality used, Q.

If the reference quality Q_0 is ^{60}Co, N_{D,w,Q_0} is denoted by $N_{D,w}$ and k_{Q,Q_0} is denoted by k_Q.

6.2.2 Relative beam data acquisition

All the required measurements for CDC algorithm configuration [34] were performed using the TRS-483 code of practice [24] for relative dosimetry of small fields used in radiotherapy.

The same measurements setup were used for TrueBeam™ STx and Novalis Tx™ LINAC.

As previously stated, a PTW MP3 water tank and a PTW microDiamond 60019 detector were used for the relative beam data acquisition.

The major axis of the detector was aligned parallel with respect to the beam central axis, as recommended by the code of practice, as observed in figure 13 [24].
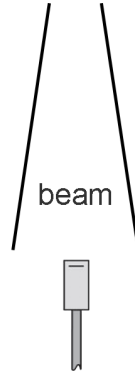
Figure 13: Detector orientation used in relative beam data acquisition. Image adapted from TRS-483.

Another factor that is transversal to all measurements is the jaw size. A square field of 5x5 cm^2 in TrueBeam™ STx and 2x2 cm^2 in Novalis Tx™ was defined for all measurements, to match the jaw size of the reference field.

To ensure that the beam is parallel to the vertical axis of the water tank, a center check was performed at two different depths every time a cone was inserted into the LINAC. No reference ionization chamber was used in OAR and TMR measurements due to the small cone sizes. To minimize the noise of the curves, the acquisition time and the delay time between each measurement was increased and the detector moving speed was decreased.

The dose rate of the relative dosimetry measurements was the same used clinically for radiosurgery treatments: 1400 MU/min for 6 FFF, 1200 MU/min for 10 FFF and 1000 MU/min for 6X SRS.

Output Factors

Accordingly to TRS-483, output factors relate the absorbed dose to water of a clinical field f_{clin} to the reference field, f_{ref}. They are derived from the measured ratio of detectors readings multiplied by an adequate correction that converts the ratio of measured readings into a ratio of values of absorbed dose to water.

The field output factor, $\Omega_{Q_{clin},Q_{ref}}^{f_{clin},f_{ref}}$ is defined by:

$$\Omega_{Q_{clin},Q_{ref}}^{f_{clin},f_{ref}} = \frac{M_{Q_{clin}}^{f_{clin}}}{M_{Q_{ref}}^{f_{ref}}} \times k_{Q_{clin},Q_{ref}}^{f_{clin},f_{ref}} \tag{6.2}$$

Where $M_{Q_{clin}}^{f_{clin}}$ and $M_{Q_{ref}}^{f_{ref}}$ are the readings of the detector in the clinical and reference field, respectively. The readings should already be corrected by the influence quantities.

Output factors readings were performed in the same setup conditions as the reference field:

- **SSD:** 95.0 cm

- **Depth:** 5.0 cm

- **Monitor Units:** 100 MU

- **Cones:** 4, 5, 7.5, 10, 12.5, 15 and 17.5 mm for TrueBeam™ STx and 4, 6, 7.5, 10, 12.5 and 15 mm for Novalis Tx™

- **Energy:** 6 FFF and 10 FFF for TrueBeam™ STx and 6X SRS for Novalis Tx™
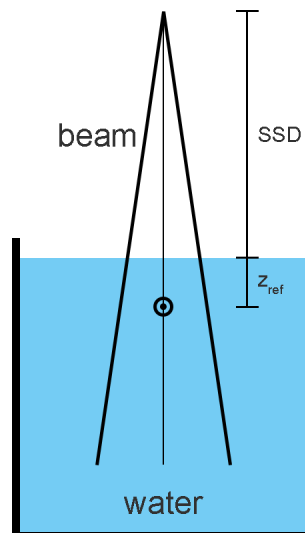
Figure 14: OF scheme.

To apply the field output factor correction, $k_{Q_{clin},Q_{ref}}^{f_{clin},f_{ref}}$, the equivalent square field size of each cone as to be determined using the equation:

$$S_{clin} = r \times \sqrt{\pi} \tag{6.3}$$

Where r is half of the FWHM diameter of the cone.

TRS-483 has several output correction factors depending on the machine, energy and detector used. It is worth to mention that the minimum field size recommended for measurements is such that the detector specific output correction factor is not greater that $\pm 5\%$ for a particular machine. For this reason, TRS-483 does not include $k_{Q_{clin},Q_{ref}}^{f_{clin},f_{ref}}$ values outside this interval.

For PTW microDiamond 60019 detector, there are correction factors available up to 4x4 mm^2 square fields. This is a problem because the smallest cone of both LINACs has a nominal diameter of 4 mm what means that its equivalent square field size is around 3.54x3.54 mm^2 and the last correction factor available is for the 4x4 mm^2 square field. To overcome this, extrapolation was used for the smallest cone.

Field output correction factors for PTW microDiamond 60019 were fitted into a two term exponential curve:

$$k_{Q_{clin},Q_{ref}}^{f_{clin},f_{ref}}(s) = a \cdot e^{b \cdot s} + c \cdot e^{d \cdot s} \tag{6.4}$$

Where s is the equivalent square field size and a, b, c, d are the parameters to be fitted.

Tissue Maximum Ratio

TMR is the ratio of absorbed dose at any depth along the beam axis to the absorbed dose at depth of maximum dose. During the measurement, the STD should be fixed. The build-up depth is defined by changing the water level of the tank.

Setup used for TMR measurements:

- **STD:** 100.0 cm (constant)
- **Depth:** From surface up to 20 cm
- **Cones:** At least 3 cones for each LINAC
- **Energy:** 6 FFF and 10 FFF for TrueBeam™ STx and 6X SRS for Novalis Tx™

Off-Axis Ratio

OAR is the ratio of absorbed dose at any point to the absorbed dose on the beam axis at the same depth.

Setup used for OAR measurements:

- **STD:** 100.0 cm
- **Depth:** 5.0 cm
- **Cones:** 4, 5, 7.5, 10, 12.5, 15 and 17.5 mm for TrueBeam™ STx and 4, 6, 7.5, 10, 12.5 and 15 mm for Novalis Tx™
- **Energy:** 6 FFF and 10 FFF for TrueBeam™ STx and 6X SRS for Novalis Tx™

6.2.3 FWHM film measurements

Calibration curve

An EBT3 film calibration curve was acquired in the TrueBeam™ STx LINAC for 6 FFF energy. The MU and the corresponding expected dose to the film are given on table 5. The film scan was performed 24 hours posteriorly to the irradiation in an Epson Expression 10000XL with a resolution of 72 dpi and 48 bit color depth (16 bits for each colour channel) without any image enhance. The same settings were used in the film acquisition of each cone.

Table 5: Number of MU and the expected absorbed dose by the films, in the central region of the beam (CAX).

MU	Expected Dose (Gy)	MU	Expected Dose (Gy)
0	0.000	800	6.754
50	0.422	1000	8.443
100	0.844	1500	12.665
200	1.689	2000	16.886
400	3.377	2500	21.108

The films irradiated were scanned and saved in tagged image file format (TIFF), since this is a lossless format. An algorithm was developed in MATLAB® to create the calibration curve and analyze the images.

To create the calibration curve, a MATLAB® script reads the image and returns the mean pixel value (MPV) of a central area in the image with 50x50 pixels^2 area. This area is approximately 1.66x1.66 cm^2 if we consider the resolution used (72 dpi). It is important to analyse a small central area of the image because TrueBeam™ STx is a FFF machine and the dose outside the central region of the beam decreases faster than a WFF machine like Novalis Tx™, as shown in the beam profiles of the next figure:
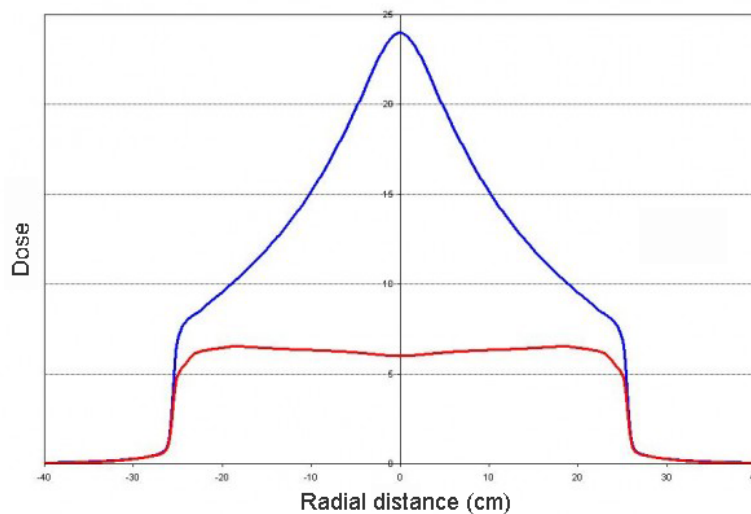
Figure 15: Off-axis profile of a FFF (blue) and WFF (red) beam. Image adapted from *Varian TrueBeam: The UAB experience* (Richard Popple, 2013).

Only the red channel was used because it is the ideal channel for the dose ranges used to measure the FWHM cone diameter [44]. Calibration curve goes up to 21.108 Gy but the absorbed dose by the radiochromic films in the FWHM cone diameter measurement was lower than 10 Gy. The red channel is the channel that has the highest sensitivity for low doses. This can be demonstrated computing the first derivative of each colour channel in the calibration curve, as shown in figure 16.
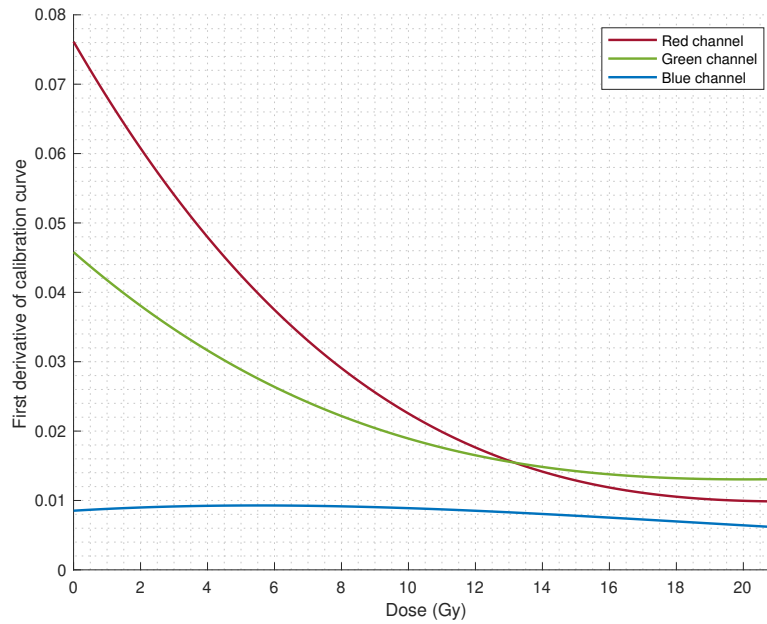
Figure 16: First derivative of EBT3 calibration curve for all colour channels.

The mean pixel value (MPV) of the red channel of each image, including the background film that has no exposure, are then used to return the netOD for each film with the equation:

$$netOD = -log_{10} \times \left(\frac{\text{Pixel MPV}}{\text{Background Pixel MPV}} \right) \tag{6.5}$$

Where $\text{Background Pixel MPV}$ is the MPV of the unexposed film.

The obtained netOD values are then fitted in a 4th polynomial degree to create the calibration curve.

$$\text{Dose (Gy)} = a \times netOD^4 + b \times netOD^3 + c \times netOD^2 + d \times netOD \tag{6.6}$$

The function coefficients a, b, c and d were found with the help of the MATLAB® Curve Fitting Toolbox.

Finally, the script saves a curve fit object containing the polynomial model and the coefficients of each colour channel in a MATLAB® MAT-File.

Film irradiation and analysis

As described earlier in the chapter of Physics of small fields (chapter 3.1), if the radius of the field is smaller than r_{LCPE}, the penumbra of the field overlaps with the detector, resulting in machine output reduction. This causes an increase in the FWHM measured by the detector, exceeding the collimator aperture projected at the isocenter. To confirm the FWHM measured with the PTW microDiamond, film irradiation was performed in the TrueBeam™ STx for 6 FFF energy.

Films were placed between water solid slabs (PTW RW3) at the isocenter with 5 cm of build-up (5 slabs). To provide back-scatter, a total of 10 slabs were placed below the films. Every film was irradiated with 1000 MU and scanned 24 hours after the irradiation, in the same orientation as the calibration curve.

FWHM of each cone through film irradiation was obtained in a developed MATLAB® script. The script does the following:

1. Imports the calibration curve that was saved previously in a MAT-File.

2. Imports the background and irradiated scanned films and selects only the red channel.

3. Assigns a netOD value of each pixel of the irradiated image using the equation:

$$netOD = -log_{10} \times \left(\frac{\text{Pixel Value}}{\text{Background Pixel MPV}} \right) \qquad (6.7)$$

4. Converts each pixel of the image to absolute dose with equation (6.6).

5. Creates a binary image of the red channel. The threshold used is 50% of maximum dose. The resulting binary image should have only with 2 regions: the region with $\geq$ 50% of maximum dose and the region with $<$ 50% of maximum dose.

(a) 48-bit colour image   (b) 16-bit greyscale image   (c) 1-bit monochrome image
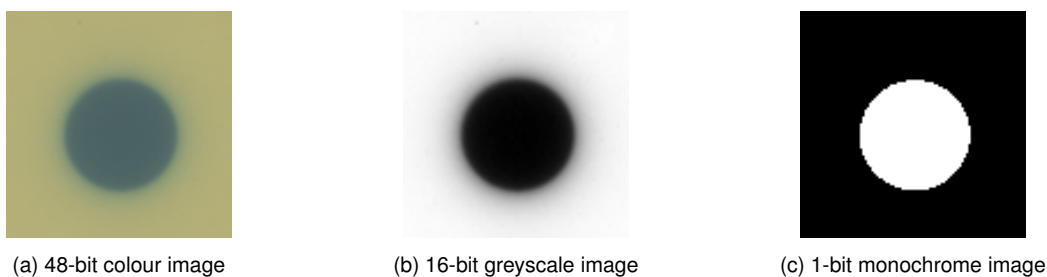
Figure 17: Example of a EBT3 film scan of a single cone containing all channels (a); only the red channel (b); and the resulting binary image (c) containing two regions: the region equal or above 50% of maximum dose (white) and the region below 50% of maximum dose (black).

6. Retrieves the diameter of the region that contains the irradiated area with $\geq$ 50% of maximum dose. The diameter is calculated based on the region area:

$$\text{Diameter (pixels)} = \sqrt{4 \times \frac{\text{Area (pixels}^2)}{\pi}} \qquad (6.8)$$

7. The diameter is then converted from pixels to mm based on the image resolution:

$$\text{Diameter (mm)} = \text{Diameter (pixels)} \times \frac{25.4 \text{ (mm/inch)}}{\text{Image Resolution (pixels/inch)}} \quad (6.9)$$

Since the image resolution is always the same, 72 pixels per inch, the equation (6.9) is reduced to:

$$\text{Diameter (mm)} = \text{Diameter (pixels)} \times 0.3527(7) \left(\frac{\text{mm}}{\text{pixels}} \right) \quad (6.10)$$

The diameter obtained with the above equation is the cone FWHM.

Step 3 to 7 are repeated for each irradiated film.

6.2.4 Beam Configuration application

"Beam Configuration" was created to store reference conditions and absolute dose calibration of each LINAC and energy; import, visualize and process beam data acquired from measurements or golden beam data provided by Varian; and import the CT calibration curve of the CT scanner. Two "Beam Configuration" applications were built, one for TrueBeam™ STx and another for Novalis Tx™.

The goal of this application is to save a MAT-File with all above data to later be used in the '"Stereotactic MU Calculator". Every time a change is made in CDC algorithm that affects beam data, absolute dose calibration or CT calibration curve, a new MAT-File should be created with the new data.

The application has 5 main tabs:

- Parameters tab: machine parameters, reference conditions and absolute dose calibration.
- TMR: to import, visualize and process TMR from measurements / Varian golden beam data.
- OAR: to import, visualize and process OAR from measurements / Varian golden beam data.
- OF: to import output factors values and visualize the curve generated.
- CT calibration: to import CT calibration curve values (housfield units (HU) and the corresponding relative electron density (RED)).

6.2.4.1 Parameters

Parameters tab is the first tab to be filled before the beam data import. It contains specific values that are important for beam data processing. There are a total of six textbox groups including one for comments. Some textboxes have predefined values that need to be confirmed by the user.

Figure 18: Beam Configuration application - Parameters tab overview.

Machine Constants

Source-axis distance (SAD) is the only constant that needs to be filled. It is 1000 mm for conventional radiotherapy LINACs and it will not change for TrueBeam™ STx or Novalis Tx™. However, the variable is not hard-coded in the software source-code because in the future this application might be used in non-conventional LINACs where SAD is not 1000 mm.

Table 6: Parameters Tab - Machine Constants.

Description	Default Value	Unit
Source-axis distance	1000	mm

Reference Conditions

Reference conditions used in absolute dosimetry such as field size, source to phantom distance, calibration depth, dose at calibration depth and MU at calibration depth are required.

Default values of reference field size, source to phantom distance and calibration depth are the same used for TrueBeam™ STx and Novalis Tx™ calibration at the time of this work.

Table 7: Parameters Tab - Reference Conditions.

Description	Default Value	Unit
Absolute dose reference field size	100	mm
Absolute dose calibration source-phantom distance	950	mm
Absolute dose calibration depth	50	mm
Reference dose at calibration depth	0	Gy
Reference MU at calibration depth	0	MU

Energy

Energy currently being configured can be changed in a drop-down menu and depends on the LINAC. For TrueBeam™ STx 6 FFF and 10 FFF are available. For Novalis, only 6X SRS MV is available. There is a textbox with the depth of maximum dose that is automatically calculated based on the energy chosen. For 6 FFF or 6X SRS MV it is 15 mm and for 10 FFF is 25 mm.

Table 8: Parameters Tab - Energy.

Description	Value(s)	Unit
Energy	6 or 10	MV
Depth of maximum dose	15 or 25	mm

OAR settings for Varian golden data and Mephysto data

There are two groups of textboxes where the user can select the SSD and depth accepted from OAR measurements. One textbox is for Varian golden data and another is for Mephysto data. This was introduced because some OAR data files may include multiple measurements at different SSDs/depths and only one SSD and depth is required.

Additionally, there is a textbox where the user can select a new SSD if the measurement was taken at a different SSD from the planned. The computation of new OAR measurements at a different SSD is only a geometric change and uses the equation (5.10).

Table 9: Parameters Tab - OAR Settings (Golden Data).

Description	Default Value	Unit
SSD accepted	1000	mm
Depth accepted	50	mm
Rescale SSD to	950	mm

Table 10: Parameters Tab - OAR Settings (Mephysto Data).

Description	Default Value	Unit
SSD accepted	950	mm
Depth accepted	50	mm
Rescale SSD to	950	mm

6.2.4.2 TMR

TMR tab allows importing TMR from Varian golden beam data in its proprietary w2CAD file format or from measurements saved in a Mephysto mc^2 file. The user can apply linear or exponential curve fitting and can visualize graphically the TMR data points measured and the interpolated curve.

Importing Varian golden beam data for Novalis Tx™ is disabled because Varian does not provide golden data for Brainlab stereotactic cones.

Figure 19: Beam Configuration application - TMR tab overview.

Varian golden beam data import

Only ASCII files with .asc extension that follows w2CAD file format are accepted by the application. The user must verify that all measurements being imported are from the correct energy. TMR from all cones should be imported and none can be duplicated. Import of single and multiple files is supported.

The application will check some parameters in the file header in order to verify if the data being imported was correctly acquired. These parameters, also known as flags, are read from the available data. Each flag stores a parameter such as the beam type, measurement type, measurement axis, field size and other important parameters depending if the beam data is OAR or TMR.

The following parameters are checked while importing TMR from Varian golden beam data files:

Table 11: Varian golden beam data required flags for TMR measurements

Flag Name	Description	Accepted Value
BMTY	Beam Type	PHO
TYPE	Measurement Type	TMR
AXIS	Measurement Axis	Z
FLSZ	Field Size	Valid nominal cone size

If one of the flags has another value from the accepted, import beam data skips the current measurement being read and continues to the next one, if available.

Mephysto beam data import

The application accepts Mephysto mc^2 files saved with .mcc extension. The user must verify if is importing the measurement for the energy chosen. Only 3 measurements from different cones are required. The remaining ones are obtained through interpolation and extrapolation. As with Varian golden beam data import, single or multiple files can be imported at the same time and there no can be measurements repeated for the same cone.

The following parameters are checked while importing TMR from Mephysto beam data:

Table 12: Mephysto beam data required flags for TMR measurements

Flag Name	Description	Accepted Value
SCAN_CURVETYPE	Measurement Type	TPRCURVE
FIELD_INPLANE	Field size inplane	Valid nominal cone size
FIELD_CROSSPLANE	Field size crossplane	Valid nominal cone size

Flag FIELD_INPLANE should be equal to FIELD_CROSSPLANE. If the measurement found is not a TPR curve or if the field size in crossplane or inplane is not the same, the import beam data skips the current measurement being read and continues to the next one, if available.

Beam data processing

Raw data imported from Varian golden beam data or from Mephysto data are interpolated to 1.0 mm spacing. A linear or exponential curve fit is applied, depending on the user choice.

The following interpolation methods are available:

- Linear
- Linear + Smooth
- Exponential

Linear

In linear interpolation data is interpolated to 1.0 mm spacing between measurements and no more processing is applied. It is recommended to be used in already smoothed curves such as measurements imported from Varian golden beam data.
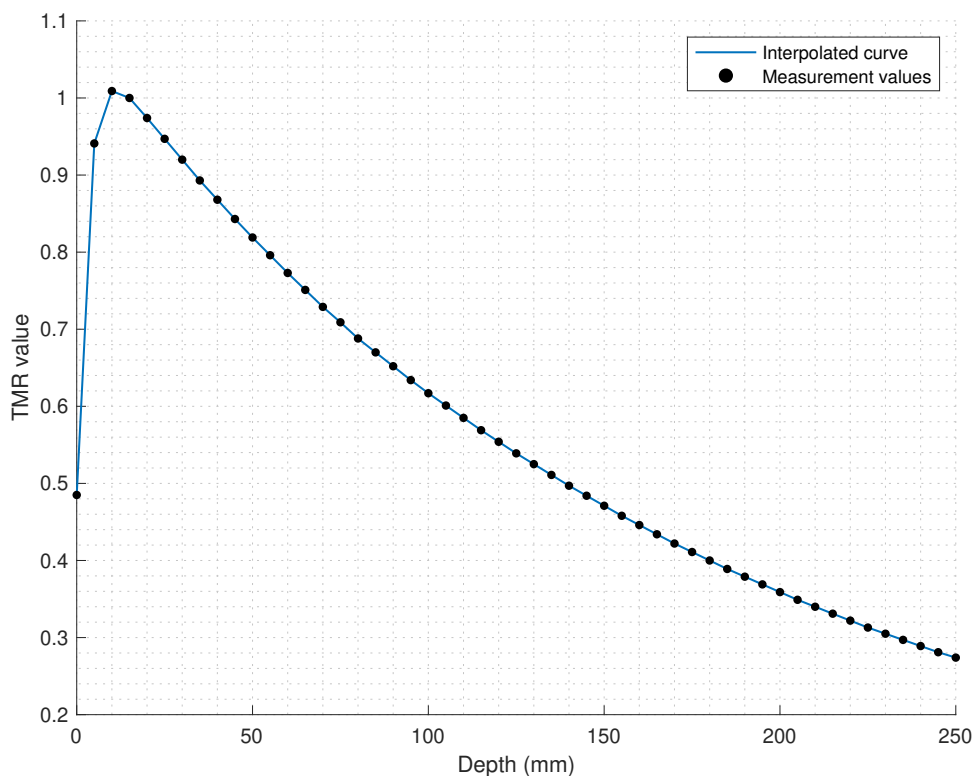
Figure 20: TMR curve of a measurement taken from Varian golden beam data with a measurement spacing of 5.0 mm (black dots) and the interpolated curve with 1.0 mm spacing (blue line).

Linear + Smooth

Linear + Smooth interpolation method interpolates measurements to 1.0 mm spacing and smooths the curve with a local regression method using weighted linear least squares and a 2nd degree polynomial model. It is recommended to be used in noisy TMR curves that have been acquired without a reference detector and have not been smoothed yet.
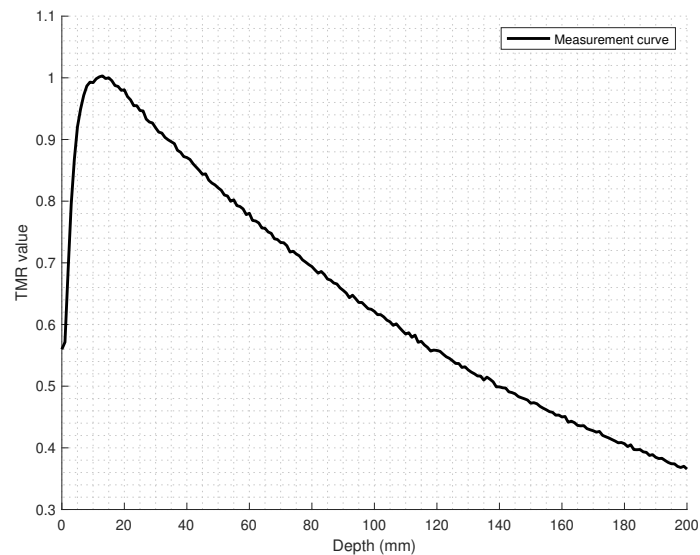
Figure 21: TMR curve of a measurement taken from Mephysto data without smoothing.
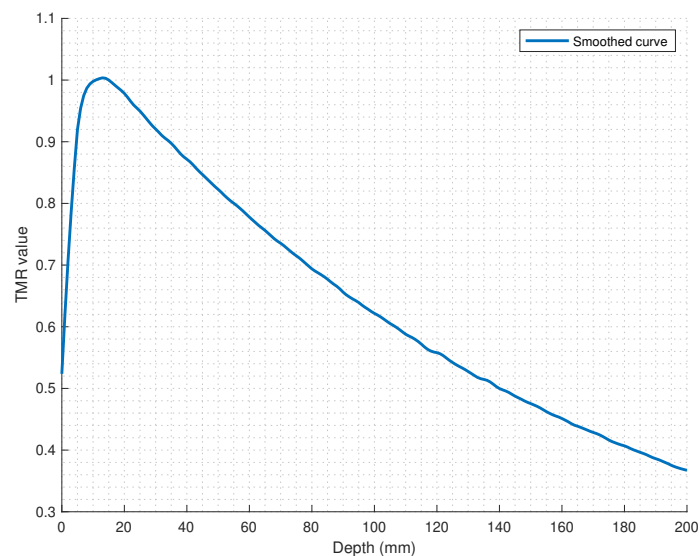
Figure 22: TMR curve of a measurement taken from Mephysto data with smoothing.

Exponential

Exponential curve fit applies a two-term exponential model to the measured values. It is useful to eliminate all the noise from TMR curves. Output curves using this method are smoother than the method explained above because the decay past the depth of maximum dose is exponential.

The model applied is the following:

$$\text{TMR}(\text{depth}) = a \cdot e^{b \cdot \text{depth}} + c \cdot e^{d \cdot \text{depth}} \tag{6.11}$$

Coefficients a, b, c and d are automatically determined based on the TMR measurement being interpolated.

After the coefficients determination, a new TMR curve of 1.0 mm spacing between measurements is generated.
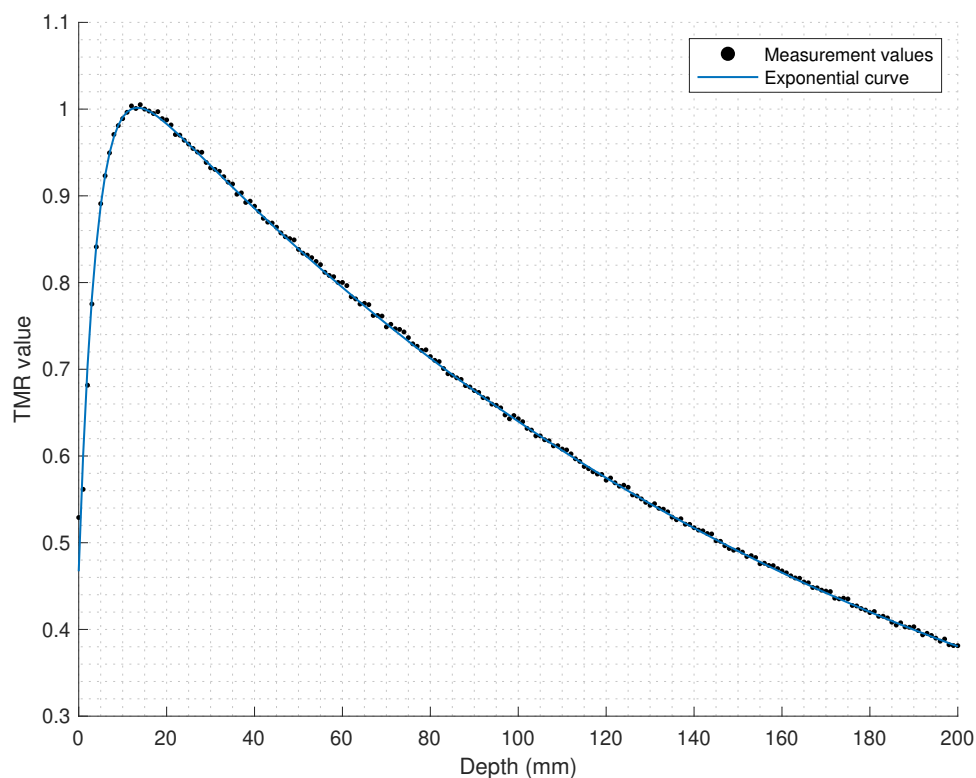
Figure 23: TMR curve of measurement taken from Mephysto data (black dots) with a exponential curve fit applied (blue line).

Once the curve fitting method is applied, TMR curves for missing cones are generated. This is only valid from measurements taken from Mephysto data because all measurements from Varian golden beam data should be imported.

Generating a TMR curve for a missing cone is done with interpolation and extrapolation. For each depth, TMR values of measured cones are fitted into a two-term exponential model and the coefficients are determined. TMR values for missing cones are then generated with a equation similar to equation (6.11):

$$\text{TMR(S)} = a \cdot e^{b \cdot \text{S}} + c \cdot e^{d \cdot \text{S}} \tag{6.12}$$

Where S is the nominal cone size and a, b, c and d are the curve coefficients.
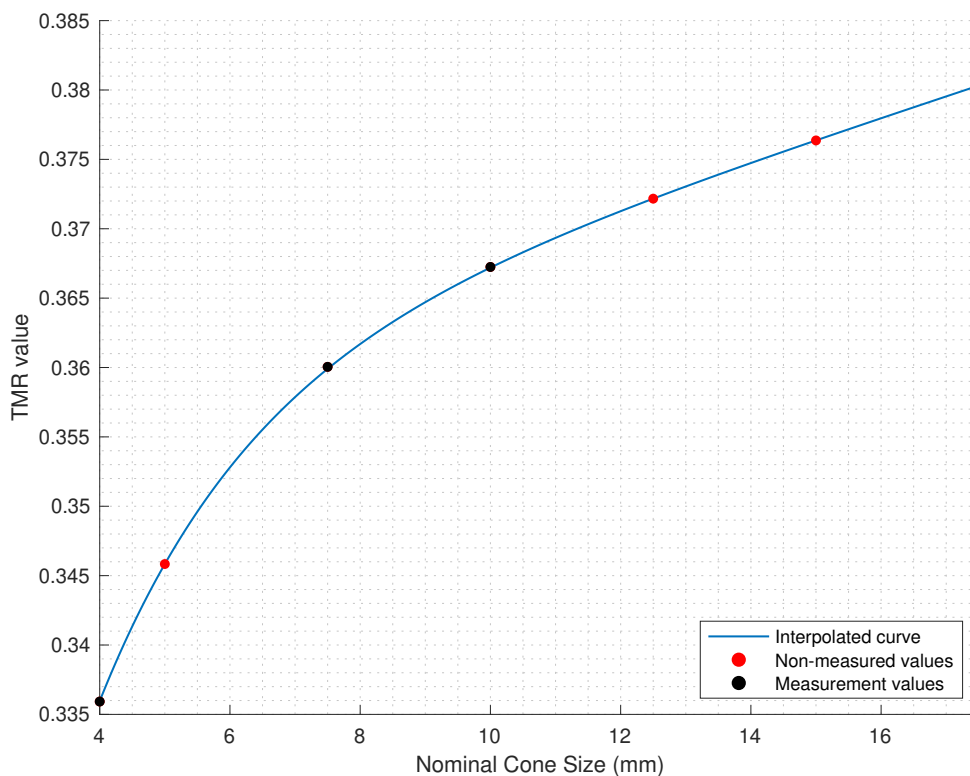
Figure 24: TMR values in function of nominal cone size for a depth past the depth of maximum dose. Measured TMR values are displayed as black dots and the interpolated TMR values for missing collimators are displayed as red dots. The exponential curve (blue line) was generated from measured TMR values (displayed as black dots).

In order to increase the accuracy, TMR for the smallest and largest cone should be provided. This way, only interpolation is required to generate TMR curves for missing collimators and no extrapolation is made. User should keep in mind that extrapolation of TMR curves for the smallest or largest cone might lead to a less accurate generated TMR curve because the fit model applied is valid only on the range of the cones used. Loss of accuracy can occur because extrapolation of the smallest or the largest cone using data from intermediate cones is a prediction from the model.

In the end of TMR data processing, the application ensures that TMR curves are

normalized to the depth of maximum dose (d_{max}) chosen in Parameters tab:

$$TMR(d, S) = \frac{D(d, S)}{D(d_{max}, S)} \tag{6.13}$$

Where S is the nominal cone size, $D(d, S)$ is the TMR value at depth d and $D(d_{max}, S)$ is the TMR value at the depth of maximum dose.

6.2.4.3 OAR

OAR tab allows importing OAR from Varian golden beam data in its proprietary w2CAD file format or from measurements saved in a Mephysto mc^2 file. The user can visualize graphically the OAR data points measured and the interpolated curve. Unlike TMR beam data import, the user can't apply a curve fit to OAR imported data. All measurements are interpolated linearly.

Importing Varian golden beam data for Novalis Tx™ is disabled because Varian does not provide golden data for Brainlab stereotactic cones.
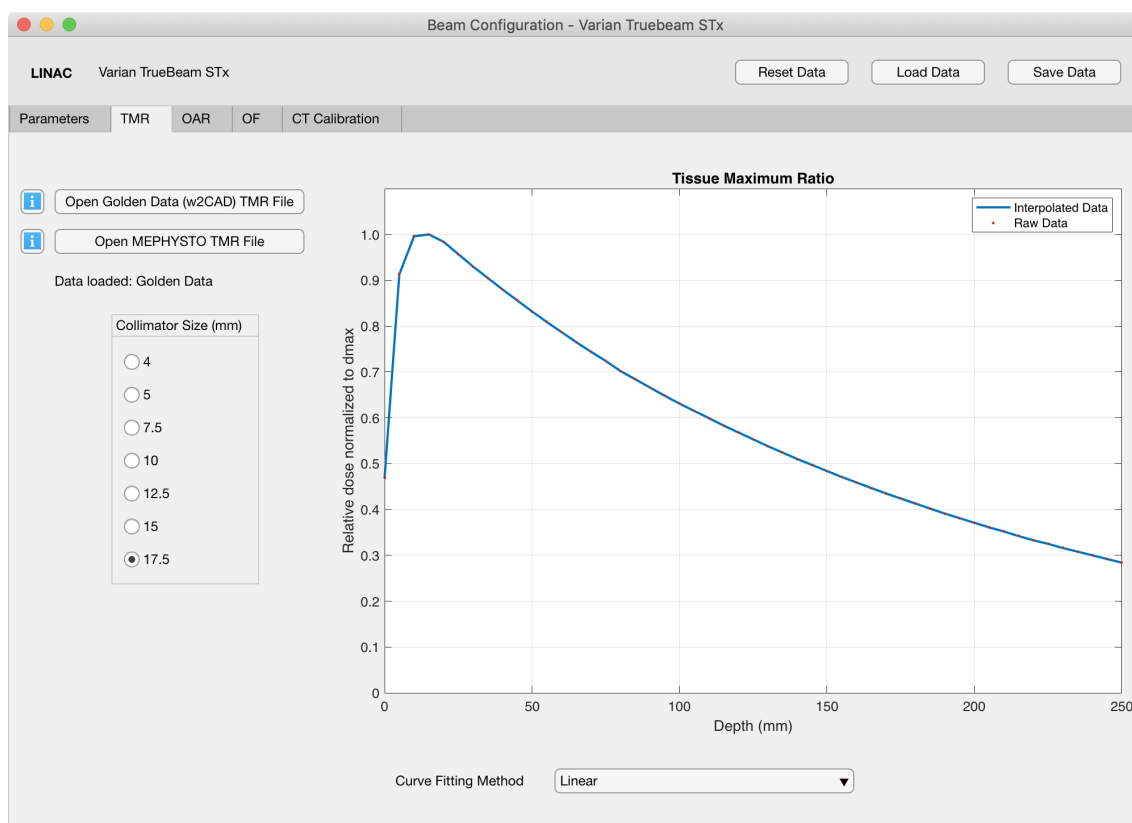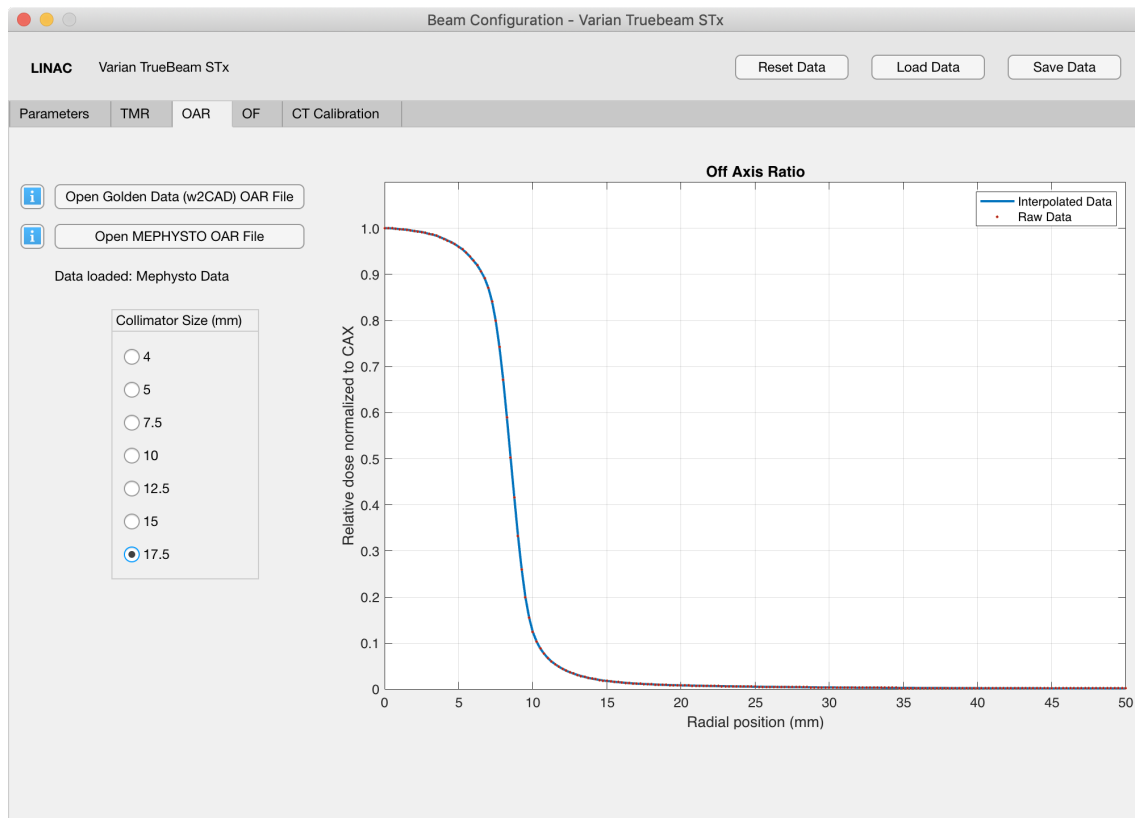

Figure 25: Beam Configuration application - OAR tab overview.

Varian golden beam data import

Only files with .asc extension that follows w2CAD file format are accepted by the application. The user must verify that all measurements being imported are from the correct energy. OAR from all cones should be provided and none can be duplicated. Import of single and multiple files is supported.

The application will check some parameters in the file header in order to verify if the data being imported was correctly acquired.

Table 13: Varian golden beam data required flags for OAR measurements

Flag Name	Description	Accepted Value
BMTY	Beam Type	PHO
TYPE	Measurement Type	OPP
AXIS	Measurement Axis	X or Y
FLSZ	Field Size	Valid nominal cone size
SSD	SSD	Same chosen in Parameters tab
DPTH	Depth	Same chosen in Parameters tab

If one of the flags has another value from the accepted, import beam data skips the current measurement being read and continues to the next one, if available.

Mephysto beam data import

The application accepts Mephysto mc^2 files saved with .mcc extension. The user must verify if is importing the measurement for the energy chosen. Measurements from all cones are required. As with Varian golden beam data import, single or multiple files can be imported at the same time and there no can be measurements repeated for the same cone.

The following parameters are checked while importing beam data:

Table 14: Mephysto beam data required flags for OAR measurements

Flag Name	Description	Accepted Value
SCAN_CURVETYPE	Measurement Type	INPLANE_PROFILE or CROSSPLANE_PROFILE
FIELD_INPLANE	Field size inplane	Valid nominal cone size
FIELD_CROSSPLANE	Field size crossplane	Valid nominal cone size

Flag FIELD_INPLANE should be equal to FIELD_CROSSPLANE. If the measurement found is not a OAR curve or if the field size in crossplane or inplane is not the same, the import beam data skips the current measurement being read and continues to the next

one, if available.

Beam data processing

Raw data imported from Varian golden beam data or from Mephysto data have different processing. Golden beam data is less processed because it already comes with a equal spacing between measurement points and profiles comes cut in half. Averaging both sides of profiles and cut in half is a common technique in profiles acquired with stereotactic cones because profiles are assumed to be symmetrical on both sides.

Varian golden beam data processing

Varian golden beam data for Varian stereotactic cones is presented in 3 different SSDs (800, 900 and 1000 mm) and one depth (50 mm). User can choose the SSD to be imported in the Parameters tab. Profiles are recommended to be rescaled to a SSD of 950 mm because this SSD ensures that the measurement is taken at 1000 mm from the source (the distance at which the field size is defined). However, the user can choose a different SSD in the Parameters tab, if desired.

Profile rescaling is made as following:

$$OAR(r, SSD_2) = OAR\left(\frac{SSD_1}{SSD_2} \times r, SSD_1\right) \tag{6.14}$$

Where r is the radial distance from CAX, SSD_1 is the SSD from the measurement and SSD_2 is the new SSD.

Mephysto data processing

OAR curves from Mephysto data files requires more processing if OAR profiles are acquired without any post-processing in Mephysto software. Mephysto allows to space measurement points equally and allows to average negative and positive sides of beam profiles. However, the developed application ensures that OAR profiles are correctly processed if it was not done previously in Mephysto software.

OAR measurements from Mephysto data are interpolated to a 0.25 mm spacing because using an equal spacing facilitates the next post-processing steps. Spacing distance of measurement data points should be low enough to not compromise the shape of the beam profile, especially in the penumbra region. The smallest the spacing distance of the measurements, the better the penumbra definition.

The next step is the removal of the negative side of beam profiles. To cut the beam profile in half, the negative side is averaged with the positive side:

$$OAR = \frac{OAR_- + OAR_+}{2} \tag{6.15}$$

Where OAR_- and OAR_+ are the negative and positive OAR measurement values of the beam profile, respectively. This is applied to both crossplane and inplane profiles, if they were imported. Then they are averaged:

$$OAR = \frac{OAR_{inplane} + OAR_{crossplane}}{2} \tag{6.16}$$

The resulting beam profile is then rescaled to a different SSD, if it was chosen in Parameters tab, using equation (6.14).

Final data processing

Finally, all measurements from Varian golden beam data or from Mephysto data are interpolated linearly with a 0.1 mm spacing and normalized to the central axis (CAX):

$$OAR(x, S) = \frac{D(x, S)}{D(0, S)} \tag{6.17}$$

Where x is the distance away from the central axis, S is the field size, $D(x, S)$ is the OAR value at a point away from the CAX and $D(0, S)$ is the OAR value at CAX.

6.2.4.4 OF

OF tab allows introducing OF values for the current LINAC and energy being configured. Field output correction factors should be applied to the data introduced. A two-term exponential curve fit is applied to the data. The user can visualize graphically the OF values introduced and the interpolated curve.
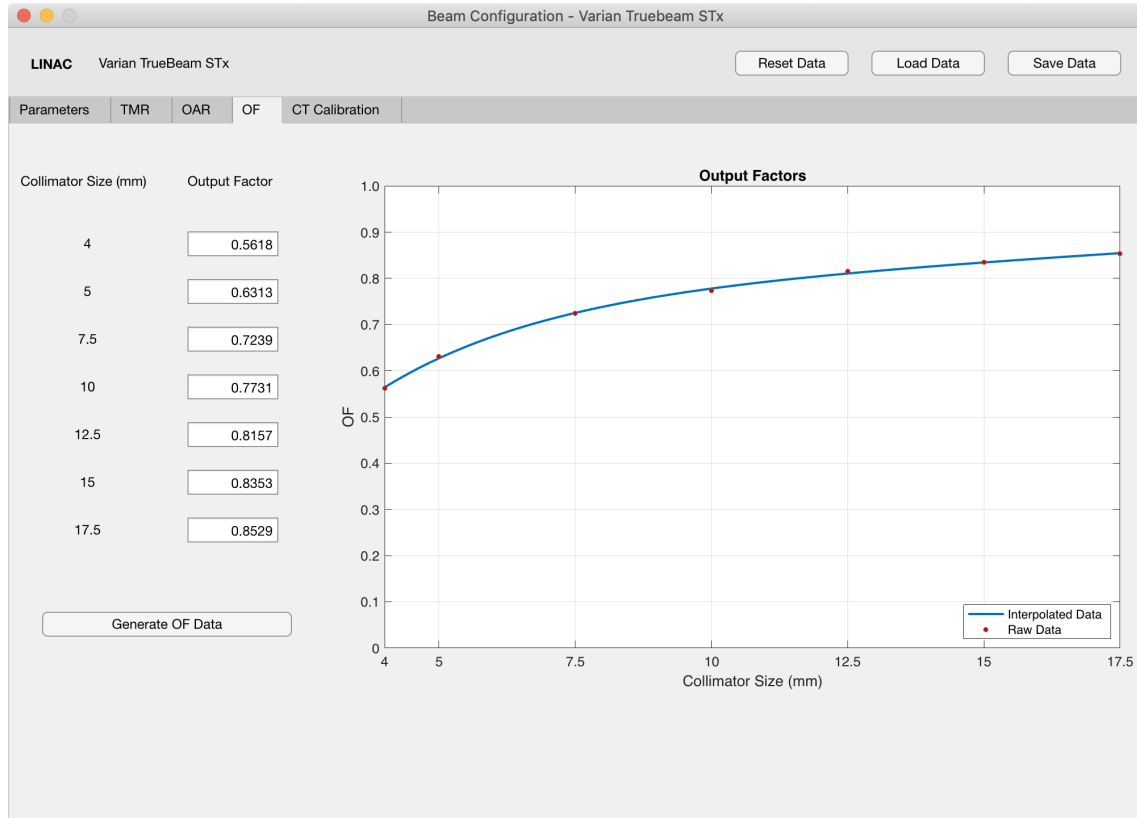
Figure 26: Beam Configuration application - OF tab overview.

Model applied:

$$OF(S) = a \cdot e^{b \cdot S} + c \cdot e^{d \cdot S} \tag{6.18}$$

S is the field size and a, b, c and d are the parameters to be fitted.

6.2.4.5 CT calibration

CT calibration tab allows introducing CT calibration curve data. A set of different Hounsfield units and the corresponding relative electron density are required. There is no need to introduce the mass density calibration curve.

RED is stored as a function of HU. To create a curve, data is interpolated linearly.
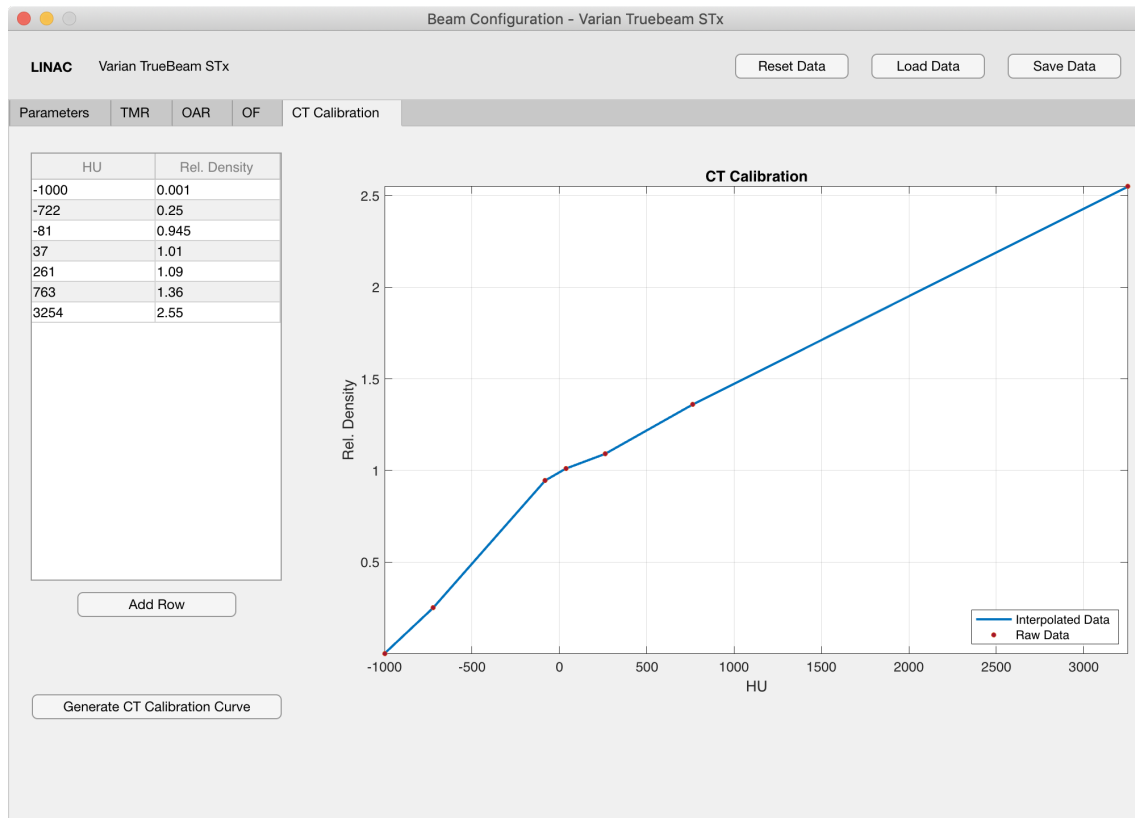
Figure 27: Beam Configuration application - CT Calibration tab overview.

6.2.4.6 Data management

"Beam Configuration" application for TrueBeam™ STx and Novalis Tx™ stores all the values introduced and imported by the user and also stores the generated curves for TMR, OAR, OF and CT calibration curve with proper interpolation in a single MAT-File with .mat extension. A MAT-File should be created for each LINAC and energy configured. If multiple CT scanners are used with different calibration curves, this procedure should be repeated for each CT scan. It is possible to load a saved file, edit values and save it again.

MAT-Files are used in the "Stereotactic MU Calculator" application. Each MAT-File contains all the required beam data such as absolute dose calibration parameters and relative measurements (TMR, OAR, OF) that are necessary to calculate the dose in a

phantom or patient. Explanation of how the "Stereotactic MU Calculator" works will be given in the next chapters.

6.2.5 Stereotactic MU Calculator application

"Stereotactic MU Calculator" is the main application of this project. It is a GUI that allows importing DICOM data from phantoms or patients. It uses beam data previously processed in "Beam Configuration" application in order to verify the number of MU of each treatment field. It supports exported plans from Eclipse™ workspace planned for TrueBeam™ STx (6 FFF and 10 FFF) and Novalis Tx™ (6X SRS) using stereotactic cones.
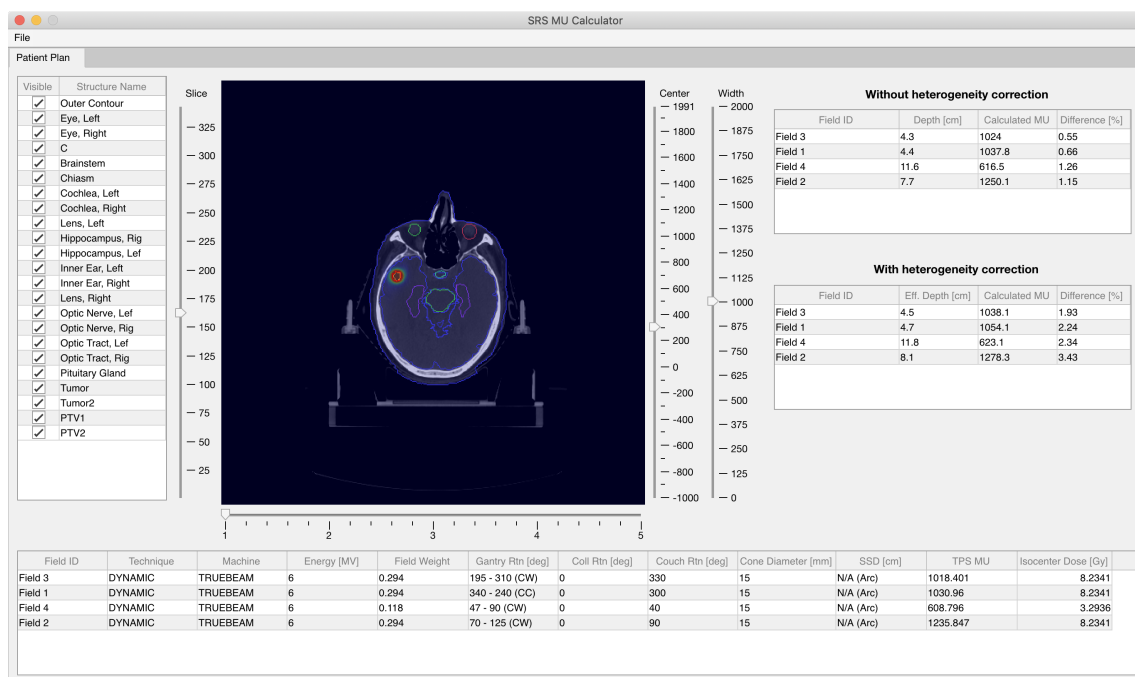
Figure 28: Stereotactic MU Calculator application overview.

A folder should be created for each treatment plan with all DICOM data. Sub-folders can be created to organize files. The application will recursively read all files with .dcm extension inside the folder selected by the user. Multiple DICOM data from different plans cannot be mixed in the same folder because only a single plan can be loaded at the same time.

The following files are required:

- CT images
- DICOM RT Structure Set
- DICOM RT Plan
- DICOM RT Dose

The imported plan must be previously approved in Eclipse™ workspace with a "Planning Approved" or "Treatment Approved" status. It must be prescribed and calculated with a 3D dose volume. A valid collimator must be assigned to every treatment field (setup-fields are discarded). Only plans with static fields or arc fields are supported. These verifications are performed automatically by the application while importing and processing the DICOM data files.

DICOM files are filtered depending on its Modality attribute on the file metadata. The application will import the following DICOM objects:

Table 15: DICOM objects supported.

DICOM object	Modality attribute	SOP UID
CT images	CT	1.2.840.10008.5.1.4.1.1.2
RT Structure Set	RTSTRUCT	1.2.840.10008.5.1.4.1.1.481.3
RT Plan	RTPLAN	1.2.840.10008.5.1.4.1.1.481.5
RT Dose	RTDOSE	1.2.840.10008.5.1.4.1.1.481.2

6.2.5.1 DICOM Coordinates System

Before going on to the CT images and DICOM RT objects imported it should be defined what is the DICOM Coordinates System.

DICOM Reference Coordinates System (RCS) or DICOM patient-based coordinate system defines the location of the image with respect to the body of the patient. It is based on X, Y and Z axis. X axis is the sagittal plane and separates the left from the right; Y axis is the coronal plane, perpendicular to the ground and separates the front (anterior) from the back (posterior); Z axis is the axial plane, parallel to the ground and separates the head (superior) from the feet (inferior).
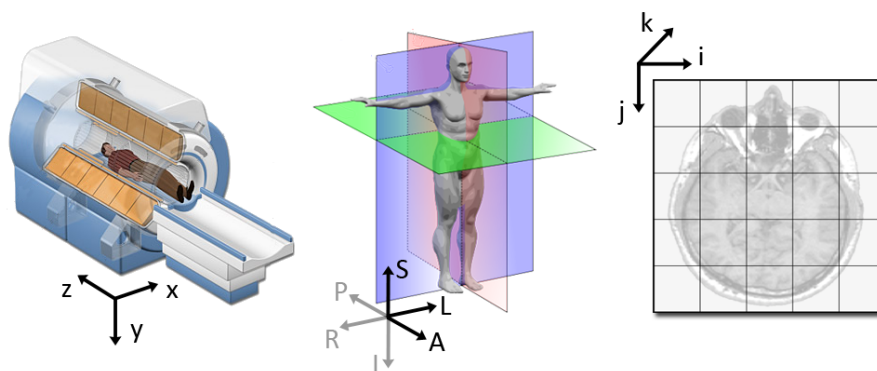
Figure 29: Coordinates systems in a MRI scanner. The same is valid for a CT scanner. Image downloaded from https://www.slicer.org/wiki/Coordinate_systems.

The origin is the intersection of all three mutually perpendicular axes. The origin is defined

in the CT scanner and is stored in the Image Position (Patient) attribute. It contains the x, y and z coordinates of the upper left corner (center of the first voxel transmitted) of the image, in mm [45].

LPS (left, posterior, superior) is the default DICOM orientation:

$$LPS = \left\{ \begin{array}{ll} \text{X axis} & \text{from right of the patient towards left} \\ \text{Y axis} & \text{from anterior of the patient towards posterior} \\ \text{Z axis} & \text{from inferior of the patient towards superior} \end{array} \right\}$$

DICOM 2D images are stored row by row, from the left to the right, followed by the second row from top to bottom. The position of an image in 3D space is indicated in a coordinate system using orientation and position 3D vectors. Orientation vectors indicate how much an image is rotated with respect to its coordinate system, and the position vector indicates the location of the image with respect to the origin. Orientation vectors are given by the Image Orientation (Patient) attribute. It contains two triplets, the first triplet values (direction cosines) represent the vector for the image orientation of the X-axis, and the second triplet values indicate the vector for the image orientation of the Y-axis [45].
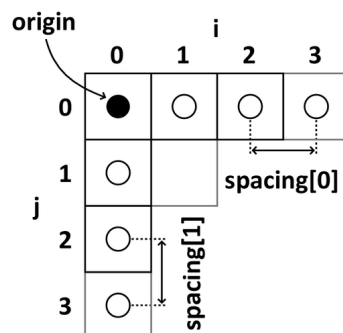
Figure 30: Image coordinate system of a 2D image. Image downloaded from https://www.slicer.org/wiki/Coordinate_systems.

A Head First Supine (HFS) scan position is a simple case where the patient-based coordinate system is aligned with the imaging system. As we move along the image columns (from left to right of the image), we are also moving on the positive direction on the X axis of the patient (from the right hand of the patient to the left hand). The same applies for the Y axis. As we move along the image rows (from top to bottom of the image), we are also moving on the positive direction on the Y axis of the patient (from the anterior side of the patient to the posterior).

Only HFS scans are supported by the application because this position is the used for patients undergoing radiosurgery. Conversion of a voxel P with coordinates $P_{x,y,z}$ in the patient-based coordinate system to the image coordinate system is simplified and can be

performed using the equation:

$$P_{c,r,s} = \frac{P_{x,y,z} - O_{x,y,z}}{V_{x,y,z}} \tag{6.19}$$

Where $P_{c,r,s}$ is the triplet with the column, row and slice indexes in the image coordinate system, $P_{x,y,z}$ is the triplet with the x, y and z position in the patient-based coordinate system (in mm), $O_{x,y,z}$ is the CT origin triplet (in mm) and $V_{x,y,z}$ is the voxel size triplet in x, y and z directions in the patient based coordinate system (in mm). This equation assumes that the first index of an array starts at 0 position, however, arrays in MATLAB® starts at position 1, so equation (6.19) becomes:

$$P_{c,r,s} = \frac{P_{x,y,z} - O_{x,y,z}}{V_{x,y,z}} + (1, 1, 1) \tag{6.20}$$

Row and column are purposely flipped in $P_{c,r,s}$ triplet because X direction corresponds to the image columns and Y direction corresponds to the image rows. After the flip, $P_{c,r,s}$ becomes $P_{r,c,s}$.

6.2.5.2   DICOM data files import and processing

CT images

The following DICOM attributes are read:

- **Instance Number:** Image identification number.

- **Image Position (Patient):** The X, Y, and Z coordinates of the upper left hand corner (center of the first voxel transmitted) of the image, in mm.

- **Image Orientation (Patient):** The direction cosines of the first row and the first column with respect to the patient.

- **Patient Position:** Patient position relative to the imaging equipment space.

- **Pixel Spacing:** Physical distance in the patient between the center of each pixel, specified by a numeric pair (adjacent row spacing and adjacent column) spacing in mm.

- **Window Center:** Acquisition Window Center value.

- **Window Width:** Acquisition Window Width value.

- **Rescale Slope / Rescale Intercept:** Constants that specify the linear transformation from pixels stored on disk to an output unit. In CT images, it maps

the pixel values to HU.

$$U = m \times SV + b \tag{6.21}$$

Where U is the output unit, m is the Rescale Slope, SV is the stored value in the pixel of the CT image and b is the Rescale Intercept. In CT images, the output is the HU value.

DICOM metadata gives the Pixel Spacing attribute, however, there is no attribute for Slice Spacing and it needs to be computed based on the Image Position (Patient) of two consecutive CT slices:

$$\text{Slice Spacing} = |Z_2 - Z_1| \tag{6.22}$$

Where Z_2 is the longitudinal distance, in mm, from the CT origin to the second acquired image and Z_1 is the longitudinal distance, in mm, from the CT origin to the first acquired image. Z_2 and Z_1 are the third value of Image Position (Patient) triplet for both CT slices.

CT images are saved in a 3D array (from now on, a multi-dimensional array will be called matrix). The first two dimensions are the rows and columns (i, j) of the CT image; the third dimension are the CT slices (k).

RT Structure Set

Data from structures are stored in various sub-fields inside the RTSTRUCT file metadata. The following sub-fields are read for each structure:

- Structure Set ROI Sequence
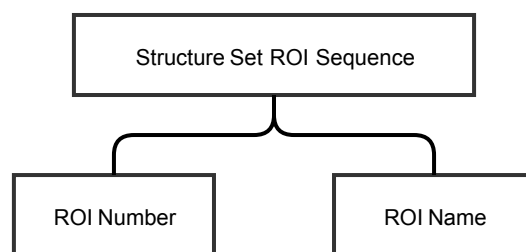
Figure 31: Data extracted from Structure Set ROI Sequence.

Structure Set ROI Sequence stores basic information about every structure: ROI Number is a integer assigned to the structure that allows it to be referenced internally in the multiple metadata sub-fields; ROI Name is the name of the structure.

• ROI Contour Sequence
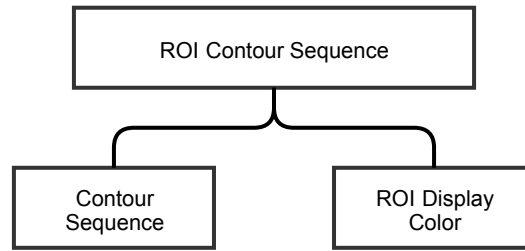
Figure 32: Data extracted from ROI Contour Sequence.

ROI Contour Sequence contains the slice contours of each structure, only present if the structure contain at least one planar contour. If it does not contain at least one planar contour it means that the structure is empty and therefore, it is not processed. This sequence also contains the display colour (red, green and blue (RGB) triplet) of the structures.

Contour Sequence attribute contains the contours of every slice contoured of every structure.
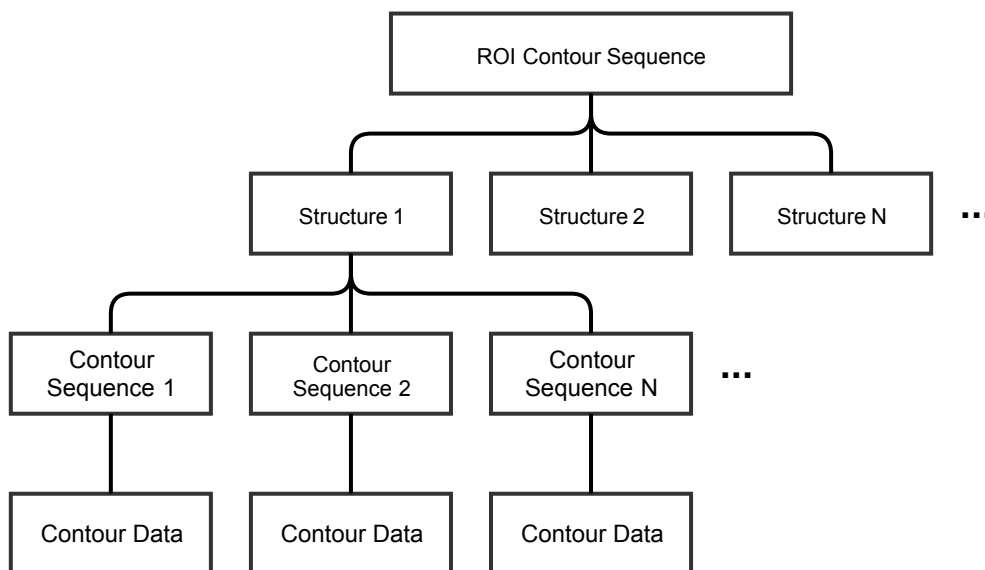
Figure 33: Contour Data extracted from ROI Contour Sequence.

Contours are saved as points under Contour Data attribute. Each point is saved as a triplet with its x, y and z coordinates in relation to the CT origin. A contour is only valid if its geometric type is CLOSED_PLANAR. This can be verified reading the Contour Geometric Type of every Contour Sequence created.

The application reads all the contour points stored under each Contour Data attribute and creates a polygon.

Figure 34: Patient external contour with its contour points on the left and the polygon on the right.

The polygon is useful to determine which voxels belong to the contoured structure. Pixels inside the polygon are inside the contoured structure and they have a value of 1. Every other pixels have a value of 0. This will create a binary image (with the same rows and columns of the CT scan) for every Contour Sequence.

In the end, binary images of all Contour Sequence instances are merged in a 3D matrix with the same dimensions of the CT scan. This is repeated for each structure so each one will have a matrix in which each voxel that belongs to the contour has a value of 1.
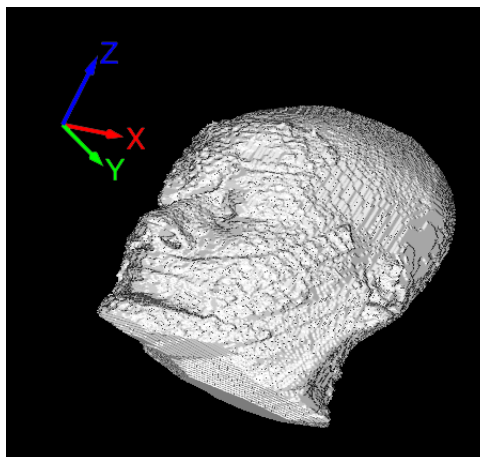
Figure 35: Patient 3D reconstruction of its external contour.

- ROI Observations Sequence

Density overrides defined in the TPS are stored under the ROI Observations Sequence attribute. If a structure has an HU value assigned, its corresponding RED is read from ROI Physical Property Value attribute:
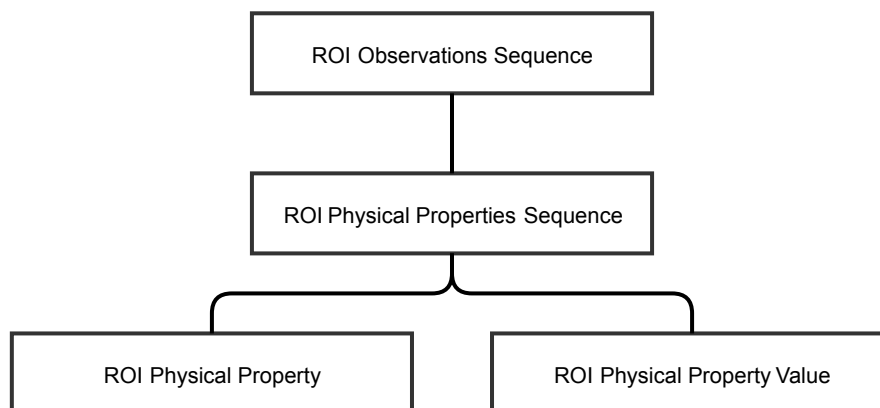
Figure 36: Data extracted from ROI Observations Sequence.

Since ROI Physical Property attribute can assume multiple physical properties (such as relative electron density or relative mass density), this attribute should be equal to REL_ELEC_DENSITY in order to read ROI Physical Property Value properly as a RED value.

RT Plan

RTPLAN file metadata contains data of all setup/treatment fields, reference points and the LINAC tolerance table used, in multiple sub-fields. Only data from treatment fields is read from the file metadata under the Beam Sequence and Fraction Group Sequence attributes.

- Beam Sequence

The Beam Sequence attribute contains all beam parameters. Beam Number is a integer assigned to the beam that allows it to be referenced internally in the multiple metadata sub-fields; Beam Name is the name of the field; Beam Type determines if the field is static or in arc. Source-Axis Distance is also read just to verify if it matches the SAD loaded from the "Beam Configuration" MAT-File. Applicator Sequence stores the nominal cone diameter used in the beam.

The Control Point Sequence attribute contains all control points of the beam since the start of the irradiation until the end. Control points are snapshots of the system at a discrete time. They play an important role in IMRT and volumetric arc therapy (VMAT) treatments where MLC leaves and dose rate changes during the irradiation. A control point is created every time a beam parameter changes such as gantry rotation, MLC leaves position or dose rate. Hundreds of control points per field might be created for these techniques.
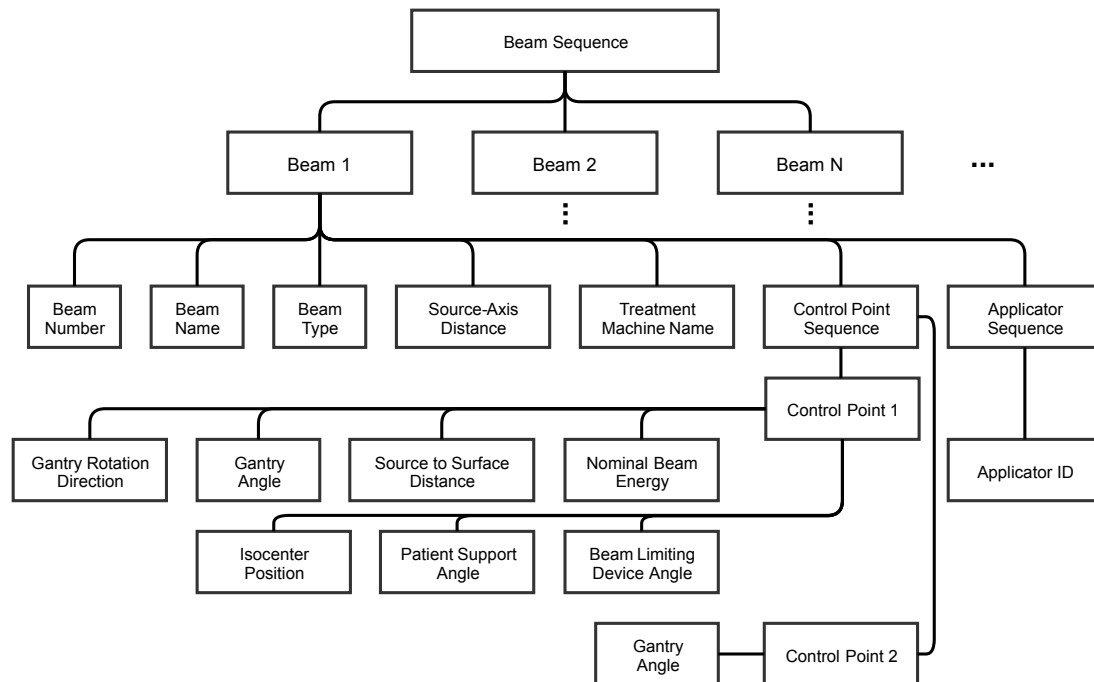
Figure 37: Data extracted from Beam Sequence.

A static field only has one control point because beam parameters do not change during irradiation. An arc field with stereotactic cones has two control points: the initial control point where all beam parameters are defined and a second control point indicating the final gantry angle. No more control points are created because there are no beam parameters changing during the irradiation.
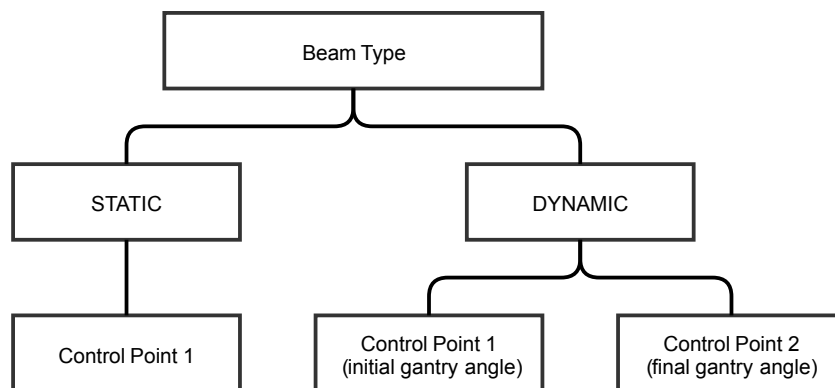
Figure 38: Control Points extracted from Beam Sequence.

The following attributes are extracted from the first control point:

- **Gantry Rotation Direction:** The direction of gantry rotation. Only used if the field is an arc. It can be clockwise or counter-clockwise.

- **Gantry Angle:** Gantry angle with respect to the IEC FIXED REFERENCE coordinate system. For arc fields, it is the initial gantry angle.

- **Patient Support Angle:** Couch rotation with respect to the IEC FIXED REFERENCE.

- **Beam Limiting Device Angle:** Collimator rotation with respect to the with respect to the IEC FIXED REFERENCE.

- **Nominal Beam Energy:** Energy of the beam.

- **Isocenter Position:** Isocenter position in relation to the CT origin.

- **Source to Surface Distance:** SSD of the beam. For arc fields, it is the SSD of the initial gantry angle.

The second control point is used only to extract the final gantry angle.

- Fraction Group Sequence

The Fraction Group Sequence contains the dose that each field contributes to a specific point and the MU per field, for one treatment fraction, under the Referenced Beam Sequence sub-field in the Beam Meterset attribute. It also contains the number of planned fractions in the Number of Fractions Planned attribute.
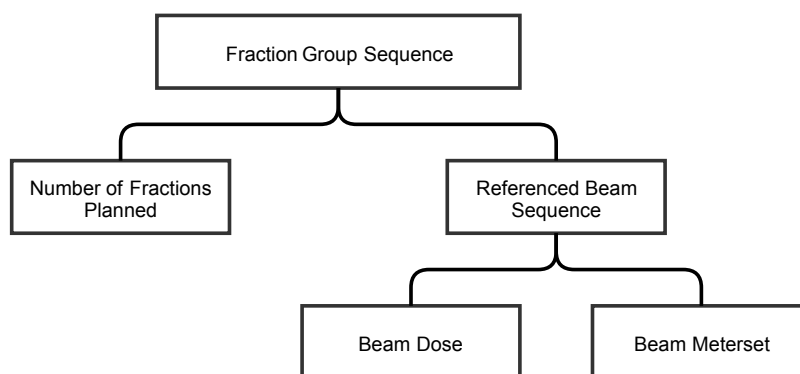
Figure 39: Data extracted from Fraction Group Sequence.

The dose at a specific point is given by the Beam Dose attribute. The point coordinates in relation to the CT origin is given by the Beam Dose Specification Point attribute, however, if the user does not create this point manually during the planning, it is omitted from the DICOM RTPLAN metadata. If the Beam Dose Specification Point is omitted from the DICOM metadata, Beam Dose can't be used to determine the dose that each field contributes to the isocenter. However, Beam Dose can be used to calculate the weight of each field.

Relative weight W_i of beam i is given by:

$$W_i = \frac{BD_i}{BD_{total}} \tag{6.23}$$

Where BD_i is the Beam Dose attribute value for beam i and BD_{total} is the sum of all Beam Dose attribute values of all treatment fields.

The dose at the isocenter of each field (per fraction) is then calculated using the dose of the isocenter nearest voxel, extracted from RT Dose metadata file.

$$ID_i = \frac{ID_{total}}{\text{fractions}} \times W_i \tag{6.24}$$

Where ID_i is the dose at the isocenter of field i (per fraction), ID_{total} is the dose of the isocenter nearest voxel, divided by the number of fractions and W_i is the relative field weight calculated on equation (6.23).

The total dose at the isocenter is obtained in the 3D calculation volume, as will be explained next.

RT Dose
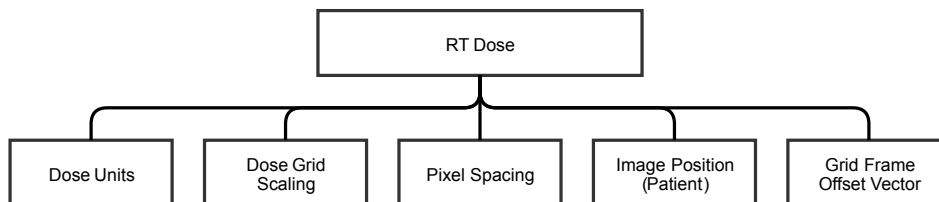
Figure 40: Data extracted from RT Dose.

RTDOSE file metadata contains the 3D calculation volume and the dose volume histogram (which is not used). The 3D calculation volume comes in a matrix with arbitrary values. To convert the matrix elements to absolute dose in Gray, RT Dose file must be exported from the TPS as absolute dose and not relative dose. This verification is done with the Dose Units attribute value. It should be equal to GY and not RELATIVE. Every matrix element is then multiplied by the Dose Grid Scaling attribute value.

In order to match the 3D dose calculation volume with the CT scan, they must have the same voxel size and dimensions (same number of rows, columns and slices).

The calculation resolution is chosen during the treatment planning and usually it is isotropic (same value for pixel and slice spacing). Pixel spacing is read from Pixel Spacing attribute and slice spacing is derived from the $\text{Grid Frame Offset Vector}$, which

contains a given slice offset from the first slice in millimeters. If the voxel size of the dose matrix does not match the CT, dose matrix is resampled with linear interpolation.

The last step is the dose matrix registration with the CT scan. By having the coordinates of the first voxel transmitted (upper left corner of the first dose slice) from $\mathrm{Image\ Position}$ $(\mathrm{Patient})$ attribute in RT Dose metadata, registration can be done. This is needed because normally the dose matrix has smaller dimensions than the CT scan. The calculation box area is defined during the treatment planning and is placed around the outer contour of the patient or phantom.
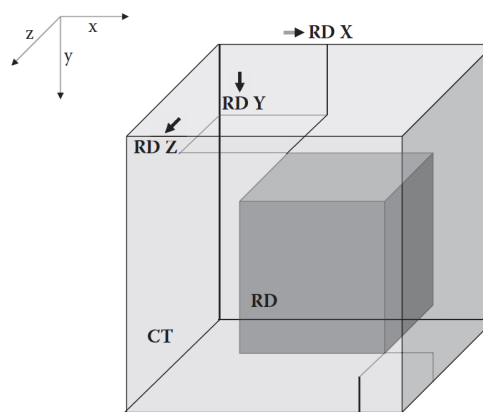
Figure 41: CT and dose matrices before the registration. RD X, RD Y and RD Z are the coordinates of the upper left corner of the first dose slice. Image adapted from *Clinical Radiotherapy Physics with MATLAB*® (Pavel Dvorak, 2018).

After the registration, the new dose matrix created matches the dimensions of the CT scan (same number of rows, columns and slices). Every voxel that is outside the old dose matrix is assigned with no dose (0 Gy).

Plans calculated in CDC workspace and exported from Eclipse™ might have a 3D dose calculation volume outside the CT scan. This happens because CDC automatically adjusts the dose calculation volume area, however, it may adjust beyond the CT area for an unknown reason. In this case, dose voxels beyond the CT scan are discarded.

6.2.5.3 MU calculation without heterogeneity correction

With all beam configuration data and patient DICOM data imported, the required MU of each field per treatment fraction can be calculated.

MU calculation is based on equation (5.1) from CDC algorithm:

$$D(r, d, SSD, S) = MU \times DR_{ref} \times OF_{TMR_{max}}(S) \times TMR(d, S) \times \left(\frac{SAD}{SSD + d} \right) \times OAR(r, S)$$

(6.25)

73

To calculate MU instead of dose:

$$MU = \frac{D(r,d,SSD,S)}{DR_{ref} \times OF_{TMR_{max}}(S) \times TMR(d,S) \times \left(\frac{SAD}{SSD+d}\right) \times OAR(r,S)} \tag{6.26}$$

Since MU calculations are performed at the isocenter, there is no lateral shift and there is no need to apply a inverse square law correction:

$$OAR(r,S) = 1$$

And:

$$\left(\frac{SAD}{SSD+d}\right) = 1$$

Equation (6.26) is then reduced to:

$$MU = \frac{D(r,d,SSD,S)}{DR_{ref} \times OF_{TMR_{max}}(S) \times TMR(d,S)} \tag{6.27}$$

The reference dose rate, DR_{ref}, is:

$$DR_{ref} = \left(\frac{D_{ref}}{MU_{ref}}\right) \tag{6.28}$$

And $OF_{TMR_{max}}(S)$ is the output factor corrected for the depth of maximum dose:

$$OF_{TMR_{max}}(S) = OF(S) \times \frac{PDD(S,SSD,d_{max})}{PDD(S,SSD,d)} \times \left(\frac{SSD+d_{max}}{SAD}\right)^2 \tag{6.29}$$

Equation (6.27) can be rewritten as:

$$MU = \frac{D(r,d,SSD,S)}{\left(\frac{D_{ref}}{MU_{ref}}\right) \times OF(S) \times \frac{PDD(S,SSD,d_{max})}{PDD(S,SSD,d)} \times \left(\frac{SSD+d_{max}}{SAD}\right)^2 \times TMR(d,S)} \tag{6.30}$$

The dose at the isocenter is given by $D(r,d,SSD,S)$. For a single treatment fraction this value is given by equation (6.24) discussed in the RT Plan section. The reference dose-rate, $\left(\frac{D_{ref}}{MU_{ref}}\right)$, is stored in the beam data configuration and only depends on the LINAC and energy of the beam.

OF depends on the collimator size used and is read directly from the beam configuration data. The OF correction for the depth of maximum dose is the OF multiplied by the quotient between the PDD at d_{max} and the PDD at the depth of which OF were taken,

multiplied by the inverse square law correction factor:

$$OF_{TMR_{max}}(S) = OF(S) \times \frac{PDD(S, SSD, d_{max})}{PDD(S, SSD, d)} \times \left(\frac{SSD + d_{max}}{SAD} \right)^2 \qquad (6.31)$$

PDD at d_{max} is assumed to be 100 so the quotient between both PDDs becomes:

$$\frac{100}{PDD(S, SSD, d)}$$

Where S is the nominal collimator diameter, SSD and d are the SSD and depth taken in OF measurements, respectively. PDD calculation is derived from TMR using a equation proposed by L J van Battum et al. [46].

$$TMR(d, r_d) = \frac{D_{inf}(d, r_d)}{S_{c,p}(r_s^*)} = \frac{PDD(d, r_s, f) \times S_{c,p}(r_s) \times \left(\frac{f+d}{f+t_0} \right)^2}{S_{c,p}(r_s^*)} \qquad (6.32)$$

Where,

- d = depth;
- r_d = field size defined at depth d;
- $TMR(d, r_d)$ = TMR value at depth d;
- $D_{inf}(d, r_d)$ = depth dose curve that represents a curve corrected for source-detector distance (infinite focus);
- f = source-phantom distance;
- $r_s^* = r_d \times \left(\frac{f+d-t_0}{f+d} \right)$;
- $S_{c,p}(r_s^*)$ = output factor at field size r_s^*;
- $r_s = r_d \times \left(\frac{f}{f+d} \right)$, field size defined at the surface of the phantom;
- $PDD(d, r_s, f)$ = PDD value at depth d and field size r_s defined at the surface of the phantom;
- $S_{c,p}(r_s)$ = output factor at field size r_s defined at the surface of the phantom;
- t_o = depth of maximum dose.

PDD at depth d and field size r_s defined at surface is given by:

$$PDD(d, r_s, f) = TMR(d, r_d) \times \left(\frac{S_{c,p}(r_s^*)}{S_{c,p}(r_s)} \right) \times \left(\frac{f + t_0}{f + d} \right)^2 \qquad (6.33)$$

$S_{c,p}(r_s^*)$ for an arbitrary field size can be calculated using the OF two-term exponential curve fit as defined in equation (6.18).

$TMR(d, S)$ is the remaining term in equation (6.30) that needs to be determined and is the only one that depends on the depth. All the others are constants (such as DR_{ref}) or are directly dependent on the reference conditions and cone size used (such as $OF_{TMR_{max}}(S)$).

TMR calculation has a different approach depending if the beam is static or arc. The calculation is simplified if the beam is static: only depth needs to be calculated in order to obtain the TMR value from the beam data. For arc beams, the average TMR is calculated instead. The arc is segmented in multiple incident gantry angles (with 1º resolution between each incident gantry angle) and for each gantry angle, depth is calculated to obtain the TMR value. In the end, the average TMR is used in equation (6.30).
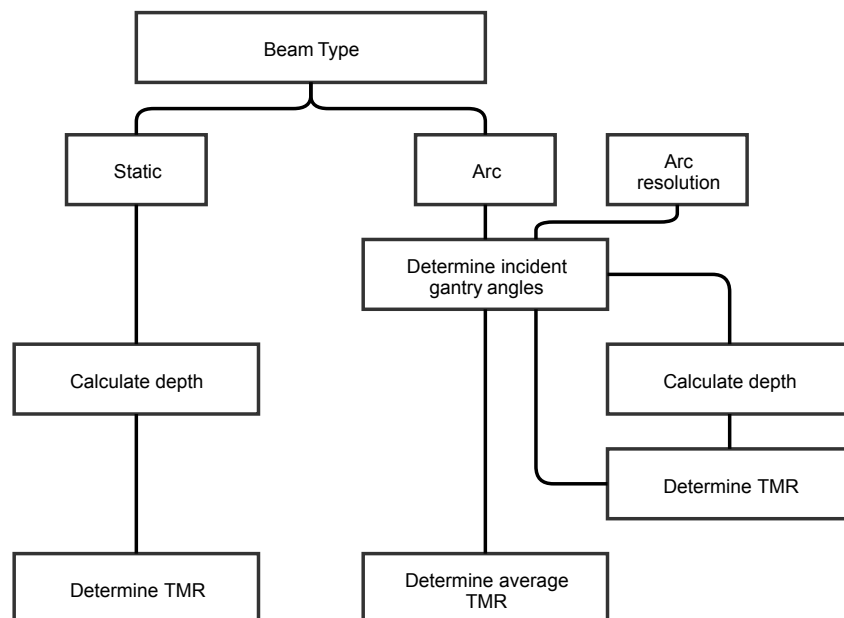
Figure 42: TMR calculation of static or arc treatment fields.

An arc resolution of 1º was chosen because it improves the accuracy of the average TMR calculation in arc fields. Irregular surfaces such as the nose and the ears of patients may benefit from shorter arc resolutions. A comparison between 1º and 10º arc resolution in TMR calculation is shown of figure 43. This value can be changed in CDC algorithm between 1º and 10º, however, in this application the value is fixed and cannot be changed.
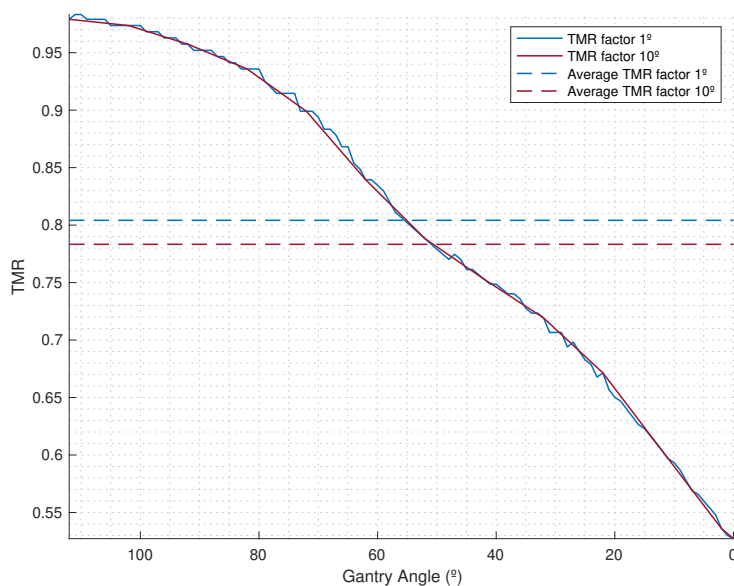
Figure 43: TMR factor in function of gantry angle with 1º and 10º arc resolution. Average TMR factor for both resolutions is displayed in dashed lines. Data is from a non-coplanar arc of a patient plan.

Depth calculation is based on the CT scan and on the external contour. A structure representing the external contour with $\mathrm{ROI\ Interpreted\ Type}$ equal to $\mathrm{EXTERNAL}$ must exist in the RT Structure Set file.

For static fields the depth can be calculated using the $\mathrm{Source\ to\ Surface\ Distance}$ attribute value:

$$Depth = SAD - SSD \qquad (6.34)$$

However, equation (6.34) is not used and depth is calculated from scratch, for both static and arc fields.

Depth is the distance between the beam entry point on the surface of the patient/phantom and the isocenter location, along the CAX. For a given CT scan and RT Structure Set with the external contour, the depth depends on the gantry angle and couch rotation.

The following steps are executed to calculate the depth in metric units:

1. Obtain the CT origin in the image coordinate system:

$$\mathrm{CTorigin}_{c,r,s} = \frac{-\mathrm{CTorigin}_{x,y,z}}{V_{x,y,z}} + (1,1,1) \qquad (6.35)$$

Where $\mathrm{CTorigin}_{c,r,s}$ is the CT origin in the image coordinate system, $\mathrm{CTorigin}_{x,y,z}$ are the coordinates of the upper left corner of the first transmitted image (Image $\mathrm{Position\ (Patient)}$ attribute value from CT scan). $V_{x,y,z}$ is the voxel size in x, y and z directions. Rows and columns are flipped because X direction corresponds to

the matrix columns and Y direction corresponds to the matrix rows. After the flip, $\mathrm{CTorigin}_{c,r,s}$ becomes $\mathrm{CTorigin}_{r,c,s}$.

2. Obtain the isocenter displacement from the CT origin in the image coordinate system:

$$\mathrm{IsocenterOffset}_{c,r,s} = \frac{\mathrm{IsocenterOffset}_{x,y,z}}{V_{x,y,z}} \tag{6.36}$$

Where $\mathrm{IsocenterOffset}_{c,r,s}$ is the offset from the CT origin in the image coordinate system, $\mathrm{IsocenterOffset}_{x,y,z}$ is the Isocenter Position attribute value and $V_{x,y,z}$ is the voxel size in x, y and z directions. Rows and columns are flipped for the same reason above. After the flip, $\mathrm{IsocenterOffset}_{c,r,s}$ becomes $\mathrm{IsocenterOffset}_{r,c,s}$.

3. Get the isocenter position related to the upper left corner voxel of the first transmitted image:

$$\mathrm{Isocenter}_{r,c,s} = \mathrm{CTorigin}_{c,r,s} + \mathrm{IsocenterOffset}_{r,c,s} \tag{6.37}$$

4. Find the target (X-Ray source) position offset from the isocenter in metric units:

$$\mathrm{TargetOffset}_{x,y,z} = \left\{ \begin{array}{l} x = \mathrm{SAD} \times \cos(\mathrm{CouchRTN}) \times sin(\mathrm{GantryRTN}) \\ y = -\mathrm{SAD} \times \cos(\mathrm{GantryRTN}) \\ z = -\mathrm{SAD} \times \sin(\mathrm{CouchRTN}) \times sin(\mathrm{GantryRTN}) \end{array} \right\}$$

Where SAD is the source-axis distance, $\mathrm{CouchRTN}$ is the couch angle and $\mathrm{GantryRTN}$ is the gantry angle, both with respect to the IEC FIXED REFERENCE coordinate system.

5. Get the target position offset from the isocenter in the image coordinate system:

$$\mathrm{TargetOffset}_{c,r,s} = \frac{\mathrm{TargetOffset}_{x,y,z}}{V_{x,y,z}} \tag{6.38}$$

Where $V_{x,y,z}$ is the voxel size in x, y and z directions. Rows and columns are flipped for the same reason above. After the flip, $\mathrm{TargetOffset}_{c,r,s}$ becomes $\mathrm{TargetOffset}_{r,c,s}$.

6. Get the increment between the isocenter and the target, dividing $\mathrm{TargetOffset}_{r,c,s}$ by its Euclidean norm:

$$\mathrm{Increment}_{r,c,s} = \frac{\mathrm{TargetOffset}_{r,c,s}}{\sqrt{|\mathrm{TargetOffset}_r|^2 + |\mathrm{TargetOffset}_c|^2 + |\mathrm{TargetOffset}_s|^2}} \tag{6.39}$$

$\mathrm{Increment}_{r,c,s}$ is a triplet with the increment values in rows, columns, slices.

7. Loop from the starting point (the isocenter location) to the target position with the increment values defined above. For each new position, the algorithm verifies if the current voxel is inside the external contour of the patient or phantom. This verification is done using the binary matrix created during the RT Structure Set processing. A value of 1 means that the current voxel is inside the external contour.

In this case, the algorithm continues to the next voxel. A value of 0 means that the current voxel no long belongs to the external contour. The last voxel that belongs to the external contour is saved as the beam entry point on the patient/phantom (BEP_{rcs}). The loop stops when the limits of the CT matrix are reached.

8. Get the offset coordinates between the isocenter and the beam entry point on the patient/phantom:

$$\text{BEPOffset}_{r,c,s} = \text{BEP}_{r,c,s} - \text{Isocenter}_{r,c,s} \tag{6.40}$$

9. Convert the previous offset coordinates to metric units:

$$\text{BEPOffset}_{y,x,z} = \frac{\text{BEPOffset}_{r,c,s}}{V_{y,x,z}} \tag{6.41}$$

$\text{BEPOffset}_{y,x,z}$ is a triplet with the distance in y, x and z directions from the isocenter to the beam entry point on the patient/phantom and $V_{y,x,z}$ is the voxel size in y, x and z directions. After the flip, $\text{BEPOffset}_{y,x,z}$ becomes $\text{BEPOffset}_{x,y,z}$.

10. Finally, depth in metric units (mm) is given by:

$$\text{Depth} = \sqrt{|\text{BEPOffset}_x|^2 + |\text{BEPOffset}_y|^2 + |\text{BEPOffset}_z|^2} \tag{6.42}$$

Depth is then used to determinate the TMR value for static fields or the average TMR value for arc fields using the beam data of the LINAC and energy imported.

With all terms of equation (6.30) determined, MU of all treatment fields per treatment fraction without heterogeneity correction can be calculated and compared to the MU calculated by CDC algorithm. The difference is given by:

$$\text{Difference (\%)} = \frac{\text{MU}_{NHC} - \text{MU}_{CDC}}{\text{MU}_{CDC}} \times 100 \tag{6.43}$$

Where MU_{NHC} is the number of MU calculated by the application without heterogeneity correction and MU_{CDC} is the number of MU calculated by CDC algorithm.

6.2.5.4 MU calculation with heterogeneity correction

MU calculation with heterogeneity correction shares the same equation used before in MU calculation without heterogeneity correction. The only exception is the depth which is replaced by the effective depth, d_{eff}, in TMR calculation:

$$MU = \frac{D(r, d, SSD, S)}{DR_{ref} \times OF_{TMR_{max}}(S) \times TMR(d_{eff}, S)} \tag{6.44}$$

Effective depth or equivalent path length (EPL) is the distance in tissue weighted by the relative electron density of that tissue to water. It is a method to correct heterogeneities inside the patient body such as bones or air cavities, however, this basic 1D inhomogeneity correction only works well for points that are far away from inhomogeneities. It does not represent the dose within the inhomogeneity because it does not consider the modifications of the scatter component, which has a greater influence within or close the inhomogeneity [22].

EPL in the algorithm created in this work is defined as:

$$\text{EPL} = d_{eff} = \sum_i \rho_i^{el} \times x_i \tag{6.45}$$

Where i represents each CT voxel along a given rayline between the isocenter and the target, ρ_i^{el} is the relative electron density of voxel i and x_i is the voxel dimension along a given rayline.
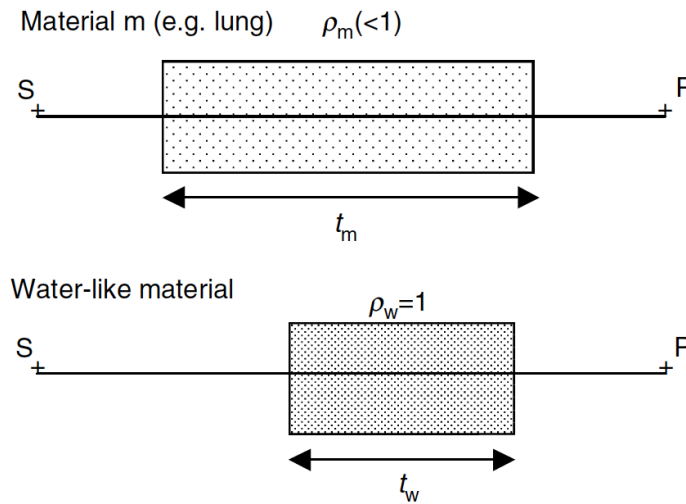
Figure 44: EPL method illustration. The attenuation at point P for a thickness t_m of material with density ρ_m is the same as for a scaled thickess t_w of water where $t_w = t_m \times \rho_m$. Image adapted from *Handbook of Radiotherapy Physics*, (Phylip Mailes, et al., 2007).

EPL calculation along a given ray line uses the first 6 steps of depth calculation discussed in the previous section. From this step forward, a loop is made from the starting point (the isocenter location) to the target position with the increment values defined in equation (6.39). For each loop interaction, the algorithm calculates the RED value of the voxel and then multiplies it by the increment distance.

First, the increment between each loop interaction is calculated in metric units:

$$\text{Increment}_{y,x,z} = \frac{\text{Increment}_{r,c,s}}{V_{y,x,z}} \tag{6.46}$$

$\text{Increment}_{r,c,s}$ was defined in equation (6.39). $\text{V}_{y,x,z}$ is the voxel size in y, x and z directions. After the rows/columns flip, $\text{Increment}_{y,x,z}$ becomes $\text{Increment}_{x,y,z}$.

The increment distance in metric units between each loop interaction is then calculated:

$$\text{IncrementDistance} = \sqrt{|\text{Increment}_x|^2 + |\text{Increment}_y|^2 + |\text{Increment}_z|^2} \qquad (6.47)$$

EPL between each loop interaction is given by:

$$\text{EPL}_i = \rho_i^{el} \times x_i \qquad (6.48)$$

Where i represents each CT voxel along the ray line, EPL_i is the EPL of voxel i, ρ_i^{el} is the RED value of voxel i and x_i is IncrementDistance between each loop interaction, defined in equation (6.47).

When the loop reaches the patient or phantom external contour, it finishes the EPL count. At this point, EPL is the sum of all contributions of EPL_i along the ray line and is given in metric units (mm). However, the loop continues until it reaches the CT matrix limits because it may exist contoured structures with custom density assigned outside the patient or phantom external contour, such as the LINAC couch or the patient mask support. This type of structures will increase the EPL, even if they are outside the external contour. Structures outside the external contour that attenuate radiation considerably should be contoured and assigned with the respective material density. If they are contoured but without any custom density assigned, the algorithm will not count them to the EPL calculation.

RED calculation depends on the voxel HU and CT calibration curve. If the voxel belongs to a structure with custom density assigned, the RED value used is read directly from the the RT Structure Set metadata file. If the voxel belongs to multiple structures with density override, the RED value used is the highest of them. In this case, and if the external contour also has a density override defined, its RED value is ignored. If the voxel belongs to a structure without custom density assigned, its RED value is obtained from the CT calibration curve using the voxel HU.
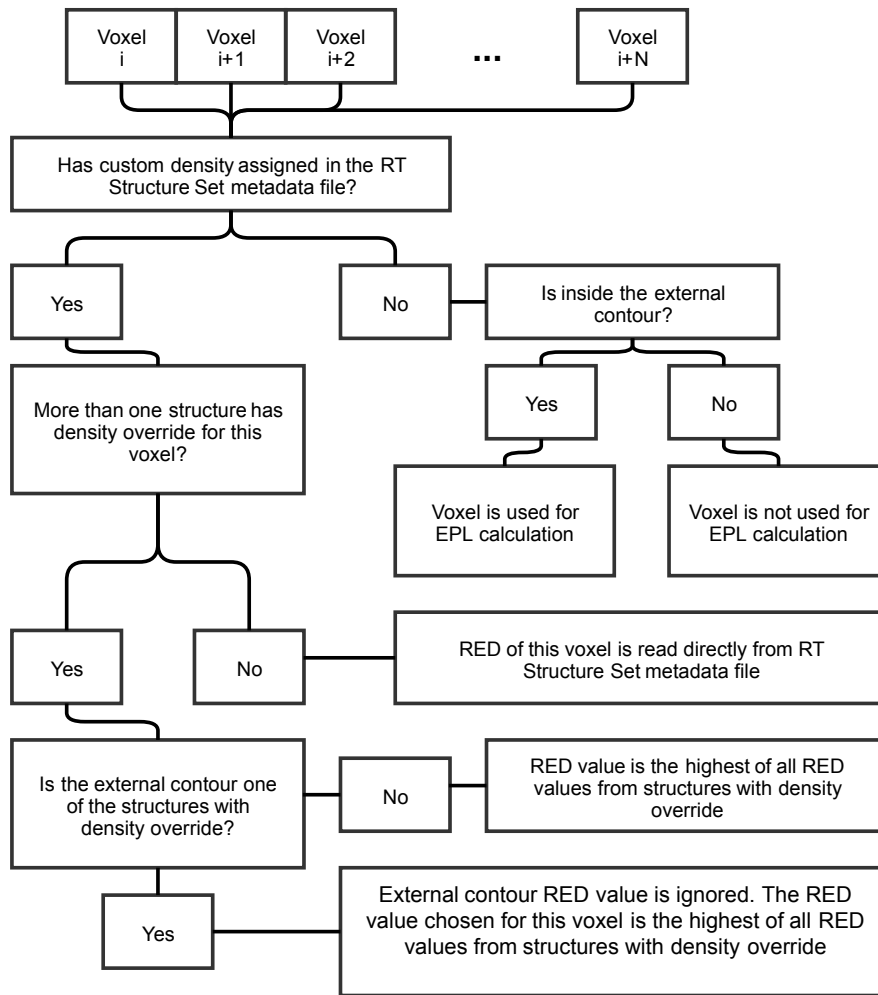
Figure 45: Voxel RED calculation.

The difference between the MU of all treatment fields per treatment fraction with heterogeneity correction and the MU calculated by CDC is given by:

$$\text{Difference } (\%) = \frac{\text{MU}_{WHC} - \text{MU}_{CDC}}{\text{MU}_{CDC}} \times 100 \qquad (6.49)$$

Where MU_{WHC} is the number of MU calculated by the application with heterogeneity correction and MU_{CDC} is the number of MU calculated by CDC algorithm.

6.2.6 Algorithm validation

The developed MATLAB® algorithm was tested in different MU calculation scenarios, with and without heterogeneity correction. Several tests were performed because many data is processed. Initially, beam data including TMR, OAR and OF is processed in "Beam Configuration" application. Then, DICOM patient data is processed in "Stereotactic MU Calculator" application. To despite any MU calculation error, all energies on both LINACs were tested with multiple collimators (a small, an intermediate and a large collimator when possible).

An additional test to verify depth calculation was performed because depth and effective depth are calculated from scratch and they can influence TMR value. For instance, at 5 cm depth, a depth calculation error of 1 mm leads to a difference of 0.4% to 0,5% in TMR calculation, reflecting a dose difference of 1% if the depth calculation error is 2 mm.

6.2.6.1 Depth calculation

Depth calculation was validated in Lucy® 3D QA phantom, simulating real treatment plans with multiple static fields using different isocenters, gantry angles and couch rotations (table 16). SSD was calculated from depth and compared to the planned SSD from TPS. Plans were created for TrueBeam™ STx. There is no need to verify depth calculation in Novalis Tx™ because the method is the same for both LINACs.

Table 16: Static field parameters used to validate depth calculation.

Gantry Rtn. (º)	Couch Rtn. (º)	TPS SSD (cm)
0	0	93.8
90	0	91.6
210	0	94.8
0	20	93.8
80	90	90.7
210	340	94.4

6.2.6.2 MU calculation without heterogeneity correction

Static fields and arcs with coplanar and non-coplanar beams were used to validate MU calculation without heterogeneity correction. Beam parameters used for TrueBeam™ STx and Novalis Tx™ are given on appendix B.1.

6.2.6.3 MU calculation with heterogeneity correction

MU calculation with heterogeneity correction cannot be compared to CDC because this algorithm does not have into account heterogeneities. Instead, the dose calculated by the developed algorithm was compared to the absorbed dose measurement in a QUASAR™ thorax phantom.

QUASAR™ thorax phantom was chosen because it has multiple insert locations and it is possible to choose inserts with different densities and sizes. The phantom has 5 small inserts with different densities, from a RED of 0.25 to a RED of 1.36. It also has two big inserts of cedar wood and acrylic [47].
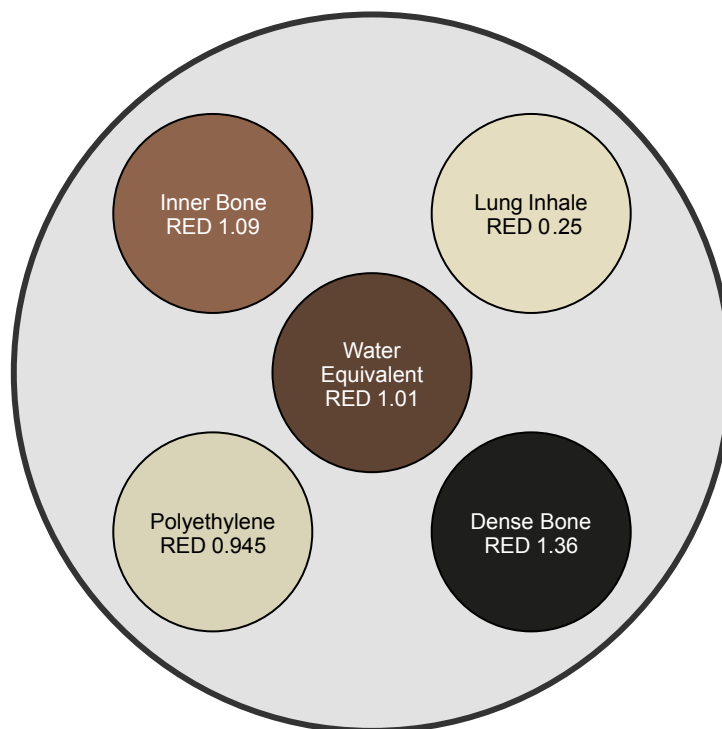
Figure 46: QUASAR™ thorax phantom small inserts available.

To simulate lung and bone, the cedar wood insert and the bone insert with a RED of 1.36 were chosen, respectively. The lowest density insert was placed in the left side of the phantom, in the left lung insertion. The highest density insert was placed in the central bottom insertion of the phantom, in the vertebrae position, to simulate bone.

The ionization chamber was placed at the isocenter (the intersection of the 3 external markers) in a special insert designed for the detector. CT scan was acquired without the ionization chamber. It was replaced by an insert with the same density as the ionization chamber special insert during the CT scan.
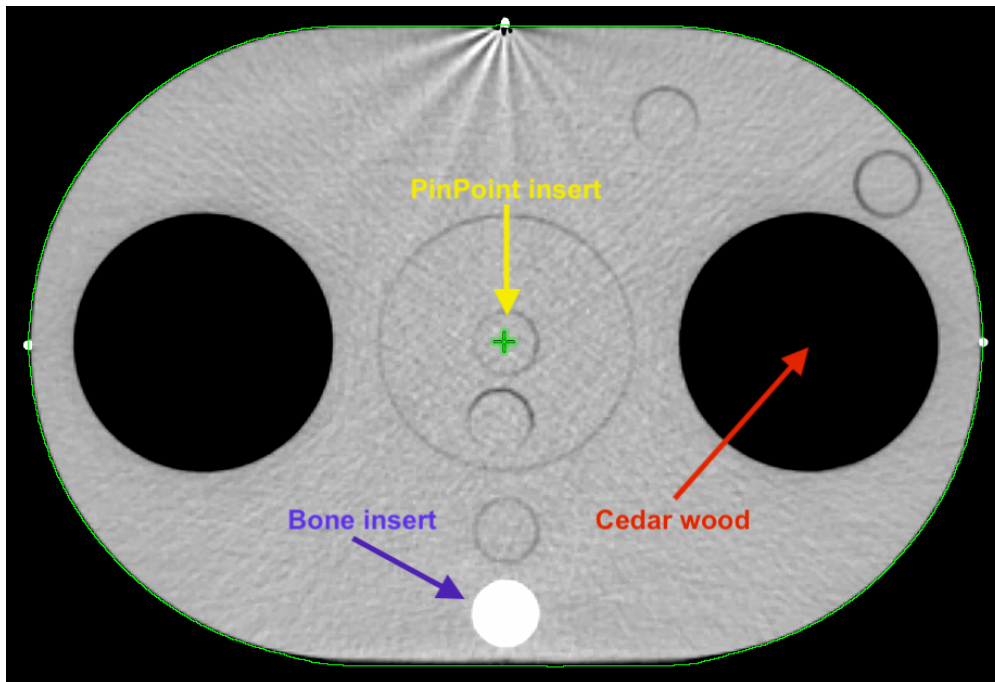
Figure 47: QUASAR™ thorax phantom axial plane with cedar wood inserts on the lungs position and bone insert on the vertebrae position.

To study the attenuation of cedar wood and bone densities, a lateral beam (incident on the lung insert) and a posterior beam (incident on the bone insert) were used. The dose absorbed by the ionization chamber on both beams should be different from the planned dose at the isocenter because cedar wood attenuates less radiation than water and bone attenuates more radiation. An additional arc incident on the lung insert and on the bone insert during its trajectory was used to validate the MU calculation with heterogeneity correction on arcs. Couch attenuation was taken in consideration to the calculation of the effective depth.

The static fields and arcs used are shown on the next figure:

(a) 90º static field   (b) 180º static field   (c) Arc 0º − > 180º
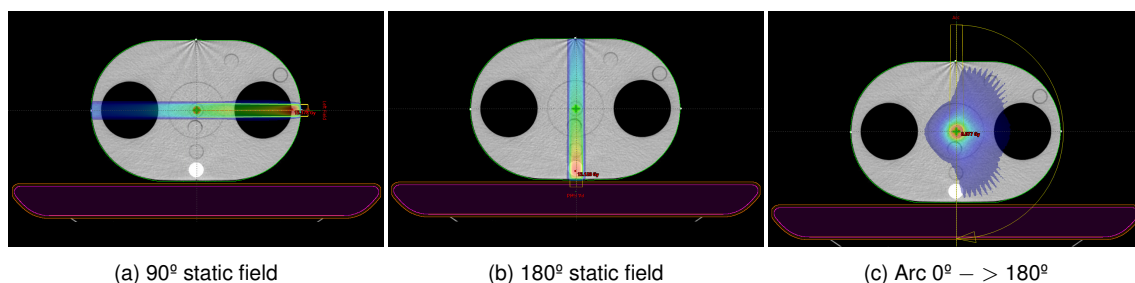
Figure 48: Static fields and arcs used to validate the MU calculation with heterogeneity correction using the QUASAR™ thorax phantom.

MU calculation with heterogeneity correction is strongly dependent on the effective depth calculation. A manual calculation of the effective depth for both static fields is presented in the 7.5.3 chapter. On the same chapter, the manual calculations are compared to the

effective depth calculated by the MATLAB® algorithm.

A PTW PinPoint 3D 31016 was used to measure the dose at the center of the phantom. Output correction factors from TRS-483 were used.

6.2.6.4 Patient plans MU verification

The final verification and validation were performed in patient plans. Radiosurgery patients previously treated at IPO Porto in TrueBeam™ STx and Novalis Tx™ LINACs were randomly chosen. Differences between the MU calculated by CDC and the MU calculated by the developed algorithm, with and without heterogeneity corrections, were obtained using the following equations:

$$\text{Difference WHC } (\%) = \frac{\text{MU}_{WHC} - \text{MU}_{CDC}}{\text{MU}_{CDC}} \times 100 \qquad (6.50)$$

$$\text{Difference NHC } (\%) = \frac{\text{MU}_{NHC} - \text{MU}_{CDC}}{\text{MU}_{CDC}} \times 100 \qquad (6.51)$$

Where MU_{WHC} and MU_{NHC} are the number of MU calculated by the developed algorithm with and without heterogeneity correction respectively and MU_{CDC} is the number of MU calculated by CDC algorithm.

7   Results and Discussion

7.1   Absolute Dosimetry

Absolute dosimetry was performed during the commissioning for both LINACs . Data was extracted from TPS in CDC configuration algorithm:

Table 17: Absolute dosimetry results in reference conditions. Dose is corrected for influence quantities.

LINAC	Energy	Ref. MU	Ref. Dose (Gy)
TrueBeam™ STx	6 FFF	100.00	0.925
TrueBeam™ STx	10 FFF	100.80	1.000
Novalis Tx™	6X SRS	106.05	1.000

7.2   Relative Dosimetry

7.2.1   OF

For OF calculation some equivalent square field size correction factors were used. Table 26 from TRS-483 presents the correction factors for the detector used, PTW microDiamond 60019. This table specifies the OF correction factors for fields collimated by MLC or SRS cones for 6 MV WFF and FFF energies, as a function of the equivalent square field size. Correction values for 10 MV WFF and FFF energies are specified in Table 27 of TRS-483.

Table 18: TrueBeam™ STx and Novalis Tx™ cone size with the equivalent square field size and the corresponding OF correction factor, for 6 FFF, 10 FFF and 6X SRS energies using PTW microDiamond 60019 detector.

Cone Size (mm)	Eqv. Square Field Size (mm)	Correction factor
4.0	3.545	0.95134
5.0	4.431	0.95815
6.0	5.317	0.96402
7.5	6.647	0.97133
10.0	8.862	0.98039
12.5	11.078	0.98661
15.0	13.293	0.99089
17.5	15.509	0.99383

The cone equivalent square field size was determined with equation (6.3). Correction factors were fitted into a two term exponential curve, defined in equation (6.4). The following curve fit coefficients were obtained:

```
Coefficients (with 95% confidence bounds):
a =             1   (0.9998, 1.001)
b =  -5.902e-06    (-1.829e-05, 6.488e-06)
c =    -0.08929    (-0.09115, -0.08743)
d =     -0.1689    (-0.1744, -0.1633)
```
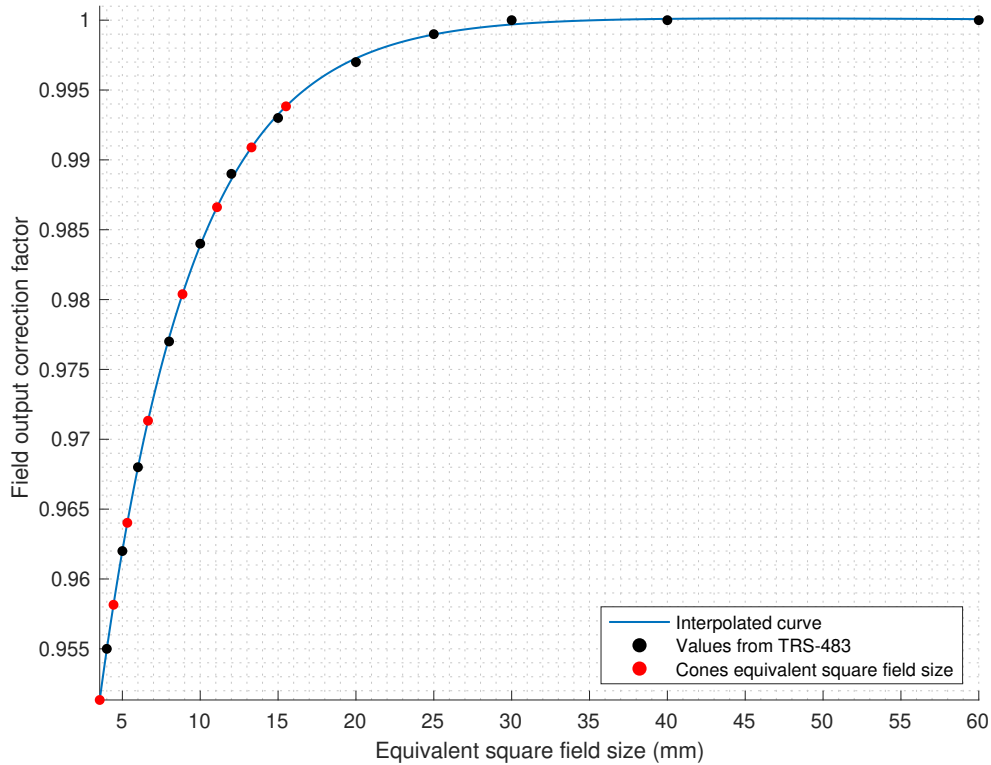

Figure 49: OF correction factors for PTW microDiamond 60019 as a function of the equivalent square field size. Red dots are the TrueBeam™ STx and Novalis Tx™ cones equivalent square field size. Valid for 6 FFF, 10 FFF and 6X SRS energies.

OF were determined using equation (6.2). For every cone size, the detector was irradiated with 100 MU at 95 cm SSD and 5 cm depth. The next two tables summarizes the OF values calculated, with correction factors applied, for TrueBeam™ STx and Novalis Tx™.

Table 19: TrueBeam™ STx OF table for 6 FFF and 10 FFF.

Cone Size (mm)	OF 6 FFF	OF 10 FFF
4.0	0.56176	0.47354
5.0	0.63126	0.54974
7.5	0.72391	0.66245
10.0	0.77311	0.73110
12.5	0.81570	0.79056
15.0	0.83532	0.82468
17.5	0.85294	0.85303

Table 20: Novalis Tx™ OF table for 6X SRS.

Cone Size (mm)	OF 6X SRS
4.0	0.55188
6.0	0.65918
7.5	0.70837
10.0	0.76564
12.5	0.79668
15.0	0.82215

A two term exponential curve fit, defined in equation (6.18), was applied to the OF values with correction factors. The following coefficients were obtained:

```
Coefficients for 6 FFF (TrueBeam STx) (with 95% confidence bounds):
a =      0.7452  (0.6324, 0.858)
b =    0.008005  (-0.0007622, 0.01677)
c =     -0.7526  (-1.102, -0.4032)
d =     -0.3246  (-0.5279, -0.1213)


Coefficients for 10 FFF (TrueBeam STx) (with 95% confidence bounds):
a =      0.7078  (0.5332, 0.8825)
b =     0.01132  (-0.001915, 0.02455)
c =     -0.7424  (-0.9349, -0.5498)
d =     -0.2582  (-0.4339, -0.08248)


Coefficients for 6X SRS (Novalis Tx) (with 95% confidence bounds):
a =      0.7472  (0.6434, 0.8509)
b =    0.007059  (-0.001369, 0.01549)
c =      -0.695  (-0.8025, -0.5874)
d =     -0.2915  (-0.4103, -0.1726)
```

A plot of the OF values obtained for both LINACs are shown on the next two figures along with the exponential curve obtained for each energy.
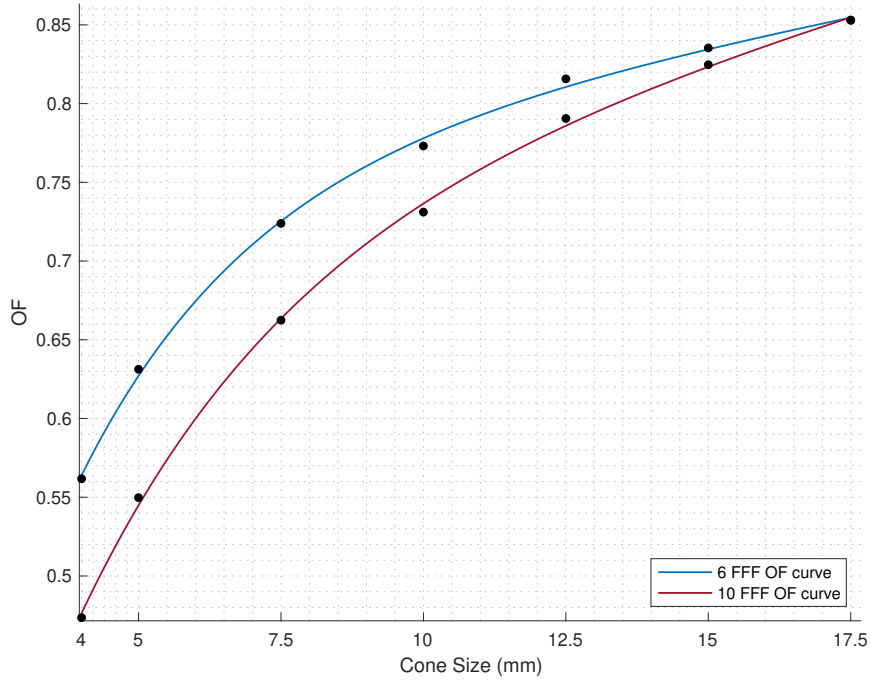
Figure 50: TrueBeam™ STx OF two term exponential curve for 6 FFF and 10 FFF.
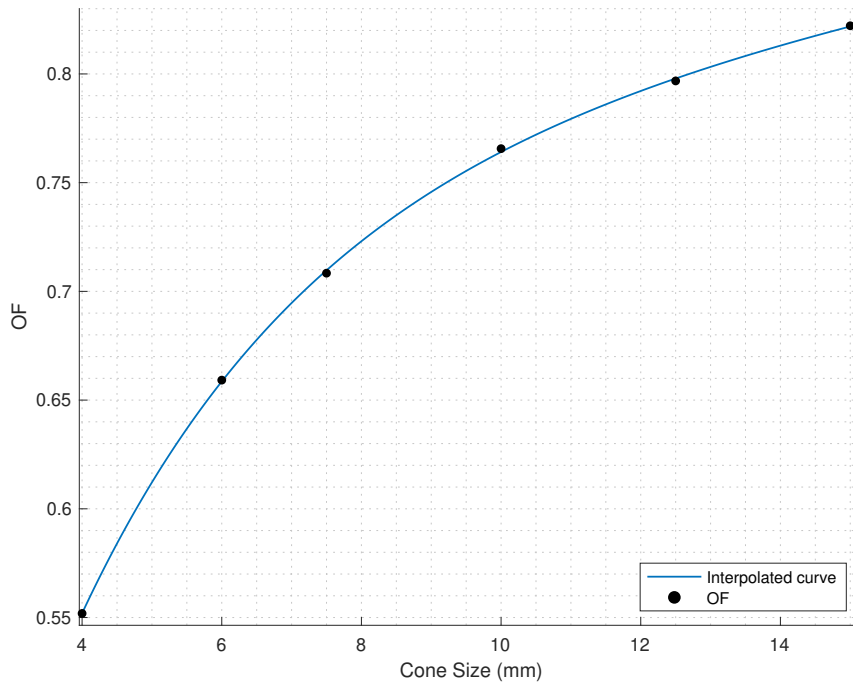
Figure 51: Novalis Tx™ OF two term exponential curve for 6X SRS.

7.2.2 TMR

TMR was acquired for 4, 7.5, 10 and 17.5 mm stereotactic cones for TrueBeam™ STx.
For Novalis Tx™, cones 4, 6, 10 and 15 mm were acquired. The remaining cones were
interpolated.

The following graphics shows the genuine TMR curves acquired without any processing
for TrueBeam™ STx (6 FFF / 10 FFF) and Novalis Tx™ (6X SRS).
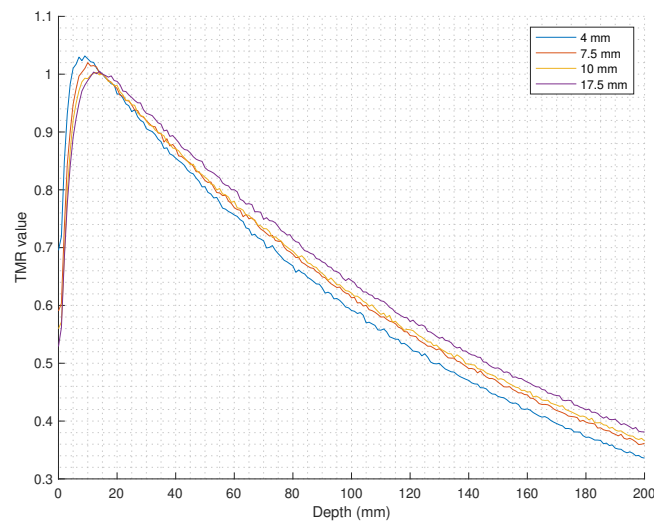
Figure 52: TrueBeam™ STx acquired TMR for 6 FFF energy without any enhancements.
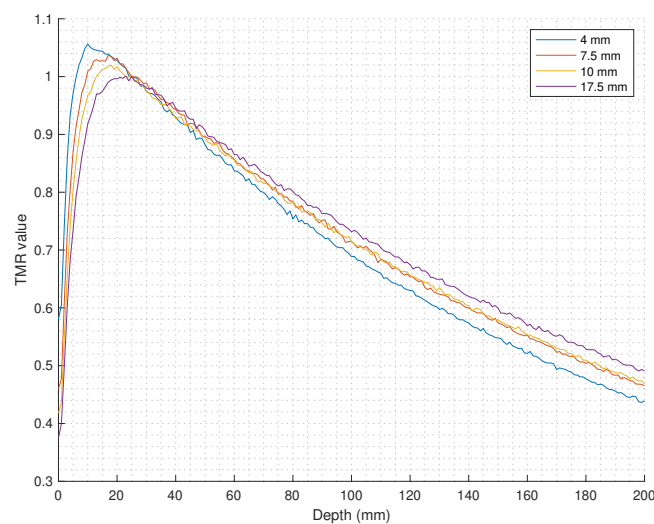
Figure 53: TrueBeam™ STx acquired TMR for 10 FFF energy without any enhancements.
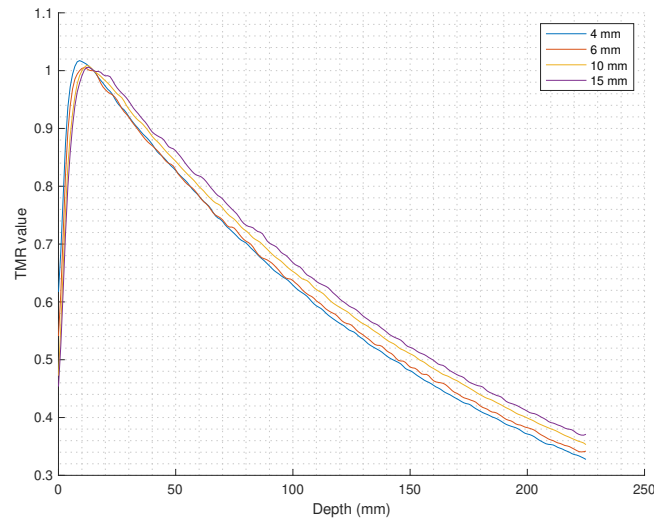
Figure 54: Novalis Tx™ acquired TMR for 6X SRS energy without any enhancements.

Data was smoothed to decrease the measurement noise, according to the different methods explained in the chapter 6.2.4.2. The resulting smoothed TMR curves are presented in appendix A.1 for TrueBeam™ and in appendix A.2 for Novalis Tx™. Figures 75, 77 and 79 shows TMR data smoothed with a local regression method using weighted linear least squares and a 2nd degree polynomial model. Figures 76, 78 and 80 shows TMR data fited into a two-term exponential model, defined previously in equation (6.11).

7.2.3 OAR

OAR was acquired for all cones. The irradiation conditions for OAR displayed below were 95 cm SSD and 5 cm depth. No smoothing was applied because curves come with no noise. Curves were averaged (negative side with positive side) and then cut in half.
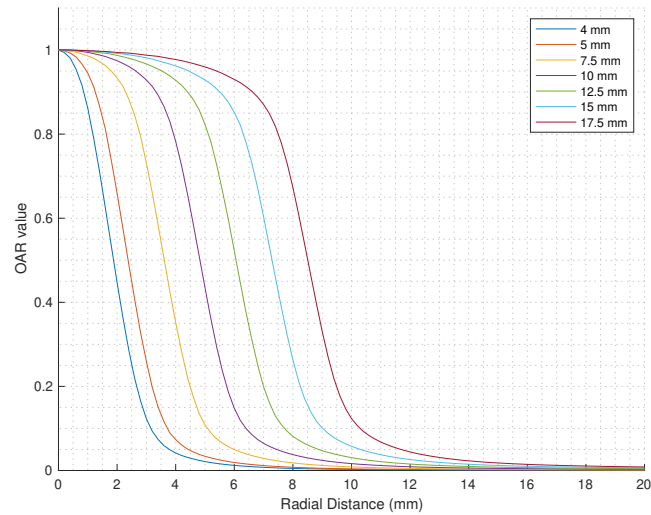
Figure 55: TrueBeam™ STx OAR for 6 FFF energy.
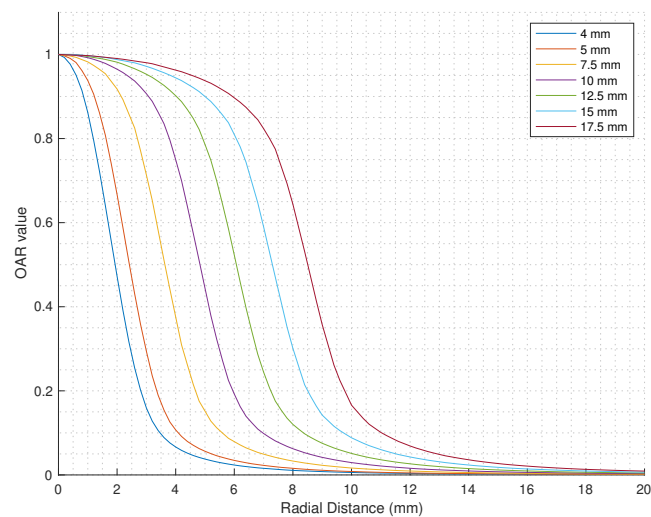
Figure 56: TrueBeam™ STx OAR for 10 FFF energy.
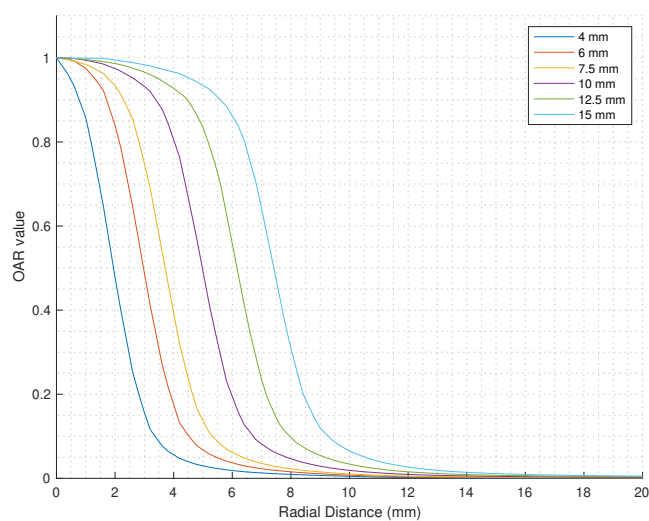
Figure 57: Novalis Tx™ OAR for 6X SRS energy.

7.3 FWHM film measurements

FWHM film measurements were performed on TrueBeam™ STx LINAC using 6 FFF energy.

7.3.1 Calibration curve

The MPV of red, green and blue colour channels of each irradiated film including the background film are displayed below:

Table 21: MPV of all colour channels.

Dose (Gy)	MPV Red	MPV Green	MPV Blue
0 (Background)	46805	44864	30294
0.422	42183	42572	29981
0.844	39011	40830	29899
1.689	33832	37585	29437
3.377	27466	32597	28371
6.754	20757	26258	26313
8.443	18703	24256	25223
12.665	15214	20434	23331
16.886	12999	17607	21582
21.108	11358	15205	20251

The following netOD values were obtained using equation (6.5):

Table 22: netOD of all colour channels.

Dose (Gy)	netOD Red	netOD Green	netOD Blue
0.422	0.04515	0.02278	0.00451
0.844	0.07910	0.04092	0.00571
1.689	0.14096	0.07689	0.01247
3.377	0.23150	0.13873	0.02848
6.754	0.35312	0.23263	0.06119
8.443	0.39839	0.26709	0.07957
12.665	0.48806	0.34154	0.11342
16.886	0.55637	0.40622	0.14728
21.108	0.61499	0.46991	0.17493

Only red channel was used. The netOD values for this channel were fitted in the 4th polynomial degree of equation (6.6). The function coefficients were the following:

```
Coefficients (with 95% confidence bounds):
a =        206  (131.2, 280.8)
b =      -179.3 (-290.2, -68.49)
c =       84.39 (32.9, 135.9)
d =        2.98 (-4.533, 10.49)
```
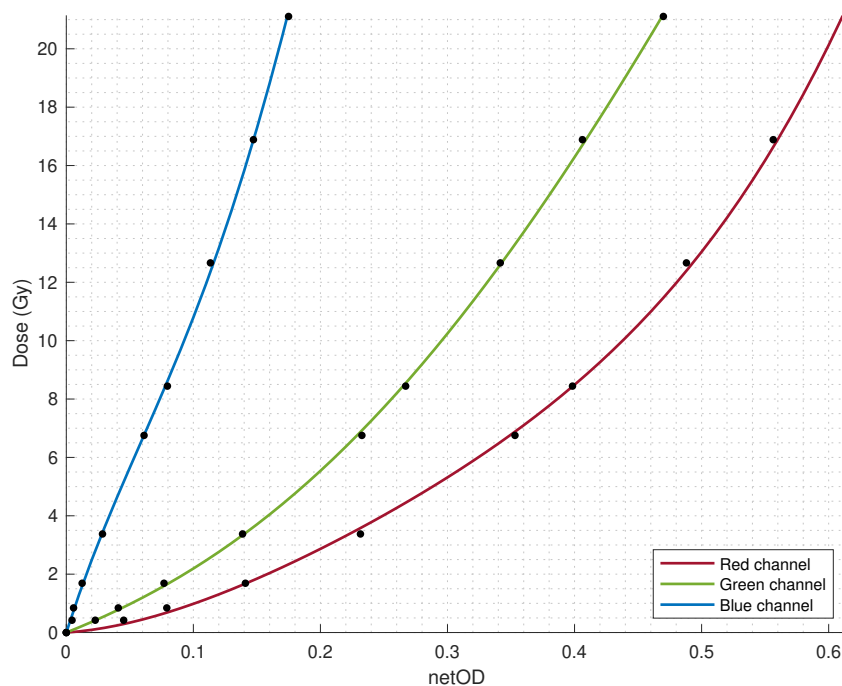

Figure 58: EBT3 calibration curve.

7.3.2 Film analysis
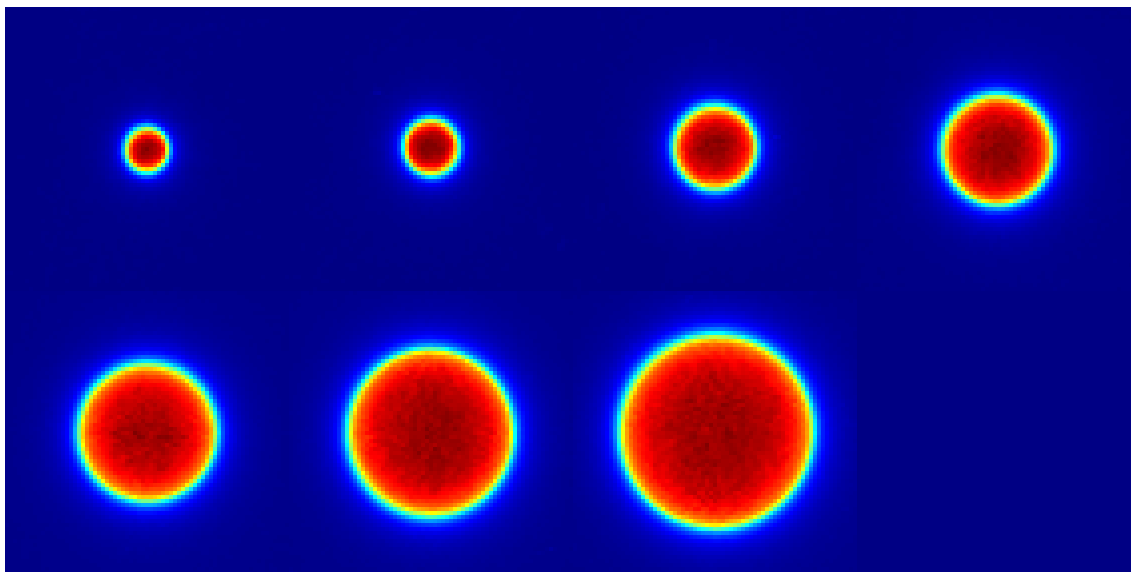
Figure 59: Red channel in *jet* colour scale of all TrueBeam™ STx collimators. Images are ordered from the smallest to the largest cone, from the left to the right, from the top to the bottom.

The following table compares the FWHM measured by film irradiation and through PTW microDiamond (extracted from OAR curves). The difference between them is shown in the last column.

Table 23: TrueBeam™ STx stereotactic cones FWHM measured by film irradiation and microDiamond.

Cone Size (mm)	Film FWHM (mm)	microDiamond FWHM (mm)	Difference (mm)
4	3.797	3.762	+0.035
5	4.875	4.756	+0.119
7.5	7.253	7.226	+0.027
10	9.644	9.658	-0.014
12.5	12.074	12.122	-0.048
15	14.599	14.580	+0.019
17.5	16.963	17.018	-0.055

7.4 CT calibration curve

The calibration curve used was the curve obtained for the TPS commissioning, as shown below.

Table 24: GE LightSpeed RT16 relative electron density calibration curve.

HU	Rel. Density
-1000	0.001
-722	0.250
-81	0.945
37	1.010
261	1.090
763	1.360
3254	2.550

Calibration curve was interpolated linearly from the lowest to the highest HU.
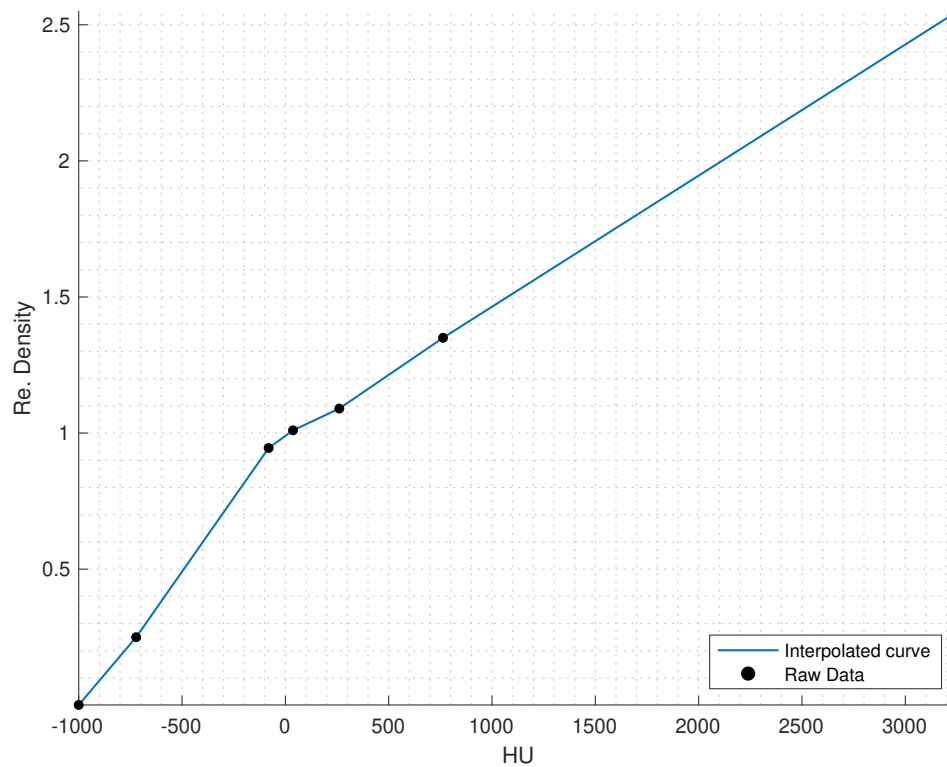
Figure 60: GE LightSpeed RT16 relative electron density calibration curve.

7.5   Algorithm validation

7.5.1   Depth calculation

To validate depth calculation, SSD was obtained with a MATLAB® algorithm and then compared with the SSD from TPS. Both SSD values were rounded to the nearest integer, in millimeters.

Table 25: Results of depth calculation validation using LUCY 3D QA phantom.

Gantry Rtn. (º)	Couch Rtn. (º)	TPS SSD (cm)	Calculated SSD (cm)	Difference (mm)
0	0	93.8	93.9	1
90	0	91.6	91.6	0
210	0	94.8	94.8	0
0	20	93.8	93.9	1
80	90	90.7	90.7	0
210	340	94.4	94.5	1

A maximum difference of 1 mm was found between the SSD calculated by the TPS and the SSD calculated with the MATLAB® algorithm.

7.5.2 MU calculation without heterogeneity correction

Results of MU calculation without heterogeneity correction validation is given on appendix C.1. The maximum difference registered was +2.07%. All the other values are below 2% difference.
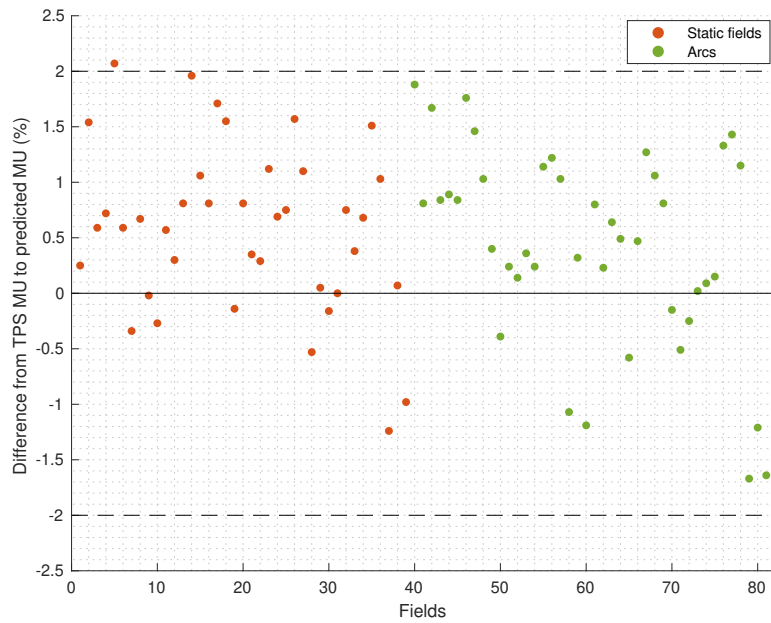
Figure 61: Scatter plot of MU calculation differences between TPS MU and predicted MU for static fields (orange dots) and arcs (green dots) in TrueBeam™ STx.
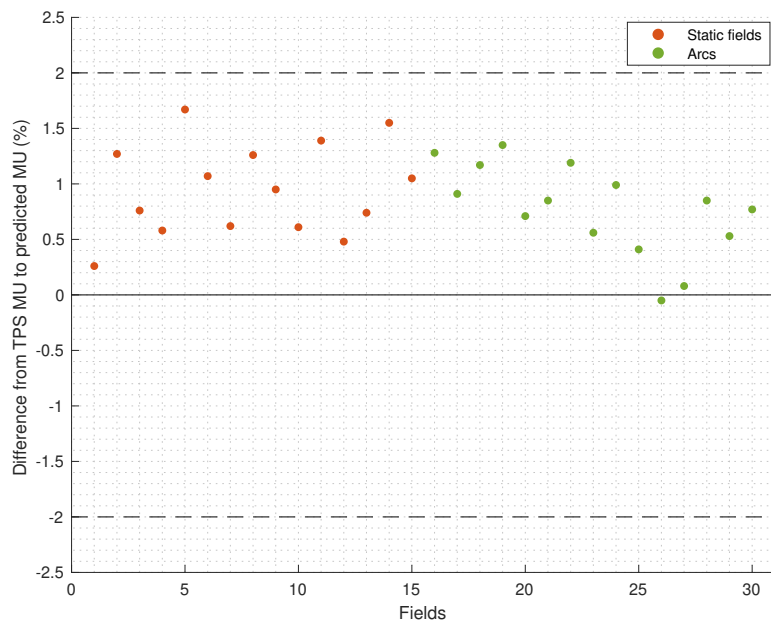
Figure 62: Scatter plot of MU calculation differences between TPS MU and predicted MU for static fields (orange dots) and arcs (green dots) in Novalis Tx™.

The results are within the expected because the algorithm developed without heterogeneity correction presented the same behaviour as CDC algorithm. For similar calculation algorithms for homogeneous conditions, AAPM TG-114 states a tolerance of 2% for fields using the same patient or phantom geometry with minimal field shaping [48].

7.5.3 MU calculation with heterogeneity correction

Manual effective depth calculation

For static fields, due to QUASAR™ thorax phantom simple geometry, effective depth can be calculated easily if RED value from the phantom and inserts are known.

QUASAR™ thorax phantom measures 30 cm width and 20 cm height [47]. Ionization chamber is placed at the center of the phantom. In a lateral beam that crosses the lung insert (gantry rotation 90º), the distance from the isocenter to the phantom surface is 15 cm (half of the phantom width). The lung insert measures 8 cm diameter. That means there are 7 cm of phantom material and 8 cm of cedar wood between the isocenter and the surface of the phantom. RED values of these regions are obtained tracing a path between the isocenter and the surface of the phantom (the voxel where the beam enters on the phantom along the CAX). A graphical representation of that ray trace is given on figure 63.
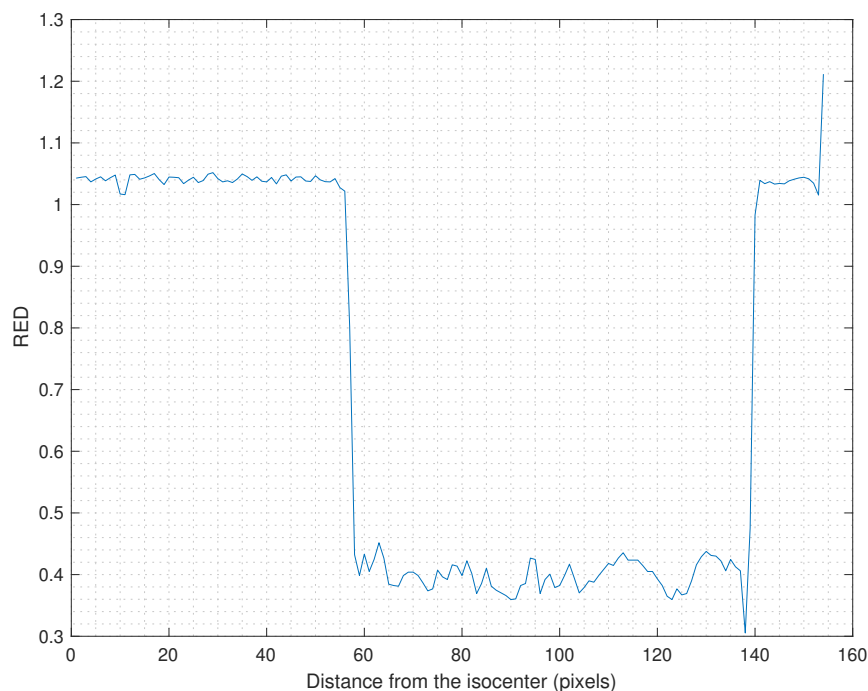
Figure 63: RED values along the QUASAR™ thorax phantom between the isocenter and the surface of the phantom, for a 90º static field.

The average RED for the phantom material is very close to the water, 1.0397 and the average RED of the cedar wood is 0.3995.

Effective depth of the lateral field is:

$$d_{eff} = \sum_i \rho_i^{el} \times x_i = (1.0397 \times 7\,\text{cm}) + (0.3995 \times 8\,\text{cm}) = 10.47\,\text{cm}$$

However, the effective depth calculated in MATLAB® for this field is 10.50 cm because the external marker placed on the left side of the phantom is partially inside the external contour, as can be seen in figure 64. The marker presence also can be seen in figure 63. The spike at the end of the plot on the right side corresponds to the marker.

Including the external marker on the external contour increases the effective depth because the marker is composed by a dense material.
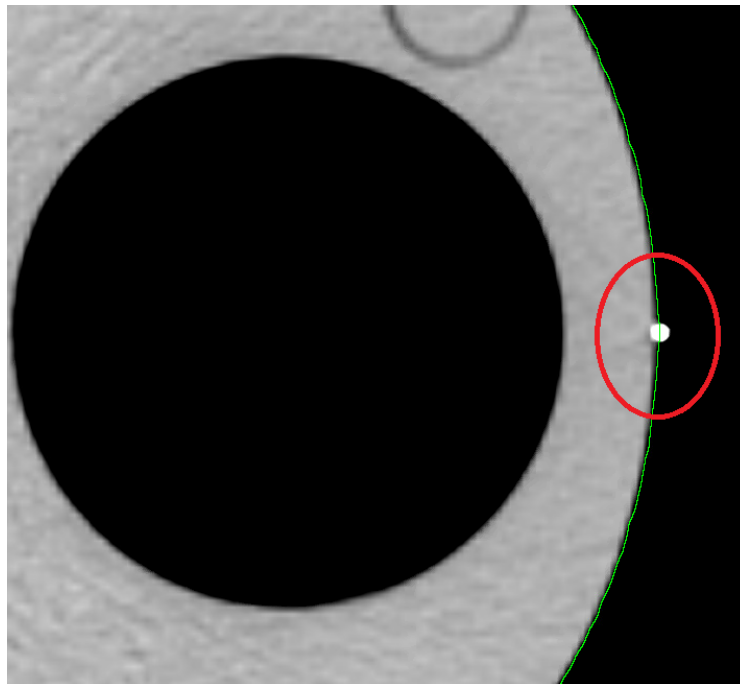
Figure 64: External marker partially inside the external contour of the phantom.

For the posterior beam that crosses the bone insert (gantry rotation 180º), the distance from the isocenter to the phantom surface is 10 cm (half of the phantom height) [47]. The bone insert measures 2 cm diameter. That means there are 8 cm of phantom material and 2 cm of bone between the isocenter and the surface of the phantom. A graphical representation of the ray trace between these two locations is given on figure 65.
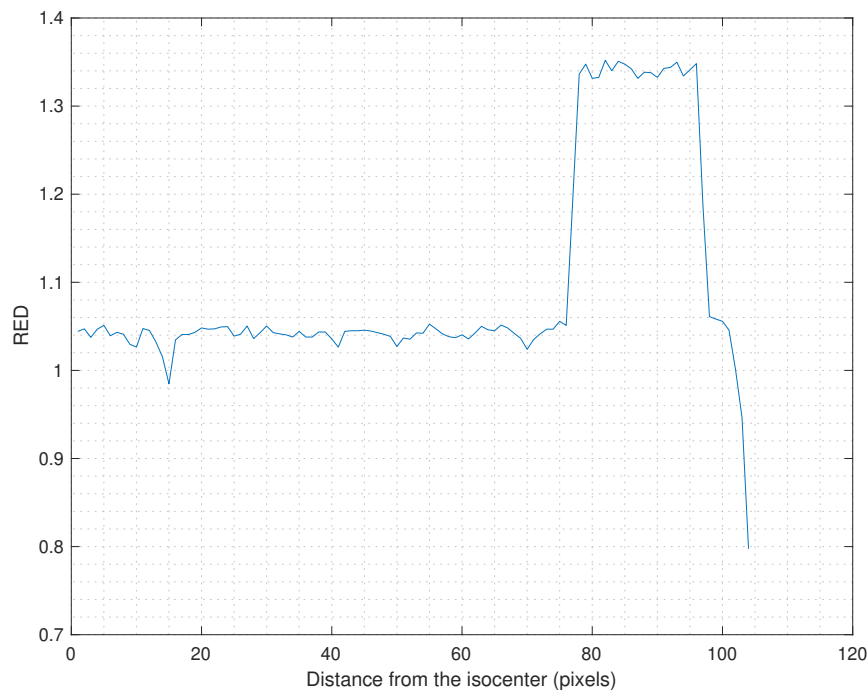
Figure 65: RED values along the QUASAR™ thorax phantom between the isocenter and the surface of the phantom, for a 180º static field.

The average RED for the phantom material is 1.0411, which is very close to the previous RED obtained for the lateral beam, with a difference of only 0.0014. The RED for the bone insert is 1.3411, which is very close to the 1.36 RED value announced by the phantom manufacturer.

Effective depth of the posterior field is:

$$d_{eff} = \sum_i \rho_i^{el} \times x_i = (1.0411 \times 8\,\text{cm}) + (1.3411 \times 2\,\text{cm}) = 11.01\,\text{cm}$$

Effective depth calculated in MATLAB® for this field is 11.13 cm. The difference might be explained because external contour includes the phantom edge, as shown on figure 66. External contour by default is drawn automatically in Eclipse™ workspace and is based on threshold values. The lower threshold for the external contour is -350 HU. Everything that is above this value is drawn as external contour.
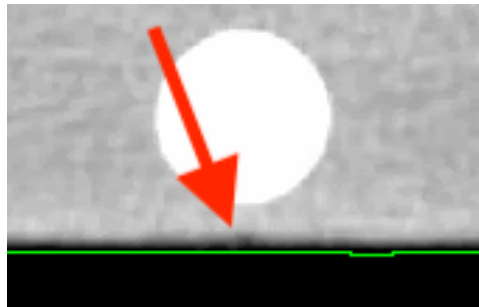
Figure 66: Phantom edge included in the external contour of the phantom. The external contour is represented by the green line.

The phantom edge is noticeable in figure 65. The RED drop at the end of the plot is the phantom edge, which has a RED value inferior to the phantom material:

Figure 67: RED drop caused by the phantom edge.

Including the phantom edge on the external contour of the phantom increases the effective depth and might be responsible for the 1.2 mm difference between the effective depth calculated manually and calculated in MATLAB®.

Another factor that needs to be taken into account is the couch attenuation. The couch model was added as a structure with custom density in Eclipse™ TPS for QUASAR™ thorax phantom plans. TrueBeam™ STx and Novalis Tx™ have a similar couch with a superior and inferior surface and a hollow interior, as shown below:
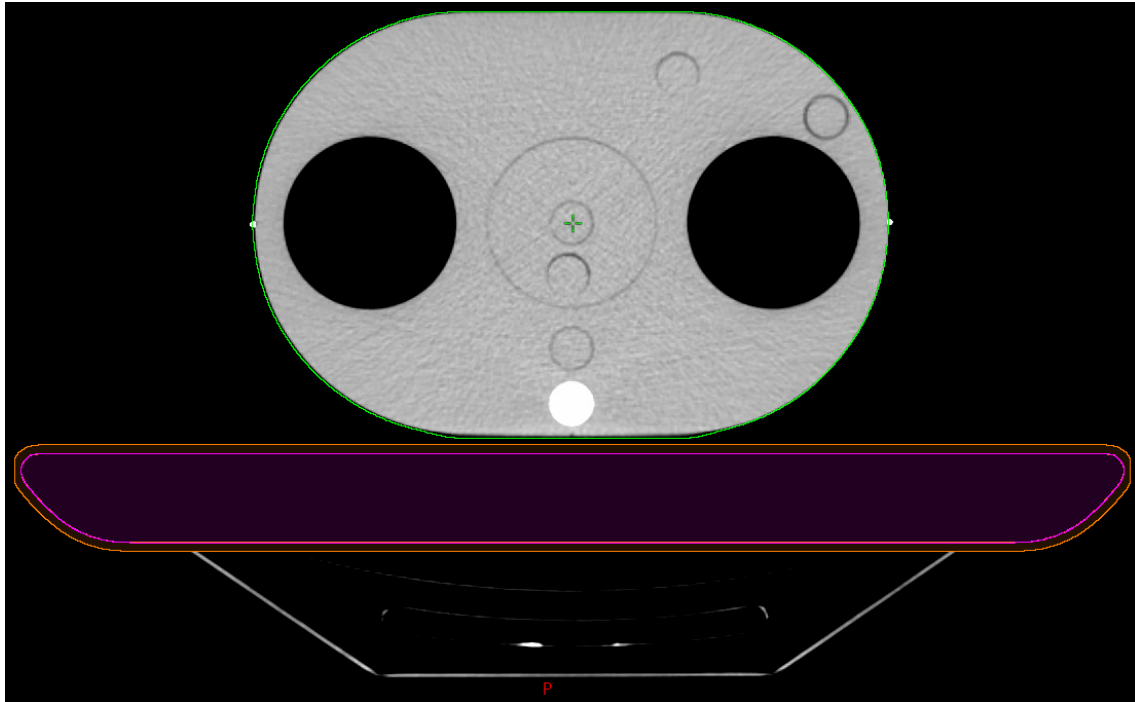
Figure 68: TrueBeam™ STx couch. The hollow interior and the couch surface are represented in magenta and orange contours with a RED of 0.0447 and 0.3224 respectively.

A couch attenuation of 5 mm of water equivalent was found for both LINACs when the beam is incident perpendicularly to the couch. This value was added to the effective depth calculated for the posterior 180º static field. However, for the arc between 0º and 180º, the couch attenuation varies with the gantry angle. In this particular case, the couch starts attenuating the beam when the gantry angle reaches 113º. Effective depth from 113º to 180º with and without couch attenuation is shown on figure 69a and its difference on figure 69b. As explained earlier, arcs are segmented into multiple static fields with 1º gantry angle resolution. For each angle, the couch attenuation was calculated and the value was added to the effective depth.

For patient plans, the couch model should be exported from Eclipse™ with custom density assigned. Any other structures that attenuate the beam should be included also.
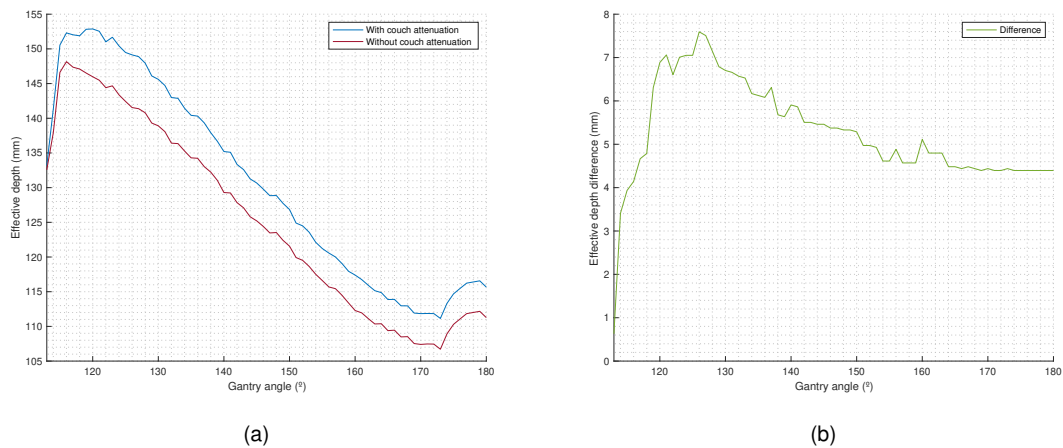
Figure 69: On the left: effective depth calculated between the gantry angle where the couch starts attenuating the beam (113º) and the end of the beam (180º). On the right: difference between the effective depth with and without couch attenuation, for the same gantry angles. The green line on (b) is the difference between the blue line and the red line on (a). Calculated for the TrueBeam™ STx couch and QUASAR™ thorax phantom using a arc between 0º and 180º for the heterogeneity correction validation tests.

Static fields and arcs used to validate MU calculation with heterogeneity correction for TrueBeam™ STx and Novalis Tx™ are given on appendix B.2.

Output correction factors for PTW PinPoint 31016

The output correction factors for the PTW PinPoint 31016 were obtained using the same methodology of PTW microDiamond 60019. Cone equivalent square field size was determined with equation (6.3). Correction factors were fitted into a two term exponential curve, defined in equation (6.4). The following curve fit coefficients were obtained:

```
Coefficients (with 95% confidence bounds):
a =      0.3626  (0.3091, 0.4162)
b =     -0.2229  (-0.2382, -0.2076)
c =           1  (0.9989, 1.001)
d =   5.981e-08  (-2.018e-05, 2.03e-05)
```

Table 26: Cone size with the equivalent square field size and the corresponding OF correction factor, for 6 FFF, 10 FFF and 6X-SRS energies using PTW PinPoint 31016 detector.

Cone Size (mm)	Eqv. Square Field Size (mm)	Correction factor
10.0	8.862	1.05030
12.5	11.078	1.03070
15.0	13.293	1.01874
17.5	15.509	1.01144
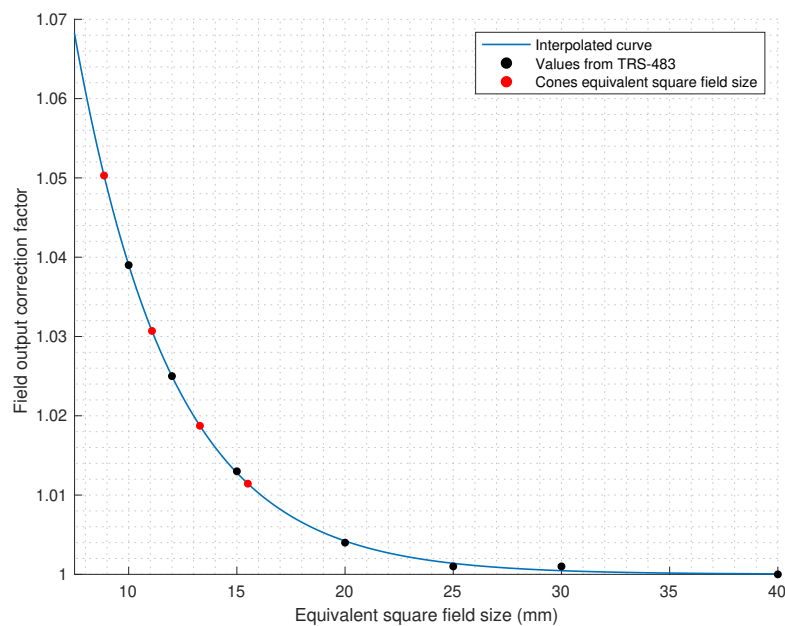
Figure 70: OF correction factors for PTW PinPoint 31016 as a function of the equivalent square field size. Red dots are the cones equivalent square field size. Valid for 6 FFF, 10 FFF and 6X SRS energies.

MU calculation results

Results of MU calculation with heterogeneity correction validation is given on appendix C.2. For the sake of clarity, results will be divided in three incidences: the 90º lateral beam, the 180º posterior beam and the arc between 0º and 180º clockwise.

- 90º lateral beam: This beam crosses 8 cm of cedar wood and is expected to give larger deviations when compared to CDC calculations. The developed algorithm underestimates the dose for TrueBeam™ STx with an average of -1.70% for 6 FFF and -3.35% for 10 FFF. In Novalis Tx™ the dose was overestimated with an average of 0.95%. The dose underestimation for 10 FFF might be related with the energy of the beam. As AAPM Report nº 85 states, heterogeneity corrections are more complex and even contradictory as the energy increases [49]. However, this should not be a concern because most of the beams do not cross air cavities before reaching the target volume in radiosurgery treatments and 10 MV is not used too often as 6 MV in this type of stereotactic treatments;

- 180º posterior beam: This beam crosses 2 cm of the bone insert. A dose underestimation was found for TrueBeam™ STx with an average of -0.31% for 6 FFF and -2.13% for 10 FFF. However, for Novalis Tx™, an average of 3.76% was obtained;

- Arc between 0º and 180º clockwise: The developed algorithm overestimated the dose for 6 FFF and underestimated the dose for 10 FFF, with an average of 1.54% and -0.90% respectively. For Novalis Tx™, the average was 3.97%.

From the results we can observe that the developed algorithm always overestimates the dose for Novalis Tx™, especially for the 90º and 180º static fields. For TrueBeam™ STx, it always underestimated the dose for the 90º and 180º static fields. For the arc, it overestimated for 6 FFF and underestimated for 10 FFF.

The maximum difference registered was 4.36% for the clockwise arc in the Novalis Tx™ using 6X SRS energy. None of the observed differences exceeded the 5% tolerance stated by AAPM TG-114. This is the uncertainty widely accepted between the difference of the planned dose and the delivered dose, for an effective radiation treatment [48].
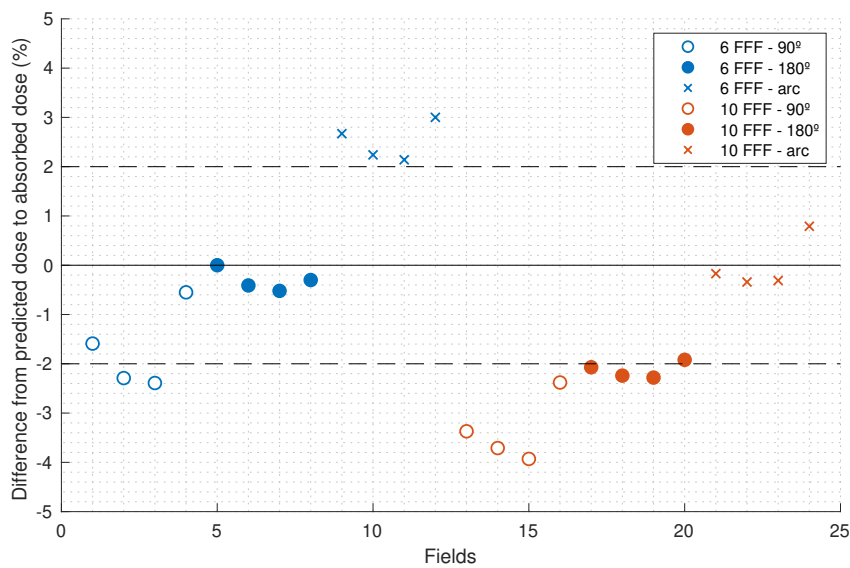
Figure 71: Scatter plot of dose calculation difference between predicted dose and absorbed dose for static fields and arcs in TrueBeam™ STx.
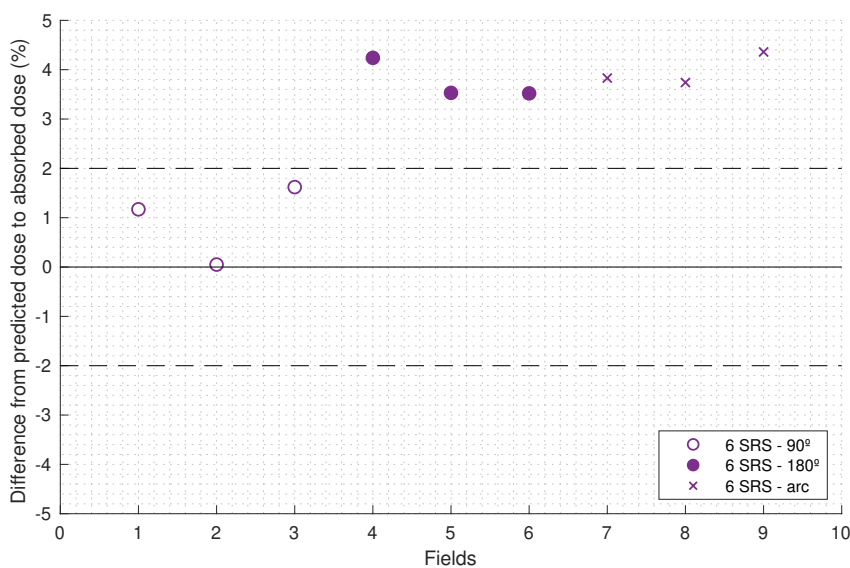
Figure 72: Scatter plot of dose calculation difference between predicted dose and absorbed dose for static fields and arcs in Novalis Tx ™.

7.5.4 Patient plans MU verification

A total of 12 patients (6 for each LINAC) were chosen to validate the software developed during this work. The results are presented on appendix D.1 for TrueBeam™ STx and on appendix D.2 for Novalis Tx™. Equations (6.50) and (6.51), given on chapter 6.2.6.4, were used to calculate the differences between the MU calculated by the CDC and the MU calculated by the developed software with and without heterogeneity correction.

The maximum difference found for MU calculation without heterogeneity correction was +1.40% on patient ID 7 from Novalis Tx™ (absolute average of 0.81% for all patients). The obtained results are within the expected because as stated before, the developed algorithm has a similar behaviour to the CDC algorithm when not using heterogeneity correction.

For MU calculation with heterogeneity correction, the maximum difference was +6.20% on patient ID 2 from TrueBeam™ STx and +5.91% on patient ID 12 from Novalis Tx™ (absolute average of 3.57% for all patients). In fact, these were the only patients whose deviation was higher than 5% for a treatment field. Figures 73 and 74 represent graphically the differences from CDC to the developed algorithm, with and without heterogeneity correction.

The developed algorithm always calculates more MU than CDC to compensate the tissue attenuation. Varian states that the dose error because bone attenuation is approximately 1.2% [34], however, the overall attenuation is higher.
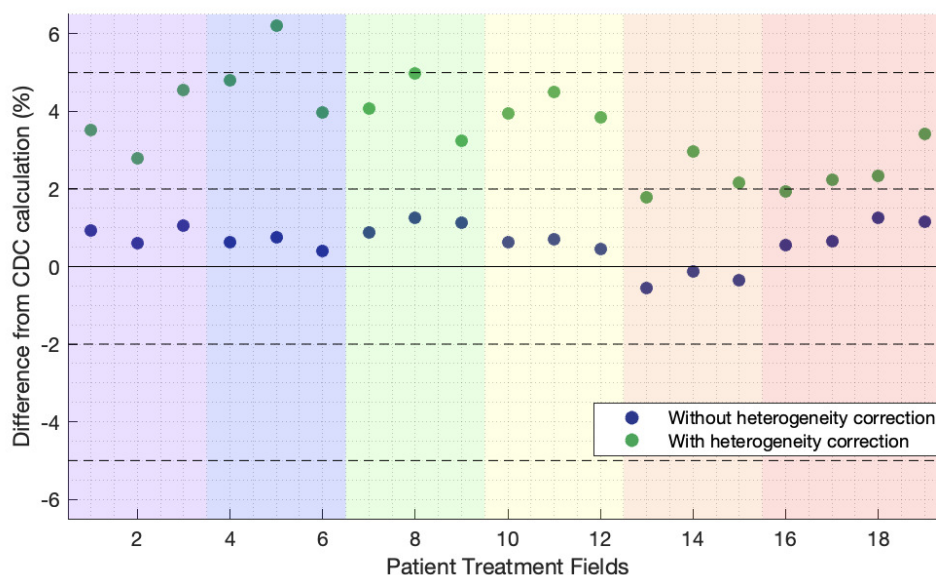
Figure 73: Differences from CDC calculation to the developed algorithm with and without heterogeneity correction in TrueBeam™ STx. Each background colour corresponds to a different patient. Green and blue dots are the differences from CDC to the developed algorithm with and without heterogeneity correction for each treatment field, respectively.
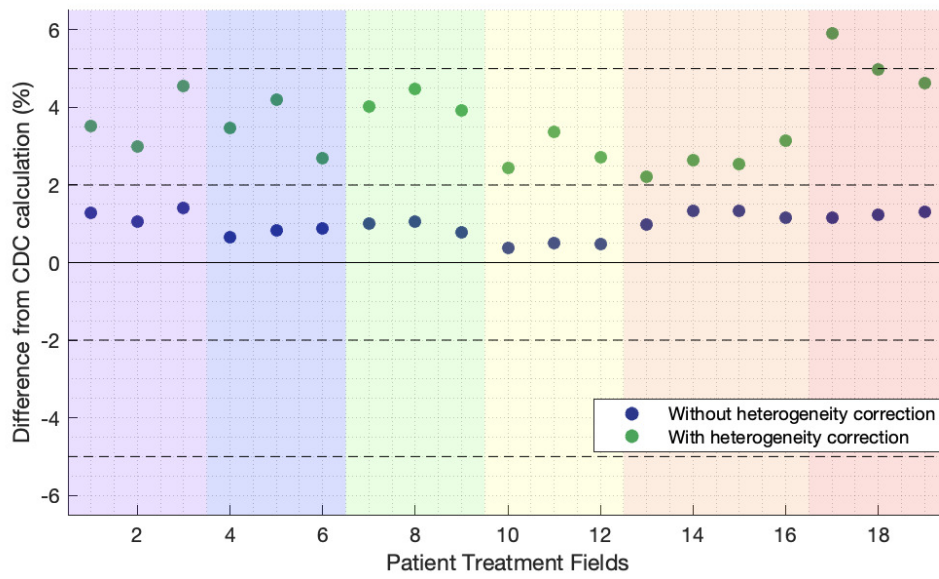
Figure 74: Differences from CDC calculation to the developed algorithm with and without heterogeneity correction in Novalis Tx™. Each background colour corresponds to a different patient. Green and blue dots are the differences from CDC to the developed algorithm with and without heterogeneity correction for each treatment field, respectively.

8   Conclusions

The main objective of this dissertation was the development of an independent MU calculator for stereotactic treatments with Varian and BrainLAB cone systems in a Varian TrueBeam™ STx and Varian Novalis Tx™. The goal of this independent MU verification is to ensure that the primary MU calculation is sufficiently accurate for the safe and effective treatment of patients.

In order to develop the independent MU calculator, TMR, OAR and OF measurements were taken in both LINACs using 6 FFF and 10 FFF energies for TrueBeam™ STx and 6X SRS energy for Novalis Tx™, following the dosimetry formalism for small fields proposed by the TRS-483. Additionally, FWHM of stereotactic cones was measured in TrueBeam™ STx using 6 FFF energy. A calibration curve was acquired to establish the relation between the film darkening and the absorbed dose.

The developed algorithm without heterogeneity was evaluated against CDC calculations for multiple plans using static fields and arcs in both LINACs. A 2% tolerance was established from AAPM TG-114. Since the calculation method from both algorithms is very similar, the results are within the expected with a maximum difference of +2.07% in one test from the algorithm validation without heterogeneity correction. For patients, the maximum deviation from CDC algorithm was +1.40%.

Regarding the heterogeneity correction, the software developed was validated with measurements in-phantom with an ionization chamber, for static fields and arcs. The 5% tolerance established was based on AAPM TG-114. A maximum difference of +4.36% was found in the validation tests. For patients, a maximum difference of +6.20% and +5.91% was found in two treatment fields of different patients, for TrueBeam™ STx and Novalis Tx™ respectively. These were the only treatment fields from the patient plans that exceeded the tolerance accepted for calculation with heterogeneity correction, in comparison with CDC calculation. The heterogeneity correction gives the ability to the dosimetrists and physicists to ponder different beam incidences in order to chose beams that crosses structures with less radiation attenuation.

9 Future work

Heterogeneity correction was the only CDC algorithm limitation that was implemented in the developed algorithms. Others limitations such as the beam obliquity and the absence of backscatter near cavities or surfaces where the beam exits are still present. Another limitation of the developed algorithms is related to the TMR calculation. TMR can't be calculated if the depth of the field is greater than the maximum TMR depth measured. For future work, these limitations should be taken into account.

Regarding algorithm validation with heterogeneity correction, dose measurements with an ionization chamber were performed only for stereotactic cones greater or equal than 10 mm due to the detector active volume size. For future work, the algorithm should be validated for smaller cones sizes (between 4 and 7.5 mm) with another dosimeter type (for example, radiochromic films).

Some improvements on relative dosimetry could be done using a PTW T-REF chamber, a new reference detector chamber for small fields. This transmission chamber can be placed directly under the LINAC head without interfering with the beam [50].

References

[1] World Health Organization. (Sep. 2018). Cancer, [Online]. Available at: https://www.who.int/news-room/fact-sheets/detail/cancer (accessed on 18/09/2018).

[2] H. Gelband, P. Jha, R. Sankaranarayanan and S. Horton, *Disease Control Priorities*, 3rd ed. Washington, DC: World Bank Publications, Nov. 2015, vol. 3.

[3] Direção-Geral da Saúde. (Sep. 2017). Programa Nacional para as Doenças Oncológicas, [Online]. Available at: https://www.dgs.pt/portal-da-estatistica-da-saude/diretorio-de-informacao/diretorio-de-informacao/por-serie-880762-pdf.aspx?v=11736b14-73e6-4b34-a8e8-d22502108547 (accessed on 18/09/2018).

[4] American Cancer Society. (Feb. 2017). Radiation Therapy Basics, [Online]. Available at: https://www.cancer.org/treatment/treatments-and-side-effects/treatment-types/radiation/basics.html (accessed on 19/06/2019).

[5] J. P. Kirkpatrick, S. G. Soltys, S. S. Lo, K. Beal, D. C. Shrieve and P. D. Brown, 'The radiosurgery fractionation quandary: single fraction or hypofractionation?' *Neuro-Oncology*, ii38–ii49, Apr. 2017.

[6] G. L. Masucci, 'Hypofractionated Radiation Therapy for Large Brain Metastases,' *Frontiers in Oncology*, vol. 8, Oct. 2018.

[7] C. Nieder, A. L. Grosu and L. E. Gaspar, 'Stereotactic radiosurgery (SRS) for brain metastases: a systematic review,' *Radiation Oncology*, vol. 9, no. 1, Jul. 2014.

[8] The International Commission on Radiation Units and Measurements, 'Prescribing, Recording, and Reporting of Stereotactic Treatments with Small Photon Beams,' ICRU Report 91, Jul. 2014.

[9] S. H. Levitt, J. A. Purdy, C. A. Perez and S. Vijayakumar, *Technical Basis of Radiation Therapy: Practical Clinical Applications*, 4th ed. Berlin: Springer, Jun. 2006.

[10] W. Schlegel, T. Bortfeld and A. L. Grosu, *New Technologies in Radiation Oncology*. Berlin: Springer, Aug. 2006.

[11] E. C. Haperin, D. E. Wazer, C. A. Perez and L. W. Brady, *Perez and Bradys Principles and Practice of Radiation Oncology*, 6th ed. Philadelphia: Wolters Kluwer health - Lippincott Williams & Wilkins, May 2013.

[12] J. P. Sheehan, S. T. Chao, D. M. Trifiletti and A. Sahgal, *Stereotactic Radiosurgery and Stereotactic Body Radiation Therapy: A Comprehensive Guide*. Springer, Jun. 2019.

[13] S. H. Benedict, D. J. Schlesinger, S. J. Goetsch and B. D. Kavanagh, *Stereotactic Radiosurgery and Stereotactic Body Radiation Therapy*. New York: CRC Press, Nov. 2016.

[14] D. E. Heron, M. S. Huq and J. M. Herman, *Stereotactic Radiosurgery and Stereotactic Body Radiation Therapy (SBRT)*. Demos Medical Publishing, Oct. 2018.

[15] Varian Medical Systems. TrueBeam Radiotherapy System, [Online]. Available at: https : / / www . varian . com / oncology / products / treatment - delivery / truebeam - radiotherapy-system (accessed on 04/02/2019).

[16] Varian Medical Systems. (Sep. 2013). TrueBeam Brochure, [Online]. Available at: https : / / www . varian . com / sites / default / files / resource_attachments / TrueBeamBrochure_RAD10119D_September2013.pdf (accessed on 04/02/2019).

[17] Varian Medical Systems. Intracranial Tracking, [Online]. Available at: https : / / www . varian . com / oncology / products / real - time - tracking - motion - management/intracranial-tracking (accessed on 18/02/2019).

[18] E. Borzov, A. Nevelsky, R. Bar-Deroma and I. Orion, 'Dosimetric characterization of Elekta stereotactic cones,' *Journal of Applied Clinical Medical Physics*, vol. 19, no. 1, 194–203, Sep. 2017.

[19] American Association of Physicists in Medicine, 'Quality assurance of medical accelerators,' Task Group 142, Aug. 2009.

[20] F. H. Attix, *Introduction to radiological physics and radiation dosimetry*. Weinheim: Wiley-VCH Verlag GmbH & Co. KGaA, Nov. 1986.

[21] J. E. Turner, *Atoms, radiation, and radiation protection*, 3rd ed. Weinheim: Wiley-VCH Verlag GmbH & Co. KGaA, May 2007.

[22] P. Mayles, A. Nahum and J. C. Rosenwald, *Handbook of Radiotherapy Physics: Theory and Practice*. New York: Taylor & Francis, Jun. 2007.

[23] H. Palmans, P. Andreo, M. S. Huq, J. Seuntjens, K. E. Christaki and A. Meghzifene, 'Dosimetry of small static fields used in external photon beam radiotherapy: Summary of TRS-483, the IAEA–AAPM international Code of Practice for reference and relative dose determination,' *Medical Physics*, vol. 45, no. 11, Sep. 2018.

[24] International Atomic Energy Agency, 'Dosimetry of Small Static Fields Used in External Beam Radiotherapy,' Vienna, Technical Report Series no. 483, Nov. 2017.

[25] P. Andreo, 'The physics of small megavoltage photon beam dosimetry,' *Radiotherapy and Oncology*, vol. 126, no. 2, 205–213, Feb. 2018.

[26] E. B. Podgorsak, *Radiation oncology physics: a handbook for teachers and students*. Vienna: International Atomic Energy Agency, Sep. 2005.

[27] I. Ciancaglioni, M. Marinelli, E. Milani, G. Prestopino, C. Verona, G. Verona-Rinati, R. Consorti, A. Petrucci and F. D. Notaristefani, 'Dosimetric characterization of a synthetic single crystal diamond detector in clinical radiation therapy small photon beams,' *Medical Physics*, vol. 39, no. 7, 4493–4501, Jul. 2012.

[28] J. M. Lárraga-Gutiérrez, P. Ballesteros-Zebadúa, M. Rodríguez-Ponce, O. A. García-Garduño and O. O. Cruz, 'Properties of a commercial PTW-60019 synthetic diamond detector for the dosimetry of small radiotherapy beams,' *Physics in Medicine and Biology*, vol. 60, no. 2, 905–924, Jan. 2015.

[29] S. Devic, N. Tomic and D. Lewis, 'Reference radiochromic film dosimetry: Review of technical aspects,' *Physica Medica*, vol. 32, no. 4, 541–556, Apr. 2016.

[30] T. Rivera, 'Thermoluminescence in medical dosimetry,' *Applied Radiation and Isotopes*, vol. 71, 30–34, Apr. 2012.

[31] B. Mijnheer, S. Beddar, J. Izewska and C. Reft, 'In vivo dosimetry in external beam radiotherapy,' *Medical Physics*, vol. 40, no. 7, Jun. 2013.

[32] S. Olsson and E. S. Bergstrand, 'Calibration of alanine dosimeters,' Faculty of Health Sciences - Department of Medicine and Care, Halsouniversitetet, Report 92a, Oct. 2001.

[33] A. S. Beddar, T. R. Mackie and F. H. Attix, 'Water-equivalent plastic scintillation detectors for high-energy beam dosimetry: II. Properties and measurements,' *Physics in Medicine and Biology*, vol. 37, no. 10, 1901–1913, Oct. 1992.

[34] Varian Medical Systems, *Eclipse Photon and Electron Algorithms Reference Guide*, Oct. 2016.

[35] PTW Freiburg GmbH. Farmer Ionization Chambers, [Online]. Available at: https://www.ptwdosimetry.com/en/products/farmer-ionization-chambers-30010-30012/ (accessed on 15/06/2019).

[36] PTW Freiburg GmbH. microDiamond Overview, [Online]. Available at: https://www.ptwdosimetry.com/en/products/microdiamond/ (accessed on 16/06/2019).

[37] V. D. Coste, P. Francescon, M. Marinelli, L. Masi, L. Paganini, M. Pimpinella, G. Prestopino, S. Russo, A. Stravato and C. Verona, 'Is the PTW 60019 microDiamond a suitable candidate for small field reference dosimetry?' *Physics in Medicine & Biology*, vol. 62, no. 17, 7036–7055, Aug. 2017.

[38] Ashland. (Apr. 2016). GAFchromic EBT3 specifications, [Online]. Available at: http://www.gafchromic.com/documents/EBT3_Specifications.pdf (accessed on 20/06/2019).

[39] Ashland. GAFchromic EBT3 Overview, [Online]. Available at: http://www.gafchromic.com/gafchromic-film/radiotherapy-films/EBT/index.asp (accessed on 20/06/2019).

[40] PTW Freiburg GmbH. PinPoint 3D Overview, [Online]. Available at: https://www.ptwdosimetry.com/en/products/pinpoint-3d-ion-chamber/ (accessed on 22/06/2019).

[41] M. Law and B. Liu, 'DICOM-RT and Its Utilization in Radiation Therapy,' *RadioGraphics*, vol. 29, no. 3, 655–667, May 2009.

[42] C. Oliveira, 'DICOM-RT standard in Radiotherapy Information Systems,' Master's thesis, Faculdade de Medicina da Universidade do Porto, Oct. 2011. [Online]. Available at: https : / / repositorio - aberto.up.pt/bitstream/10216/62158/2/TeseCeleste%20Oliveira.pdf (accessed on 23/06/2019).

[43] International Atomic Energy Agency, 'Absorbed Dose Determination in External Beam Radiotherapy,' Vienna, Technical Report Series no. 398, Jun. 2006.

[44] V. C. Borca, M. Pasquino, G. Russo, P. Grosso, D. Cante, P. Sciacero, G. Girelli, M. R. Porta and S. Tofani, 'Dosimetric characterization and use of GAFCHROMIC EBT3 film for IMRT dose verification,' *Journal of Applied Clinical Medical Physics*, vol. 14, no. 2, 158–171, Mar. 2013.

[45] R. Goebel, *DICOM Coordinate System*, BrainVoyager User's Guide. [Online]. Available at: https : / / www . brainvoyager . com / bv / doc / UsersGuide / CoordsAndTransforms/CoordinateSystems.html (accessed on 29/06/2019).

[46] L. J. Battum, M. Essers and P. R. Storchi, 'Conversion of measured percentage depth dose to tissue maximum ratio values in stereotactic radiotherapy,' *Physics in Medicine and Biology*, vol. 47, no. 18, 3289–3300, Sep. 2002.

[47] Modus Medical Devices Inc. QUASAR Thorax Phantom Specifications, [Online]. Available at: https://modusqa.com/motion/phantom/specifications (accessed on 02/07/2019).

[48] R. L. Stern, R. Heaton, M. W. Fraser, S. M. Goddu, T. H. Kirby, K. L. Lam, A. Molineu and T. C. Zhu, 'Verification of monitor unit calculations for non-IMRT clinical radiotherapy: Report of AAPM Task Group 114,' *American Association of Physicists in Medicine*, Dec. 2010.

[49] American Association of Physicists in Medicine, 'Tissue Inhomogeneity Corrections for Megavoltage Photon Beams,' AAPM Report no. 85, Aug. 2004.

[50] PTW Freiburg GmbH. T-REF Chamber, [Online]. Available at: https : / / www . ptwdosimetry . com / en / products / t - ref - chamber/ (accessed on 28/07/2019).

Appendices

A Smoothed TMR curves

A.1 TrueBeam™
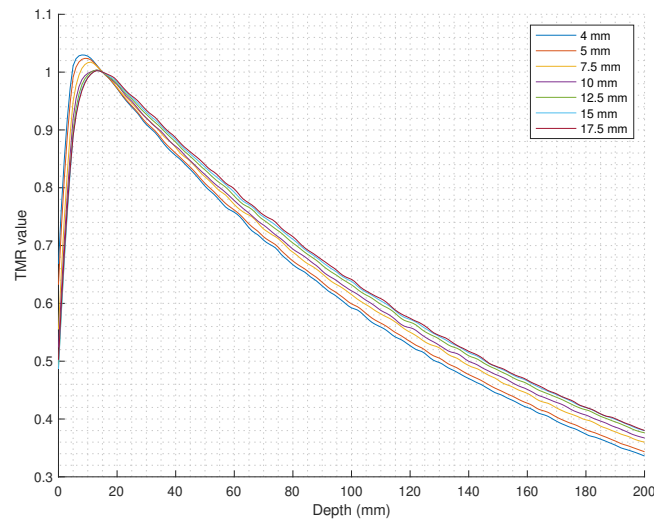
Figure 75: TrueBeam™ STx smoothed TMR with a local regression method using weighted linear least squares and a 2nd degree polynomial model for 6 FFF energy.
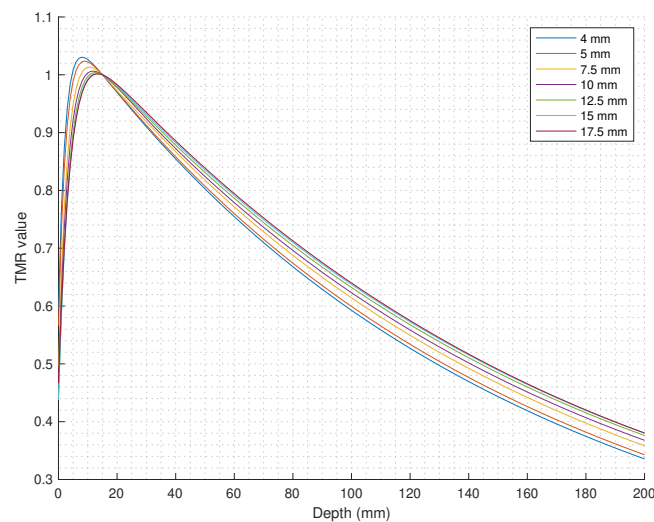
Figure 76: TrueBeam™ STx TMR fitted into a two-term exponential model for 6 FFF energy.
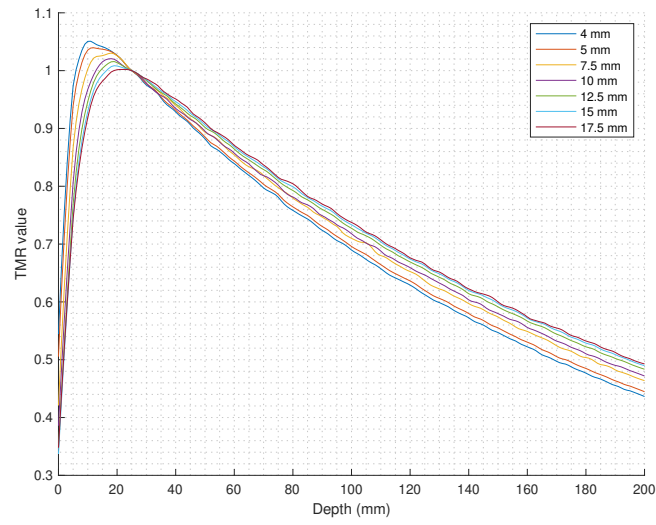
Figure 77: TrueBeam™ STx smoothed TMR with a local regression method using weighted linear least squares and a 2nd degree polynomial model for 10 FFF energy.
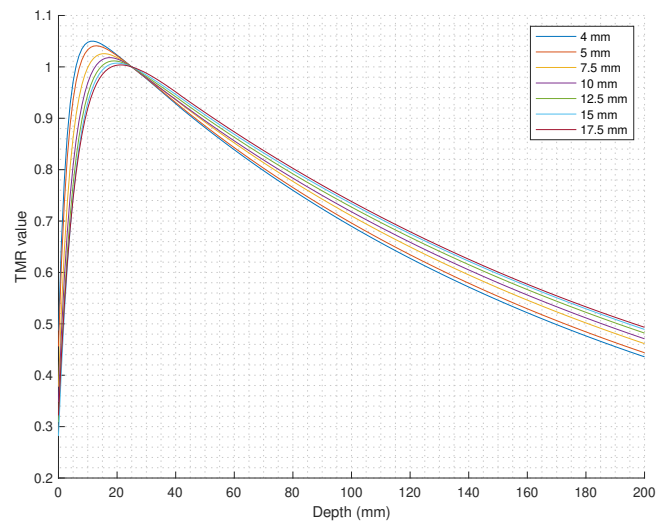
Figure 78: TrueBeam™ STx smoothed TMR fitted into a two-term exponential model for 10 FFF energy.

A.2 Novalis Tx™
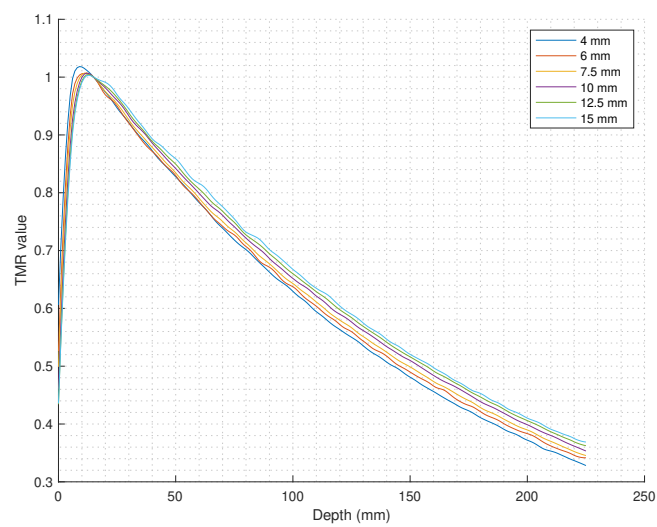
Figure 79: Novalis Tx™ smoothed TMR with a local regression method using weighted linear least squares and a 2nd degree polynomial model for 6X SRS energy.
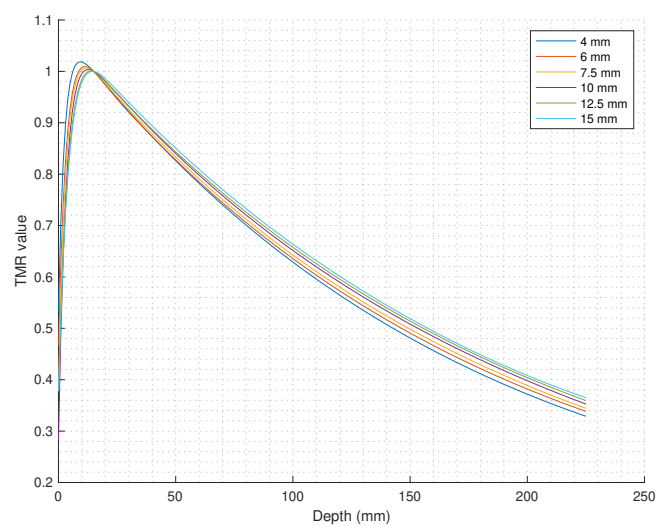
Figure 80: Novalis Tx™ smoothed TMR fitted into a two-term exponential model for 6X SRS energy.

B Beam parameters used in algorithm validation

B.1 Without heterogeneity correction

Table 27: Static field parameters used for MU calculation without heterogeneity correction validation in TrueBeam™ STx LINAC. All fields are normalized to a isocenter dose of 8 Gy.

Energy	Cone Size (mm)	Gantry Rtn. (º)	Couch Rtn. (º)	TPS MU
6 FFF	17.5	0	0	1079.2
6 FFF	17.5	90	0	1212.7
6 FFF	17.5	210	0	1023.1
6 FFF	17.5	0	20	1074.2
6 FFF	17.5	80	90	1266.1
6 FFF	17.5	210	340	1040.5
6 FFF	10	0	0	1197.9
6 FFF	10	90	0	1353.1
6 FFF	10	210	0	1133.2
6 FFF	10	0	270	1197.0
6 FFF	10	90	45	1502.0
6 FFF	10	210	320	1197.0
6 FFF	5	0	0	1487.3
6 FFF	5	90	0	1689.6
6 FFF	5	210	0	1403.6
6 FFF	5	0	45	1487.3
6 FFF	5	90	30	1843.0
6 FFF	5	210	310	1513.4
10 FFF	17.5	0	0	995.3
10 FFF	17.5	90	0	1089.5
10 FFF	17.5	210	0	954.1
10 FFF	15	0	0	1030.7
10 FFF	15	90	0	1129.9
10 FFF	15	210	0	987.4
10 FFF	12.5	0	0	1076.9

Table 27: Static field parameters used for MU calculation without heterogeneity correction validation in TrueBeam™ STx LINAC. All fields are normalized to a isocenter dose of 8 Gy.

Energy	Cone Size (mm)	Gantry Rtn. (º)	Couch Rtn. (º)	TPS MU
10 FFF	12.5	90	0	1182.7
10 FFF	12.5	210	0	1030.9
10 FFF	10	0	0	1162.1
10 FFF	10	90	0	1285.5
10 FFF	10	210	0	1116.1
10 FFF	7.5	0	0	1294.3
10 FFF	7.5	90	0	1429.3
10 FFF	7.5	210	0	1236.0
10 FFF	5	0	0	1576.0
10 FFF	5	90	0	1749.3
10 FFF	5	210	0	1501.9
10 FFF	4	0	0	1845.4
10 FFF	4	90	0	2052.8
10 FFF	4	210	0	1757.0

Table 28: Arc parameters used for MU calculation without heterogeneity correction validation in TrueBeam™ STx LINAC. All arcs are normalized to a isocenter dose of 8 Gy, calculated with 1º gantry resolution.

Energy	Cone Size (mm)	Gantry Rtn. (º)	Couch Rtn. (º)	TPS MU
6 FFF	17.5	11 → 124	20	1225.3
6 FFF	17.5	232 → 332	340	1025.4
6 FFF	17.5	112 → 0	90	1200.7
6 FFF	15	300 → 120	30	902.6
6 FFF	15	107 → 320	85	884.0
6 FFF	15	181 → 67.5	320	964.3
6 FFF	12.5	0 → 120	30	1241.2
6 FFF	12.5	300 → 70	45	1213.0
6 FFF	12.5	181 → 340	340	978.9
6 FFF	10	11 → 124	20	1376.1
6 FFF	10	232 → 332	340	1142.7

Table 28: Arc parameters used for MU calculation without heterogeneity correction validation in TrueBeam™ STx LINAC. All arcs are normalized to a isocenter dose of 8 Gy, calculated with 1º gantry resolution.

Energy	Cone Size (mm)	Gantry Rtn. (º)	Couch Rtn. (º)	TPS MU
6 FFF	10	112 → 0	90	1347.2
6 FFF	7.5	0 → 120	90	1205.1
6 FFF	7.5	300 → 70	0	1406.4
6 FFF	7.5	181 → 340	270	1146.2
6 FFF	5	300 → 120	30	1194.7
6 FFF	5	107 → 320	85	1166.3
6 FFF	5	181 → 67.5	320	1286.8
6 FFF	4	0 → 120	90	1580.1
6 FFF	4	300 → 70	0	1856.6
6 FFF	4	181 → 340	270	1500.1
10 FFF	17.5	11 → 124	20	1101.4
10 FFF	17.5	232 → 332	340	958.5
10 FFF	17.5	112 → 0	90	1084.3
10 FFF	15	300 → 120	30	899.4
10 FFF	15	107 → 320	85	900.0
10 FFF	15	181 → 67.5	320	935.3
10 FFF	12.5	0 → 120	30	1157.2
10 FFF	12.5	300 → 70	45	1136.6
10 FFF	12.5	181 → 340	340	962.3
10 FFF	10	11 → 124	20	1303.3
10 FFF	10	232 → 332	340	1124.0
10 FFF	10	112 → 0	90	1281.7
10 FFF	7.5	0 → 120	90	1230.5
10 FFF	7.5	300 → 70	0	1393.4
10 FFF	7.5	181 → 340	270	1182.0
10 FFF	5	300 → 120	30	1322.0
10 FFF	5	107 → 320	85	1297.8
10 FFF	5	181 → 67.5	320	1401.6
10 FFF	4	0 → 120	90	1752.4

Table 28: Arc parameters used for MU calculation without heterogeneity correction validation in TrueBeam™ STx LINAC. All arcs are normalized to a isocenter dose of 8 Gy, calculated with 1º gantry resolution.

Energy	Cone Size (mm)	Gantry Rtn. (º)	Couch Rtn. (º)	TPS MU
10 FFF	4	300 → 70	0	2003.3
10 FFF	4	181 → 340	270	1677.9

Table 29: Static field parameters used for MU calculation without heterogeneity correction validation in Novalis Tx™ LINAC. All fields are normalized to a isocenter dose of 8 Gy.

Energy	Cone Size (mm)	Gantry Rtn. (º)	Couch Rtn. (º)	TPS MU
6X SRS	15	0	0	1093.0
6X SRS	15	90	0	1216.3
6X SRS	15	210	0	1041.0
6X SRS	15	0	20	1089.5
6X SRS	15	80	90	1266.6
6X SRS	15	210	340	1058.2
6X SRS	10	0	0	117.5
6X SRS	10	90	0	1315.3
6X SRS	10	210	0	1120.8
6X SRS	10	0	20	1172.7
6X SRS	10	80	90	1376.1
6X SRS	10	210	340	1143.7
6X SRS	6	0	0	1379.9
6X SRS	6	90	0	1546.4
6X SRS	6	210	0	1310.3
6X SRS	6	0	20	1379.9
6X SRS	6	80	90	1620.1
6X SRS	6	210	340	1337.7

Table 30: Arc parameters used for MU calculation without heterogeneity correction validation in Novalis Tx™ LINAC. All arcs are normalized to a isocenter dose of 8 Gy, calculated with 1º gantry resolution.

Energy	Cone Size (mm)	Gantry Rtn. (º)	Couch Rtn. (º)	TPS MU
6X SRS	15	11-124	20	897.0
6X SRS	15	232-332	340	1002.1

Table 30: Arc parameters used for MU calculation without heterogeneity correction validation in Novalis Tx™ LINAC. All arcs are normalized to a isocenter dose of 8 Gy, calculated with 1º gantry resolution.

Energy	Cone Size (mm)	Gantry Rtn. (º)	Couch Rtn. (º)	TPS MU
6X SRS	15	112-0	90	889.0
6X SRS	12.5	11-124	20	1334.5
6X SRS	12.5	232-332	340	992.5
6X SRS	12.5	112-0	90	1074.2
6X SRS	10	11-124	20	1334.5
6X SRS	10	232-332	340	1129.8
6X SRS	10	112-0	90	1310.3
6X SRS	7.5	11-124	20	1426.7
6X SRS	7.5	232-332	340	1120.0
6X SRS	7.5	112-0	90	1215.9
6X SRS	6	11-124	20	1115.6
6X SRS	6	232-332	340	1261.4
6X SRS	6	112-0	90	1100.1

B.2   With heterogeneity correction

Table 31: Beam parameters used for dose calculation with heterogeneity correction validation in TrueBeam™ STx LINAC. All fields are normalized to a isocenter dose of 8 Gy. Arcs are calculated with 1º gantry resolution.

Energy	Cone Size (mm)	Gantry Rtn. (º)	Couch Rtn. (º)	TPS MU
6 FFF	17.5	90	0	1739.0
6 FFF	17.5	180	0	1332.8
6 FFF	17.5	0 → 180	0	1522.1
6 FFF	15	90	0	1791.0
6 FFF	15	180	0	1367.0
6 FFF	15	0 → 180	0	1564.1
6 FFF	12.5	90	0	1848.6
6 FFF	12.5	180	0	1406.1
6 FFF	12.5	0 → 180	0	1611.1
6 FFF	10	90	0	1966.3
6 FFF	10	180	0	1494.3
6 FFF	10	0 → 180	0	1710.4
10 FFF	17.5	90	0	1437.9
10 FFF	17.5	180	0	1170.5
10 FFF	17.5	0 → 180	0	1297.8
10 FFF	15	90	0	1499.2
10 FFF	15	180	0	1216.0
10 FFF	15	0 → 180	0	1350.4
10 FFF	12.5	90	0	1579.4
10 FFF	12.5	180	0	1275.1
10 FFF	12.5	0 → 180	0	1419.1
10 FFF	10	90	0	1730.4
10 FFF	10	180	0	1392.1
10 FFF	10	0 → 180	0	1553.1

Table 32: Beam parameters used for dose calculation with heterogeneity correction validation in Novalis Tx™ LINAC. All fields are normalized to a isocenter dose of 8 Gy. Arcs are calculated with 1º gantry resolution.

Energy	Cone Size (mm)	Gantry Rtn. (º)	Couch Rtn. (º)	TPS MU
6X SRS	15	90	0	1688.7
6X SRS	15	180	0	1327.7
6X SRS	15	0 → 180	0	1521.3
6X SRS	12.5	90	0	1754.5
6X SRS	12.5	180	0	1374.9
6X SRS	12.5	0 → 180	0	1553.3
6X SRS	10	90	0	1843.8
6X SRS	10	180	0	1438.9
6X SRS	10	0 → 180	0	1649.4

C   Algorithm validation results

C.1   Without heterogeneity correction

Table 33: Results of MU calculation without heterogeneity correction validation in TrueBeam™ STx LINAC using static fields.

Energy	Cone Size (mm)	Gantry Rtn. (º)	Couch Rtn. (º)	TPS MU	Predicted MU	Difference (%)
6 FFF	17.5	0	0	1079.2	1081.9	+0.25
6 FFF	17.5	90	0	1212.7	1231.4	+1.54
6 FFF	17.5	210	0	1023.1	1029.1	+0.59
6 FFF	17.5	0	20	1074.2	1081.9	+0.72
6 FFF	17.5	80	90	1266.1	1292.3	+2.07
6 FFF	17.5	210	340	1040.5	1046.6	+0.59
6 FFF	10	0	0	1197.9	1193.8	-0.34
6 FFF	10	90	0	1353.1	1362.1	+0.67
6 FFF	10	210	0	1133.2	1133.0	-0.02
6 FFF	10	0	270	1197.0	1193.8	-0.27
6 FFF	10	90	45	1502.0	1510.6	+0.57
6 FFF	10	210	320	1197.0	1200.6	+0.30
6 FFF	5	0	0	1487.3	1499.4	+0.81
6 FFF	5	90	0	1689.6	1722.7	+1.96
6 FFF	5	210	0	1403.6	1418.5	+1.06
6 FFF	5	0	45	1487.3	1499.4	+0.81
6 FFF	5	90	30	1843.0	1874.6	+1.71
6 FFF	5	210	310	1513.4	1536.8	+1.55
10 FFF	17.5	0	0	995.3	993.9	-0.14
10 FFF	17.5	90	0	1089.5	1098.3	+0.81
10 FFF	17.5	210	0	954.1	957.4	+0.35
10 FFF	15	0	0	1030.7	1033.7	+0.29
10 FFF	15	90	0	1129.9	1142.6	+1.12
10 FFF	15	210	0	987.4	994.2	+0.69
10 FFF	12.5	0	0	1076.9	1085.0	+0.75

Table 33: Results of MU calculation without heterogeneity correction validation in TrueBeam™ STx LINAC using static fields.

Energy	Cone Size (mm)	Gantry Rtn. (º)	Couch Rtn. (º)	TPS MU	Predicted MU	Difference (%)
10 FFF	12.5	90	0	1182.7	1201.3	+1.57
10 FFF	12.5	210	0	1030.9	1042.2	+1.10
10 FFF	10	0	0	1162.1	1155.9	-0.53
10 FFF	10	90	0	1285.5	1286.2	+0.05
10 FFF	10	210	0	1116.1	1114.3	-0.16
10 FFF	7.5	0	0	1294.3	1294.3	0.00
10 FFF	7.5	90	0	1429.3	1440.0	+0.75
10 FFF	7.5	210	0	1236.0	1240.7	+0.38
10 FFF	5	0	0	1576.0	1586.7	+0.68
10 FFF	5	90	0	1749.3	1775.8	+1.51
10 FFF	5	210	0	1501.9	1517.4	+1.03
10 FFF	4	0	0	1845.4	1822.6	-1.24
10 FFF	4	90	0	2052.8	2054.2	+0.07
10 FFF	4	210	0	1757.0	1739.7	-0.98

Table 34: Results of MU calculation without heterogeneity correction validation in TrueBeam™ STx LINAC using arcs.

Energy	Cone Size (mm)	Gantry Rtn. (º)	Couch Rtn. (º)	TPS MU	Predicted MU	Difference (%)
6 FFF	17.5	11-124	20	1225.3	1248.3	+1.88
6 FFF	17.5	232-332	340	1025.4	1033.7	+0.81
6 FFF	17.5	112-0	90	1200.7	1220.8	+1.67
6 FFF	15	300-120	30	902.6	910.2	+0.84
6 FFF	15	107-320	85	884.0	891.9	+0.89
6 FFF	15	181-67.5	320	964.3	972.4	+0.84
6 FFF	12.5	0-120	30	1241.2	1263.1	+1.76
6 FFF	12.5	300-70	45	1213.0	1230.7	+1.46
6 FFF	12.5	181-340	340	978.9	988.9	+1.03
6 FFF	10	11-124	20	1376.1	1381.6	+0.40

Table 34: Results of MU calculation without heterogeneity correction validation in TrueBeam™ STx LINAC using arcs.

Energy	Cone Size (mm)	Gantry Rtn. (º)	Couch Rtn. (º)	TPS MU	Predicted MU	Difference (%)
6 FFF	10	232-332	340	1142.7	1138.2	-0.39
6 FFF	10	112-0	90	1347.2	1350.5	+0.24
6 FFF	7.5	0-120	90	1205.1	1206.8	+0.14
6 FFF	7.5	300-70	0	1406.4	1411.4	+0.36
6 FFF	7.5	181-340	270	1146.2	1149.0	+0.24
6 FFF	5	300-120	30	1194.7	1208.3	+1.14
6 FFF	5	107-320	85	1166.3	1180.5	+1.22
6 FFF	5	181-67.5	320	1286.8	1300.0	+1.03
6 FFF	4	0-120	90	1580.1	1563.2	-1.07
6 FFF	4	300-70	0	1856.6	1850.7	+0.32
6 FFF	4	181-340	270	1500.1	1482.3	-1.19
10 FFF	17.5	11-124	20	1101.4	1110.2	+0.80
10 FFF	17.5	232-332	340	958.5	960.7	+0.23
10 FFF	17.5	112-0	90	1084.3	1091.2	+0.64
10 FFF	15	300-120	30	899.4	903.8	+0.49
10 FFF	15	107-320	85	900.0	894.8	-0.58
10 FFF	15	181-67.5	320	935.3	939.7	+0.47
10 FFF	12.5	0-120	30	1157.2	1171.9	+1.27
10 FFF	12.5	300-70	45	1136.6	1148.6	+1.06
10 FFF	12.5	181-340	340	962.3	970.1	+0.81
10 FFF	10	11-124	20	1303.3	1301.4	-0.15
10 FFF	10	232-332	340	1124.0	1118.3	-0.51
10 FFF	10	112-0	90	1281.7	1278.5	-0.25
10 FFF	7.5	0-120	90	1230.5	1230.8	+0.02
10 FFF	7.5	300-70	0	1393.4	1394.7	+0.09
10 FFF	7.5	181-340	270	1182.0	1183.8	+0.15
10 FFF	5	300-120	30	1322.0	1339.6	+1.33
10 FFF	5	107-320	85	1297.8	1316.2	+1.43

Table 34: Results of MU calculation without heterogeneity correction validation in TrueBeam™ STx LINAC using arcs.

Energy	Cone Size (mm)	Gantry Rtn. (º)	Couch Rtn. (º)	TPS MU	Predicted MU	Difference (%)
10 FFF	5	181-67.5	320	1401.6	1417.7	+1.15
10 FFF	4	0-120	90	1752.4	1723.2	-1.67
10 FFF	4	300-70	0	2003.3	1979.0	-1.21
10 FFF	4	181-340	270	1677.9	1650.4	-1.64

Table 35: Results of MU calculation without heterogeneity correction validation in Novalis Tx™ LINAC using static fields.

Energy	Cone Size (mm)	Gantry Rtn. (º)	Couch Rtn. (º)	TPS MU	Predicted MU	Difference (%)
6X SRS	15	0	0	1093.0	1095.8	+0.26
6X SRS	15	90	0	1216.3	1231.7	+1.27
6X SRS	15	210	0	1041.0	1048.9	+0.76
6X SRS	15	0	20	1089.5	1095.8	+0.58
6X SRS	15	80	90	1266.6	1287.8	+1.67
6X SRS	15	210	340	1058.2	1069.5	+1.07
6X SRS	10	0	0	117.5	1179.8	+0.62
6X SRS	10	90	0	1315.3	1331.9	+1.26
6X SRS	10	210	0	1120.8	1131.4	+0.95
6X SRS	10	0	20	1172.7	1179.8	+0.61
6X SRS	10	80	90	1376.1	1395.2	+1.39
6X SRS	10	210	340	1143.7	1149.2	+0.48
6X SRS	6	0	0	1379.9	1390.1	+0.74
6X SRS	6	90	0	1546.4	1570.4	+1.55
6X SRS	6	210	0	1310.3	1324.1	+1.05
6X SRS	6	0	20	1379.9	1390.1	+0.74
6X SRS	6	80	90	1620.1	1641.8	+1.34
6X SRS	6	210	340	1337.7	1345.7	+0.60

Table 36: Results of MU calculation without heterogeneity correction validation in Novalis Tx™ LINAC using arcs.

Energy	Cone Size (mm)	Gantry Rtn. (º)	Couch Rtn. (º)	TPS MU	Predicted MU	Difference (%)
6X SRS	15	11-124	20	897.0	908.5	+1.28
6X SRS	15	232-332	340	1002.1	1011.2	+0.91
6X SRS	15	112-0	90	889.0	899.4	+1.17
6X SRS	12.5	11-124	20	1334.5	1270.5	+1.35
6X SRS	12.5	232-332	340	992.5	999.5	+0.71
6X SRS	12.5	112-0	90	1074.2	1083.3	+0.85
6X SRS	10	11-124	20	1334.5	1350.4	+1.19
6X SRS	10	232-332	340	1129.8	1136.1	+0.56
6X SRS	10	112-0	90	1310.3	1323.3	+0.99
6X SRS	7.5	11-124	20	1426.7	1432.5	+0.41
6X SRS	7.5	232-332	340	1120.0	1119.4	-0.05
6X SRS	7.5	112-0	90	1215.9	1216.9	+0.08
6X SRS	6	11-124	20	1115.6	1125.1	+0.85
6X SRS	6	232-332	340	1261.4	1268.1	+0.53
6X SRS	6	112-0	90	1100.1	1108.6	+0.77

C.2   With heterogeneity correction

Table 37: Results of dose calculation with heterogeneity correction validation in TrueBeam™ STx LINAC.

Energy	Cone Size (mm)	Gantry Rtn. (º)	TPS MU	Predicted Dose (Gy)	Absorbed Dose (Gy)	Difference (%)
6 FFF	17.5	90	1739.0	10.105	10.268	-1.59
6 FFF	17.5	180	1332.8	7.304	7.304	0.00
6 FFF	17.5	0-180	1522.1	8.063	7.928	+1.70
6 FFF	15	90	1791.0	10.127	10.364	-2.29
6 FFF	15	180	1367.0	7.297	7.327	-0.41
6 FFF	15	0-180	1564.1	8.065	7.963	+1.28
6 FFF	12.5	90	1848.6	10.135	10.383	-2.39
6 FFF	12.5	180	1406.1	7.264	7.302	-0.52
6 FFF	12.5	0-180	1611.1	8.040	7.947	+1.17
6 FFF	10	90	1966.3	10.304	10.361	-0.55
6 FFF	10	180	1494.3	7.374	7.396	-0.30
6 FFF	10	0-180	1710.4	8.158	7.997	+2.01
10 FFF	17.5	90	1437.9	9.602	9.937	-3.37
10 FFF	17.5	180	1170.5	7.470	7.628	-2.07
10 FFF	17.5	0-180	1297.8	8.012	8.135	-1.51
10 FFF	15	90	1499.2	9.618	9.989	-3.71
10 FFF	15	180	1216.0	7.453	7.624	-2.24
10 FFF	15	0-180	1350.4	8.053	8.140	-1.07
10 FFF	12.5	90	1579.4	9.618	10.011	-3.93
10 FFF	12.5	180	1275.1	7.417	7.590	-2.28
10 FFF	12.5	0-180	1419.1	8.027	8.112	-1.05
10 FFF	10	90	1730.4	9.824	10.064	-2.38
10 FFF	10	180	1392.1	7.692	7.692	-1.92
10 FFF	10	0-180	1553.1	8.180	8.177	+0.04

Table 38: Results of dose calculation with heterogeneity correction validation in Novalis Tx™ LINAC.

Energy	Cone Size (mm)	Gantry Rtn. (º)	TPS MU	Predicted Dose (Gy)	Absorbed Dose (Gy)	Difference (%)
6X SRS	15	90	1688.7	9.857	9.743	+1.17
6X SRS	15	180	1327.7	7.379	7.079	+4.24
6X SRS	15	0-180	1521.3	8.028	7.734	+3.80
6X SRS	12.5	90	1754.5	9.824	9.819	+0.05
6X SRS	12.5	180	1374.9	7.360	7.109	+3.53
6X SRS	12.5	0-180	1553.3	8.046	7.756	+3.74
6X SRS	10	90	1843.8	9.980	9.821	+1.62
6X SRS	10	180	1438.9	7.345	7.095	+3.52
6X SRS	10	0-180	1649.4	8.071	7.734	+4.36

D   Patient plans MU verification

D.1   TrueBeam™ STx patient plans
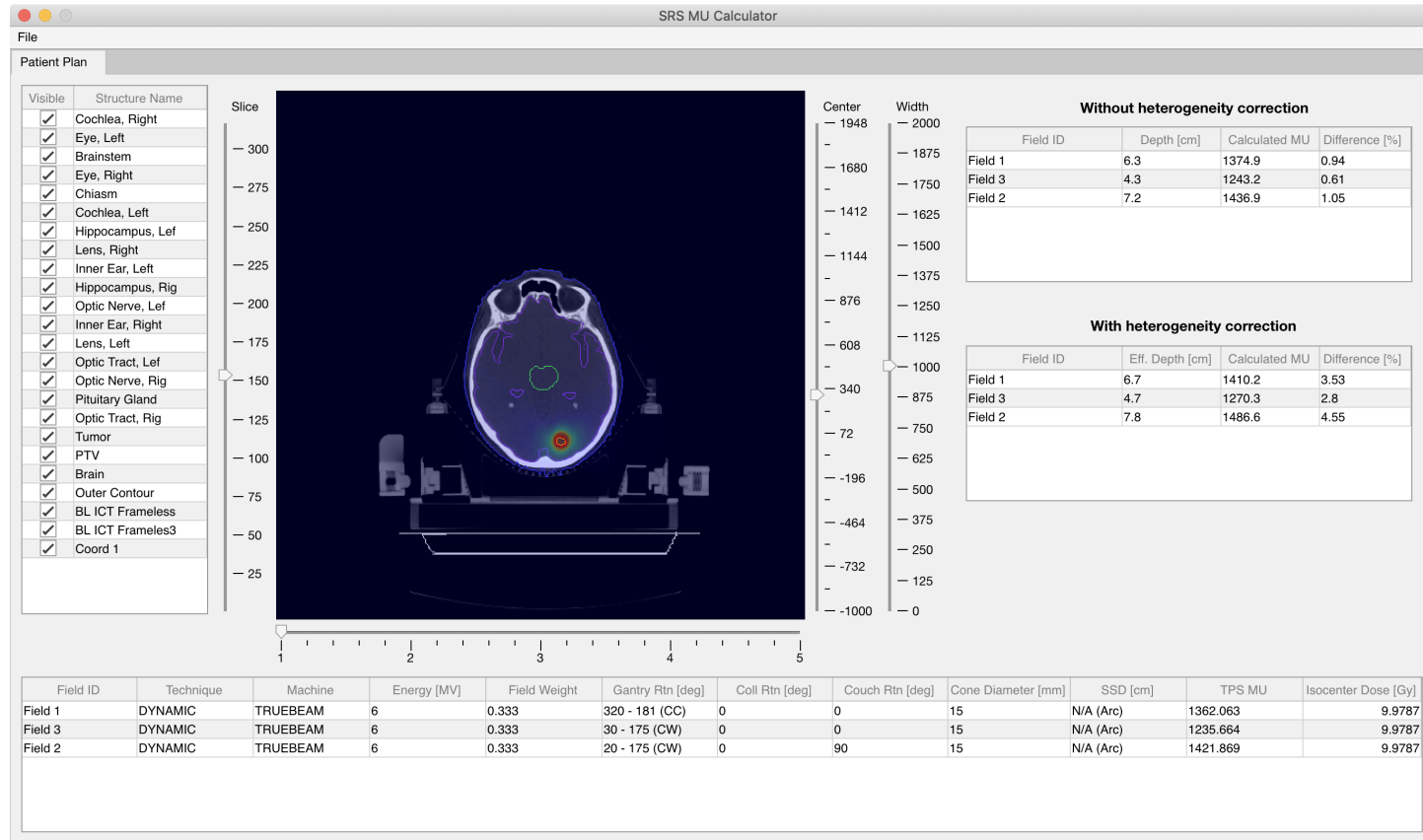
Figure 81: Patient ID 1.
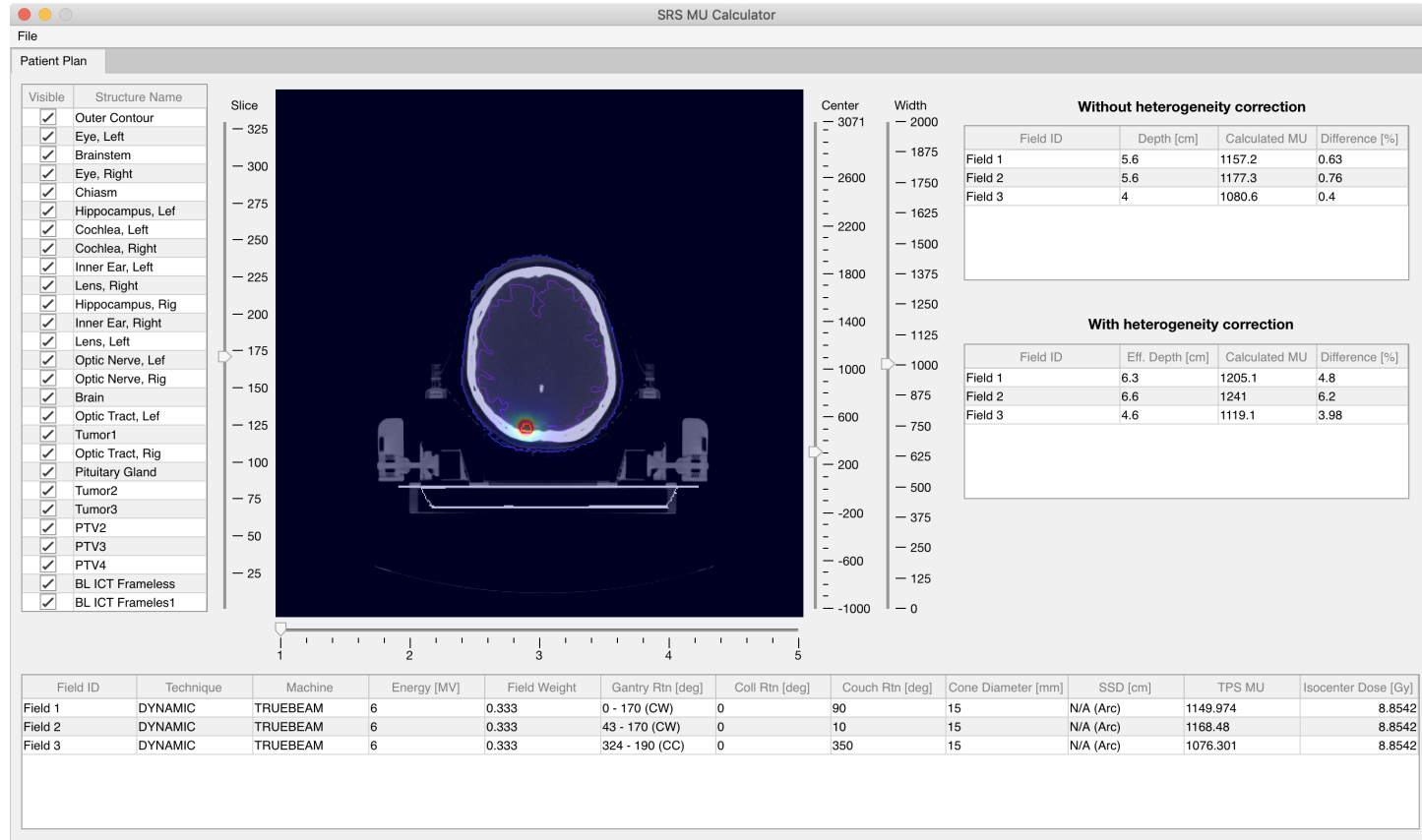
Figure 82: Patient ID 2.
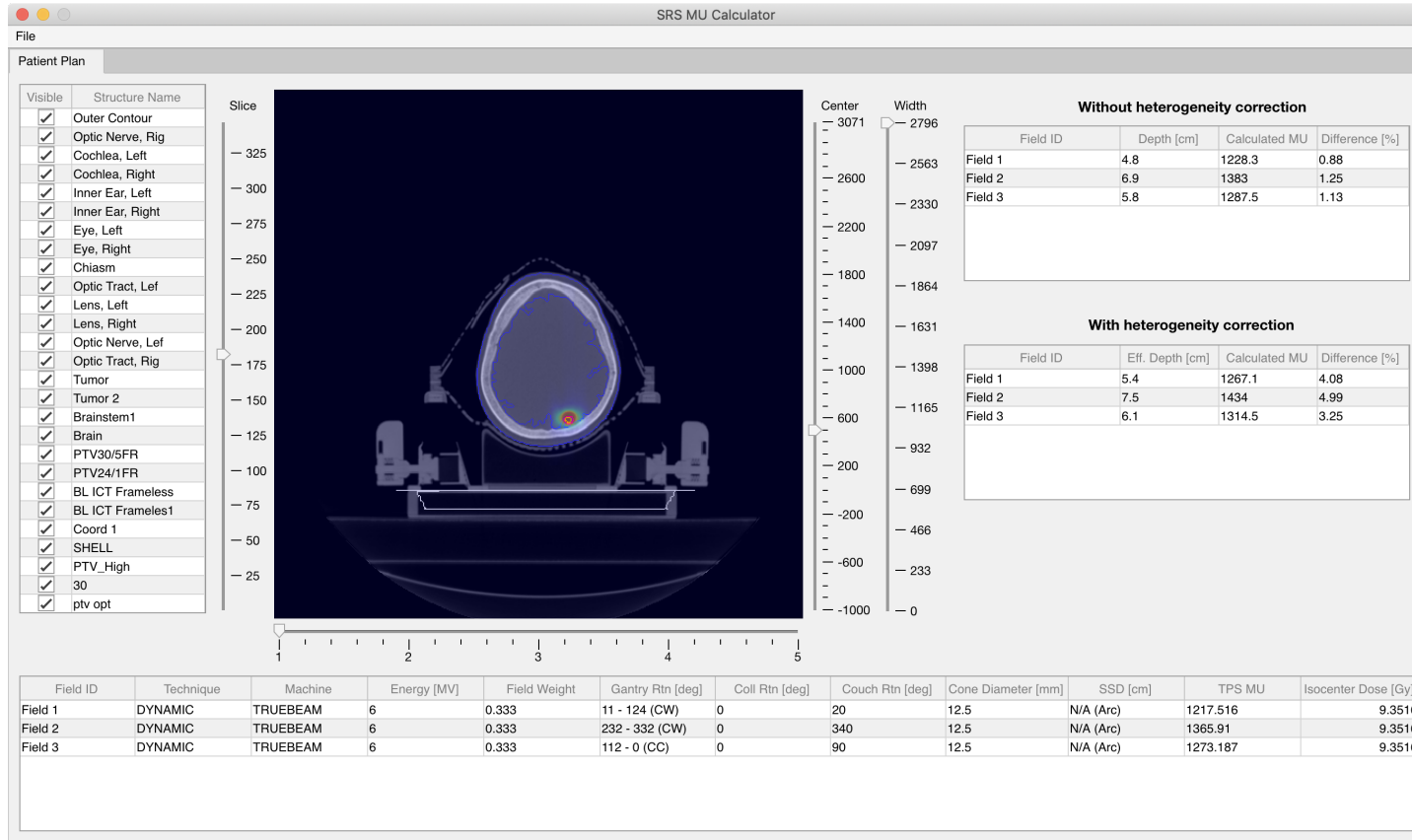
Figure 83: Patient ID 3.
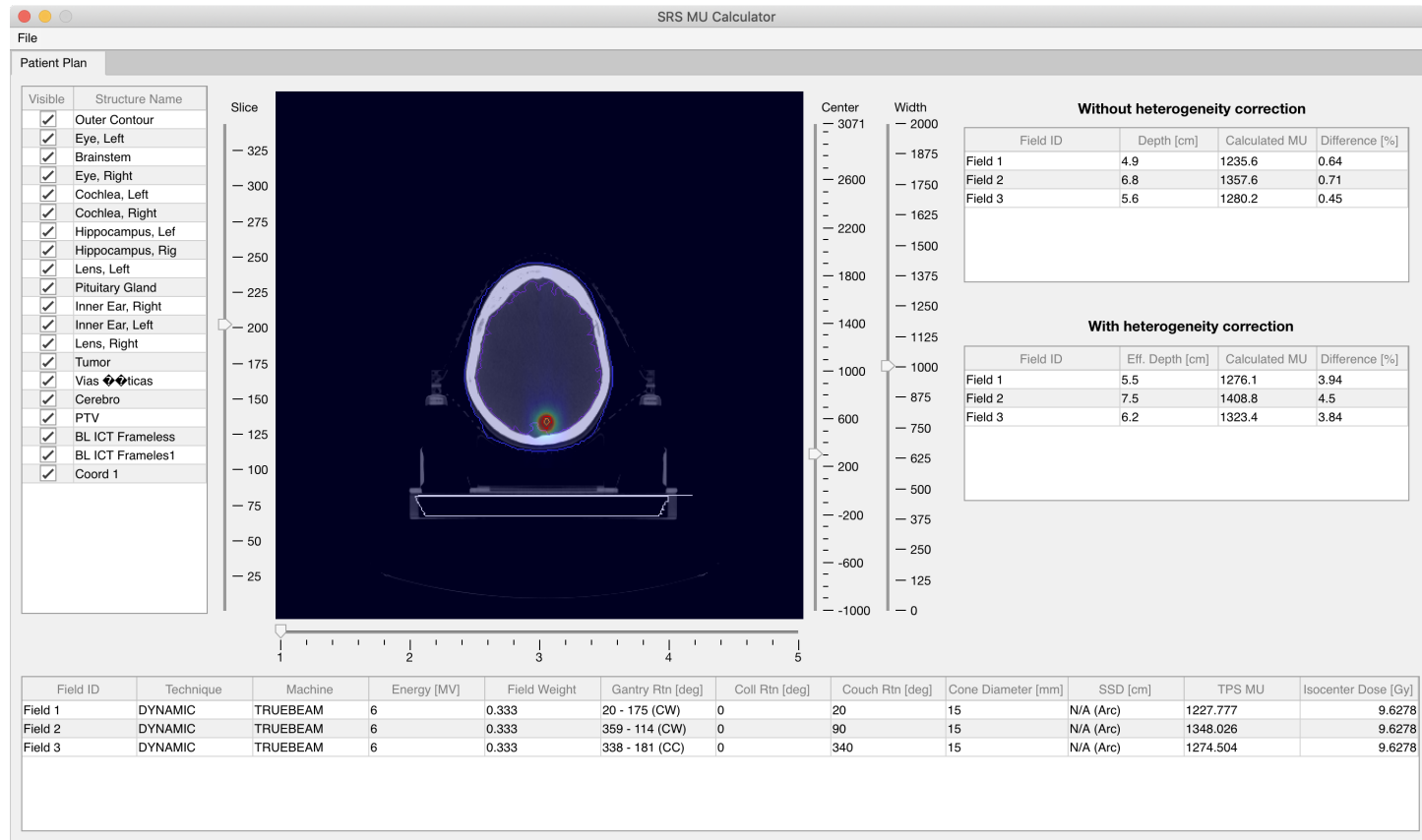
Figure 84: Patient ID 4.
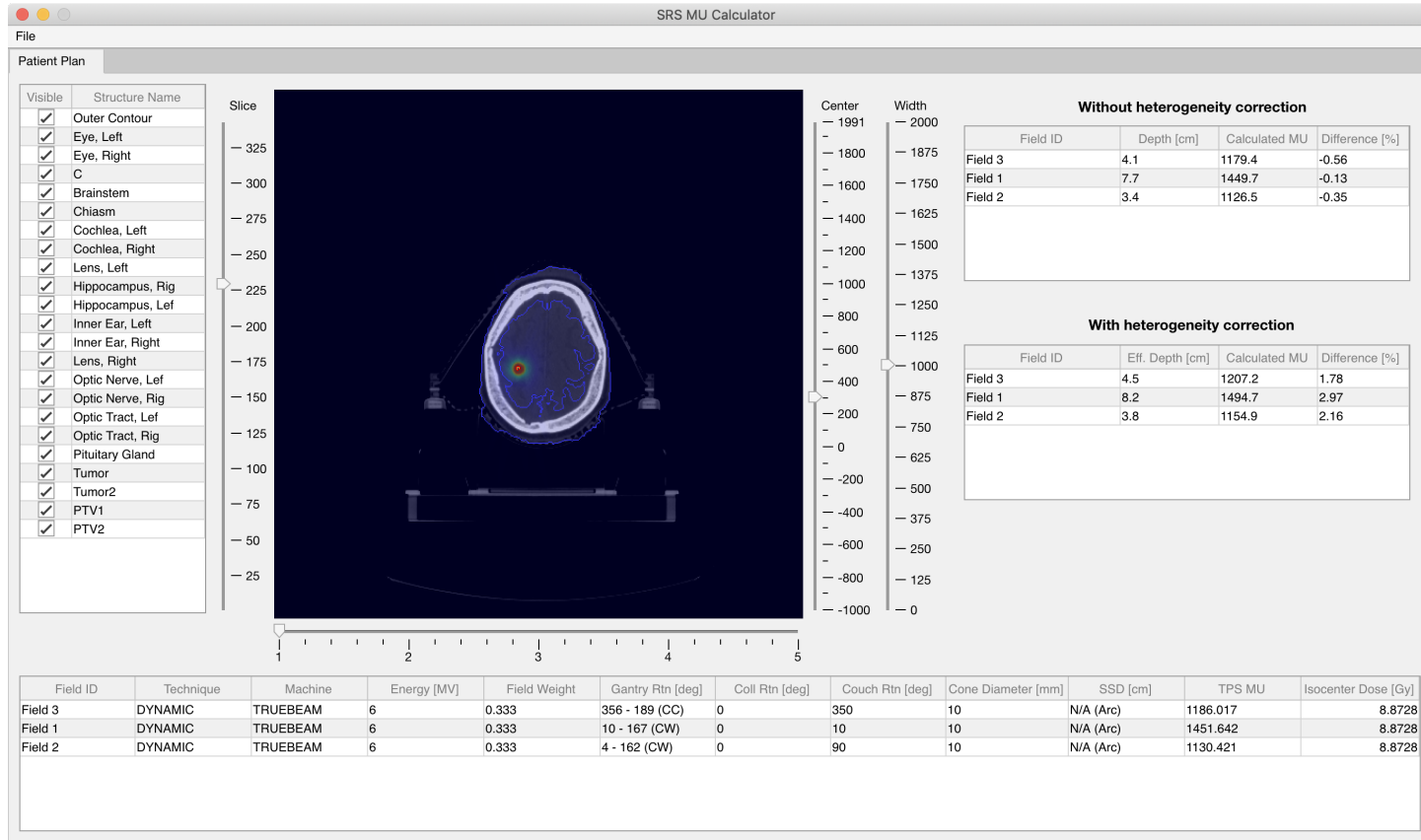
Figure 85: Patient ID 5.
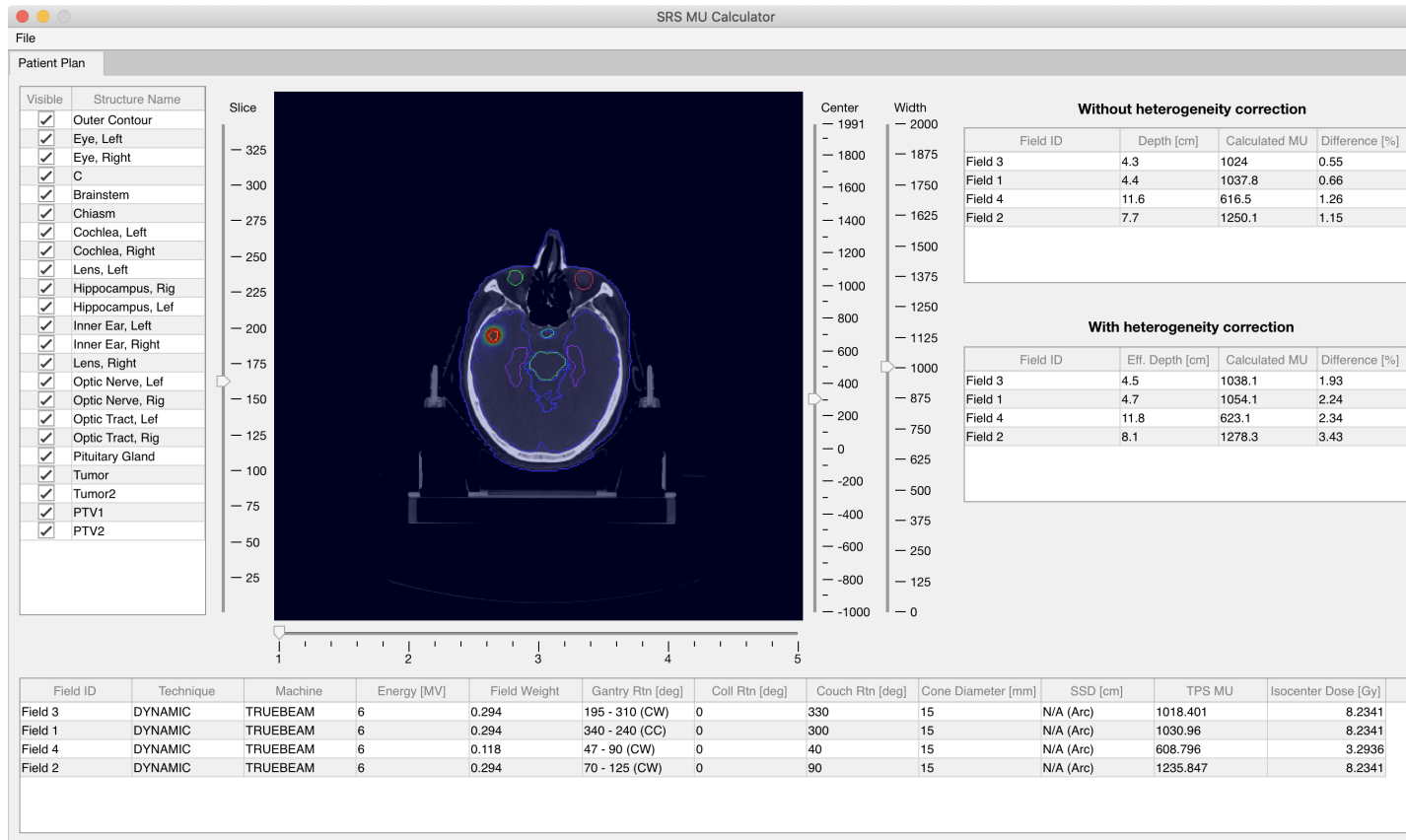
Figure 86: Patient ID 6.
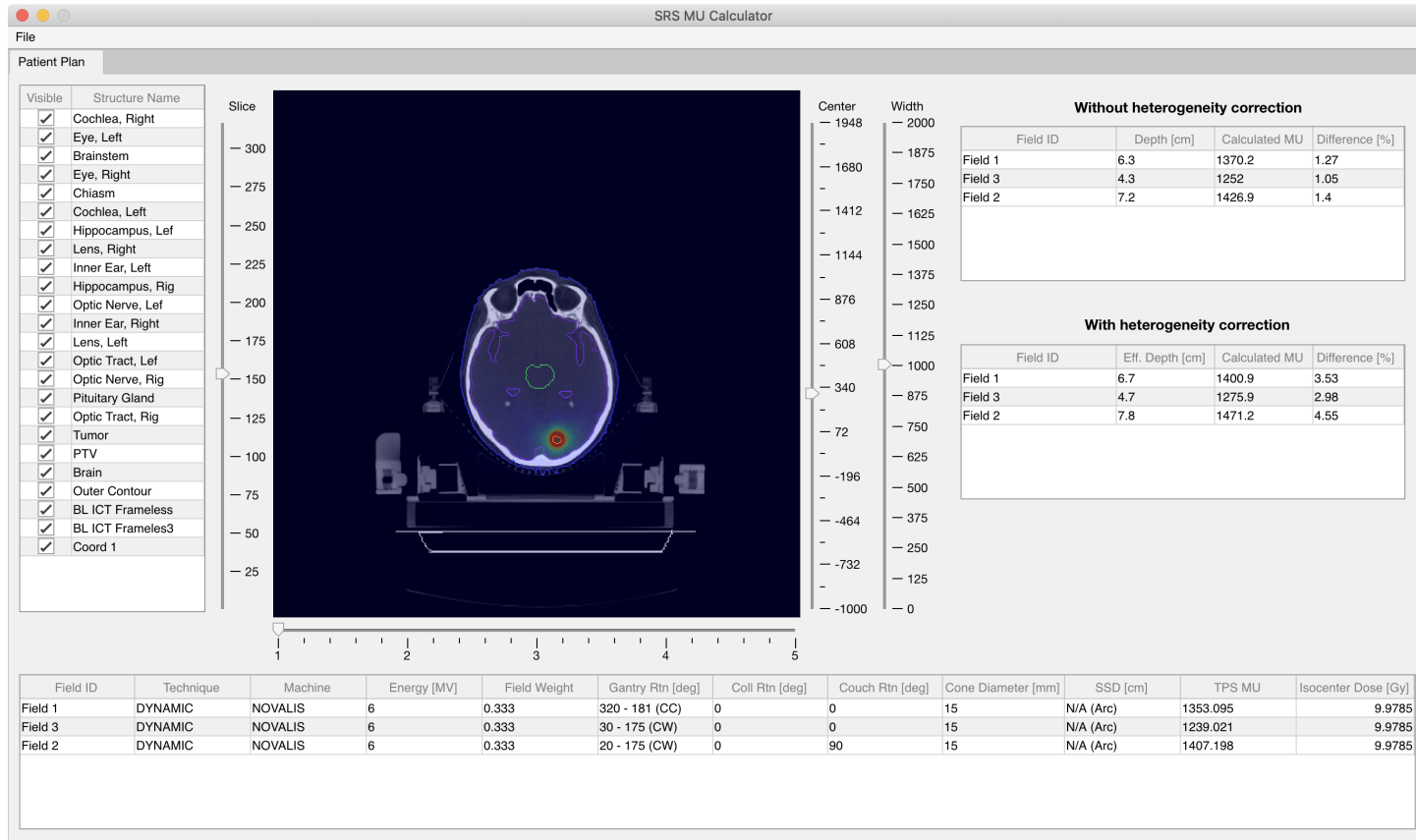
D.2 Novalis Tx™ patient plans
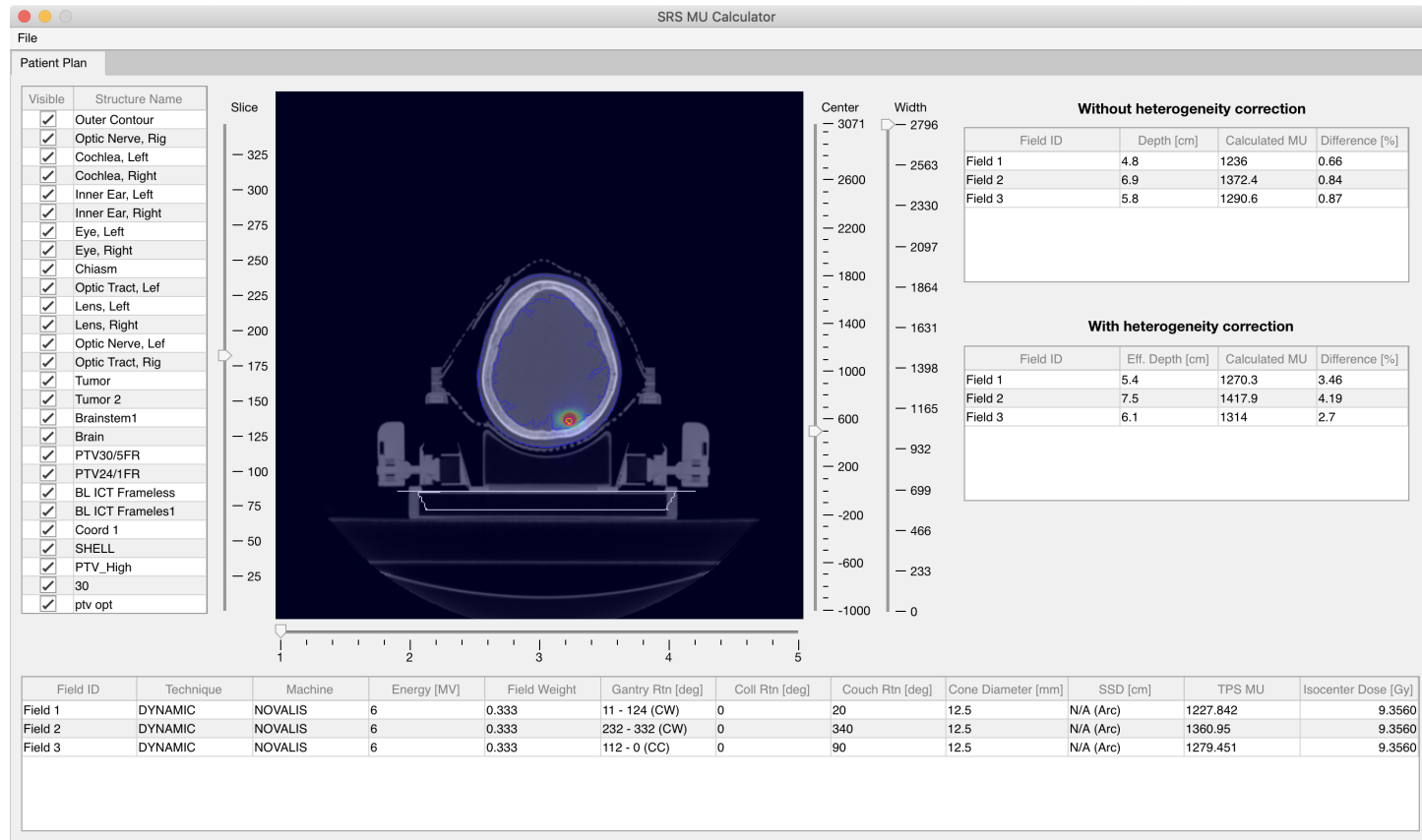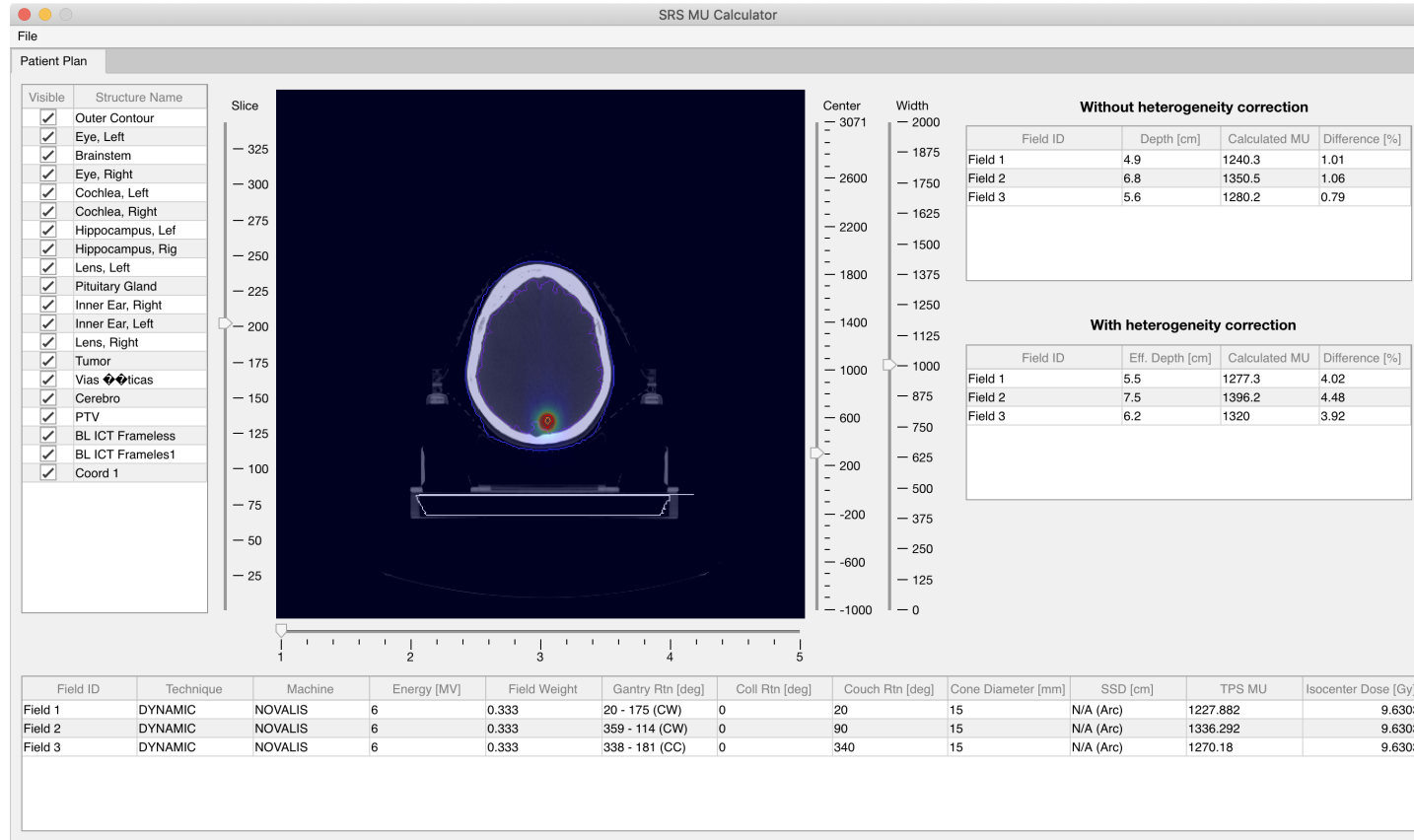
Figure 87: Patient ID 7.
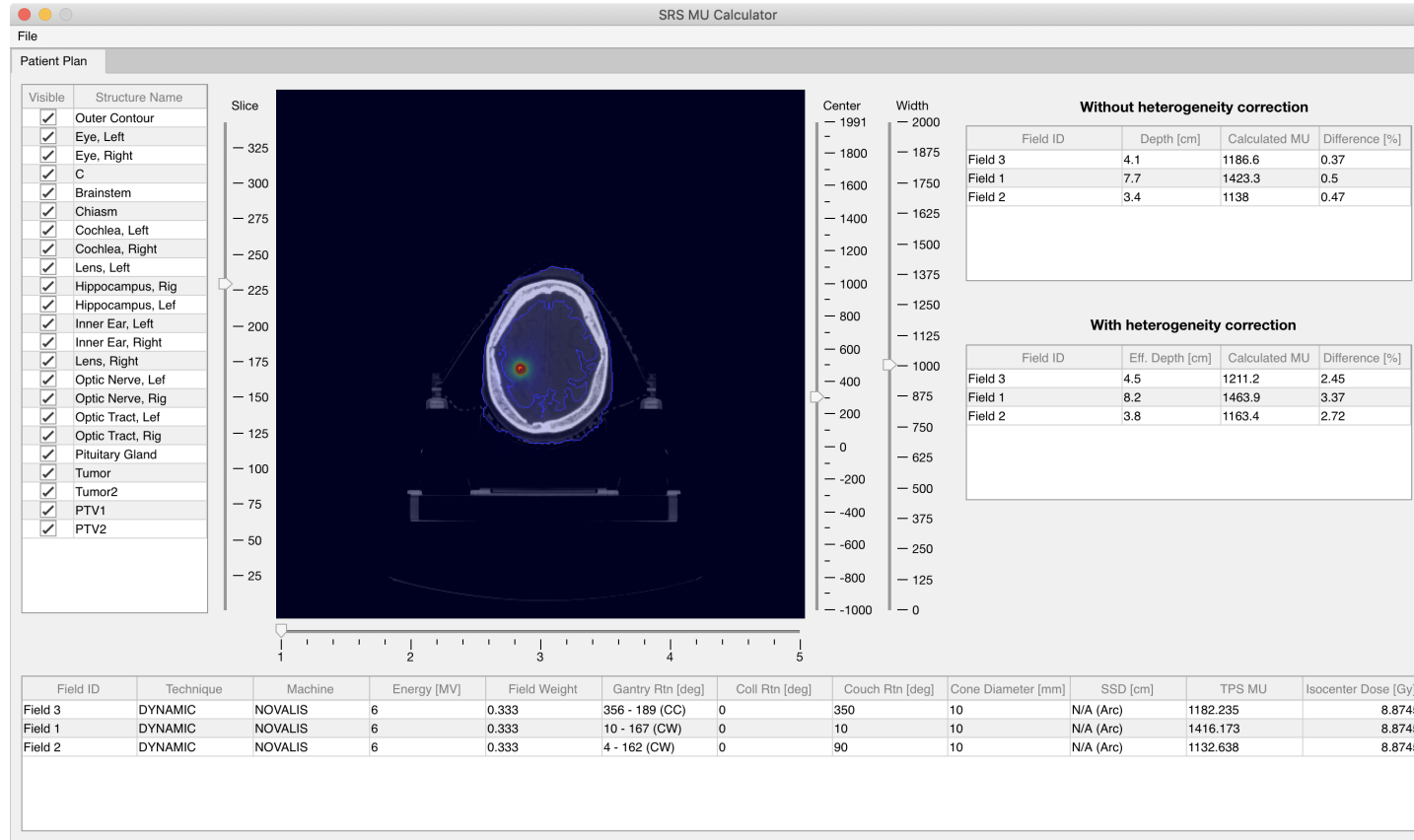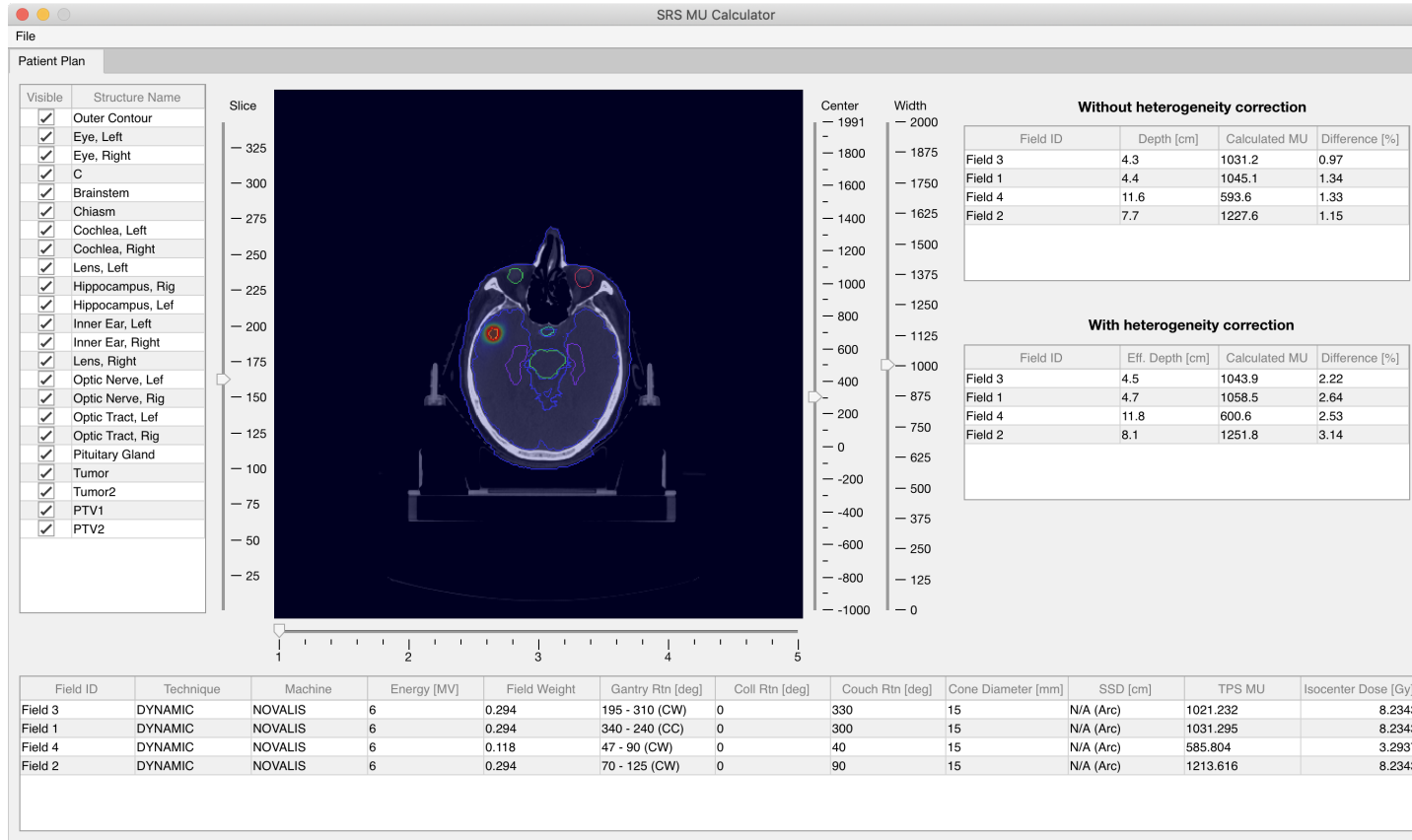
Figure 88: Patient ID 8.
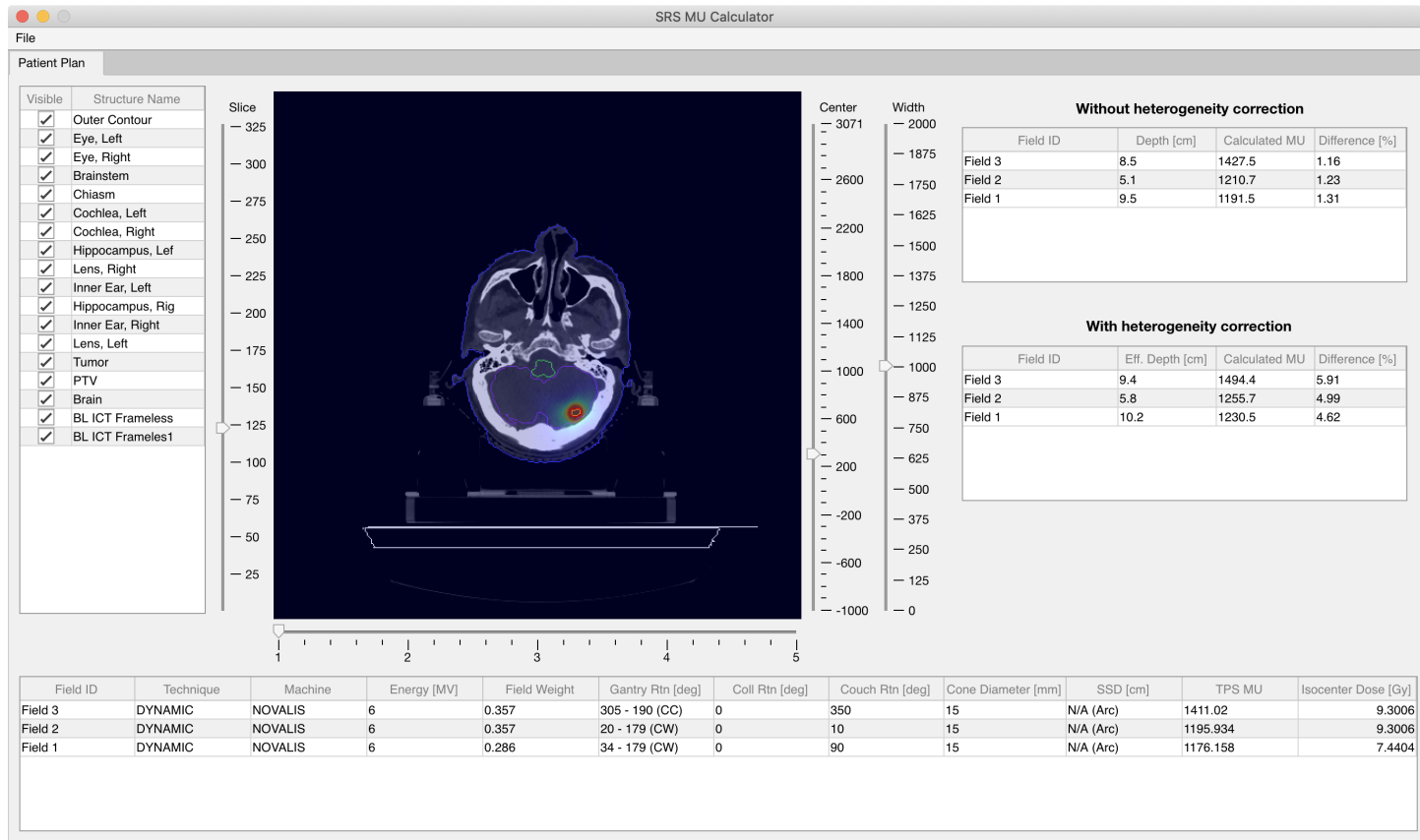
Figure 89: Patient ID 9.

Figure 90: Patient ID 10.

Figure 91: Patient ID 11.

Figure 92: Patient ID 12.